NOVA SCHOOL OF SCIENCE & TECHNOLOGY

DEPARTMENT OF PHYSICS

LUIS DUARTE RODRIGUES SUSTELO

Bachelor in Physics Engineering Sciences

ROLE OF POLARIZATION IN LASER SPECTROSCOPY OF HYPERFINE GROUND STATE IN MUONIC HYDROGEN AND HELIUM-3

MASTER IN PHYSICS ENGINEERING

NOVA University Lisbon
February, 2022

NOVA SCHOOL OF SCIENCE & TECHNOLOGY

DEPARTMENT OF PHYSICS

ROLE OF POLARIZATION IN LASER SPECTROSCOPY OF HYPERFINE GROUND STATE IN MUONIC HYDROGEN AND HELIUM-3

LUIS DUARTE RODRIGUES SUSTELO

Bachelor in Physics Engineering Sciences

Supervisor: Pedro Manuel Duarte Gonçalves Amaro
Assistant Professor, NOVA University Lisbon

Co-supervisor: Aldo Antognini
Paul Scherrer Institut

Examination Committee:

Chair: André João Maurício Leitão do Valle Wemans
Assistant Professor, NOVA University Lisbon

Rapporteur: Jorge Miguel Sampaio
Assistant Professor, Universidade de Lisboa

Adviser: Pedro Manuel Duarte Gonçalves Amaro
Assistant Professor, NOVA University Lisbon

MASTER IN PHYSICS ENGINEERING

NOVA University Lisbon
February, 2022

Role of Polarization in Laser Spectroscopy of Hyperfine Ground State in Muonic Hydrogen and Helium-3

To my grandparents and Kiara.

Acknowledgements

I would like to express my most sincere thank you to my adviser professor Dr. Pedro Amaro, for all the guidance, for all the knowledge he shared and the support we gave me always making sure that I was happy with my work. I would also like to thank my co-adviser Dr. Aldo Antognini, who despite being at distance gave me some crucial comments in the writing of the thesis, and professor Dr. José Santos, who checked on my work and gave me constructive advises. I would also like to thank my colleague Miguel Ferro, whose thesis is also in the context of the CREMA's HyperMu experiment, and with whom I ended up discussing results several times, which not only gave me extra motivation, but allowed me to write a better thesis.

I would like to thank FaCiT, and everyone involved in it, especially professor Dr. Teresa Calvão, who helped me in my time of need during my 2nd and 3rd year.

I would also like to thank professor Dr. Isabel Catarino, who in more than one occasion guided me out trouble, not only making the connection with FaCiT, as well as giving me some serenity during the harsh 4th year.

I must thank my long time friends, the ones who put up with me for a way before college: Luis Gonçalves, Patricia Cruz, Pedro Reis and Leonardo Faria. These are without a doubt, the ones who supported me most through everything, not only college.

Then there are the people I met at college. These are dozen of people, the ones that received me when I first came to college, the ones who I was lucky to be in the same class, and the ones I received when they first came to college. It is almost unfair not to put all of their names in here, as the stories we all had are endless. Despite this, I must at least write the names of the closest friends, Nuno Gomes, Pedro Pimentel, Guilherme Frizado, Tiago Moura, Carolina Adame, João Fernandes, Marcelo Morais, Duarte Carreira, Gonçalo Leónidas and Ricardo Castelhano. This oversimplified list represents the people I carry close to my heart, and were responsible for making these the best years so far. Indeed the most Special years.

To my brothers, my mother, my father and Qilby, you were never easy to deal with, but all of you have always supported and believed in me, and made what you could to gave me the best education. I dedicate this thesis to Kiara and my grandparents, even

tho they would not be able to understand anything of this work, it is the best I can do to thank them.

Finnaly, to the most important person, my partner Audrey Inácio, thank you so much for these four and half years. I couldn't have made it through them without you. Thank you.

Abstract

Laser spectroscopy have made possible the study of nuclear properties with highly accurate frequency-measurements of atomic transitions. When applied to muonic atoms, this capacity to resolve nuclear structure is further enhanced, and allows the measurement of the proton and α-particle with unprecedented accuracy. Furthermore, by measuring the transition frequency of the Hyperfine Splitting (HFS) of the ground state of muonic hydrogen, it is even possible to probe subtle details of the nucleus, such as Zemach radius and nucleus polarizability.

The Charge Radius Experiments with Muonic Atoms (CREMA)'s HyperMu experiment, was devised with the goal of measuring the HFS of the ground state of Muonic Hydrogen (μH) by observing the fast laser-excited atoms. Additionally, another experiment with the goal of measuring the HFS of the ground state of Muonic Helium-3 (μ^3He^+) is also being planned by the CREMA collaboration which detects electron decay-asymmetries from laser-excited atoms.

With the goal of optimizing the number of events detected in these experiments, all aspects must be optimized, including the polarization of the laser, i.e. if linear, circular or elliptical polarization produces a better expected value for the number of events detected.

In this thesis, a theoretical framework was developed based on the optical Bloch equations, adding phenomenological populations for the detected events, as well as the Doppler effect.

For the HyperMu experiment it was found no dependency on the polarization, while for the experiments based on electron-decay asymmetries it was confirmed that circular polarization produces the highest number of detected events. Moreover, it was found that even though the results are best for circular polarizations, the laser can have a reduced degree of circular polarization of up to 30% (mixture polarization of 70% circular and 30% linear), with the number of detected events only being compromised by 6%.

Keywords: Laser Spectroscopy, Hyperfine Structure, Bloch Equations, Laser Polarization, Muonic Hydrogen, Muonic Helium-3

Resumo

Espectroscopia de laser tornou possível o estudo de propriedades nucleares através de medições altamente precisas da frequência de transições atómicas. Quando aplicada a átomos muónicos, esta capacidade de resolver a estrutura nuclear é reforçada, e permite a medição do protão e partícula α com precisão sem precedentes. Além disso, medindo a frequência da transição da HFS do estado fundamental de hidrogénio muónico, é até possível sondar detalhes subtis do núcleo, como o raio de Zemach e a polarizabilidade do núcleo.

A experiência HyperMu da colaboração CREMA, foi planeada com o objectivo de medir a HFS do estado fundamental do μH por medição dos átomos rápidos excitados pelo laser. Adicionalmente, uma outra experiência com o objectivo de medir a HFS do estado fundamental do μ^3He^+ está a ser desenvolvida pela colaboração CREMA, que detecta a assimetria no decaimento de electrões vindos de átomos excitados pelo laser.

Com o objectivo de optimizar a o número de detecções nestas experiências, todos os aspectos devem ser optimizados, inclusive a polarização do laser, i.e. se polarização linear, circular ou elíptica produz um melhor valor esperado para o número de eventos detectados.

Nesta tese, o formalismo teórico foi desenvolvido com base nas equações ópticas de Bloch, adicionando populações fenomenológicas para os eventos detectados, assim como o efeito de Doppler.

Para a experiência de HyperMu não foi encontrada qualquer dependência da polarização, enquanto que para as experiências baseadas no decaimento assimétrico de electrões foi confirmado que polarização circular produz o maior número de eventos detectados. Além disso, foi encontrado que apesar dos resultados serem melhores para polarização circular, o laser pode ter um grau de polarização circular reduzido até 30% (mistura de polarizações, 70% circular e 30% linear), com o número de eventos detectados a ser comprometido em apenas 6%.

Palavras-chave: Espectroscopia de Laser, Estrutura Hiperfina, Equações de Bloch, Polarização do Laser, Hidrogénio Muónico, Hélio-3 Muónico

Contents

List of Figures

List of Tables

Abbreviations

μ**H**	Muonic Hydrogen
μ^3**He**$^+$	Muonic Helium-3
ChPT	Chiral Perturbation Theory
CODATA	Committee on Data for Science and Technology
CREMA	Charge Radius Experiments with Muonic Atoms
E1	Electric Dipole
E2	Electric Quadrupole
FWHM	Full Width Half Maximum
HFS	Hyperfine Splitting
LMS	Least Minimun Squares
M1	Magnetic Dipole
PSI	Paul Scherrer Institut
QED	Quantum Electrodynamics

Symbols

$\mathcal{A}$	Asymmetry Measure
a_k	Coefficients of the Non-Perturbed Wave-Function
c_i	Annihilation Operator
$\mathcal{A}^{\mathbf{Peak}}$	Asymmetry Measure at Resonance
$\vec{\mathbf{A}}$	Vector Potential
$\vec{\mathbf{B}}$	Magnetic Field
c	Speed of Light
c.c.	Complex conjugate of the expression written before it
χ	Tilt Angle Between Electric Fields
$c_i^\dagger$	Creation Operator
$\Delta\mathcal{A}$	Loss in Asymmetry
Δ	Laser frequency Relative to Transition Frequency
$\Delta\eta$	Loss in Polarization
$\vec{\mathbf{E}}$	Electric Field
ε_0	Vacuum Permittivity
e	Electron Charge (Positive)
E	Energy
η	Polarization Degree
F	Atom Total Angular Momentum Quantum Number
$\mathcal{F}$	Laser Fluence
Q	Four-Momentum Transfer
$\vec{\mathbf{F}}$	Atom Total Angular Momentum
Γ_c	Decoherence Rate

Γ_D	Doppler Width
G_E	Electric Sachs Form Factor
$\Gamma_{\mathbf{el}}^{F=0}$	Elastic Decay Rate of the Singlet State
$\Gamma_{\mathbf{el}}^{F=1}$	Elastic Decay Rate of the Triplet State
g_F	F Gyroscopic Factor
Γ_{ij}	Decay Rate from State ψ_i to ψ_j
$\Gamma_{\mathbf{in}}$	Inelastic Decay Rate
g_J	J Gyroscopic Factor
Γ_l	Laser Bandwidth
g_L	Angular Gyroscopic Factor
G_M	Magnetic Sachs Form Factor
Γ_μ	Muon Decay Rate
g_N	Nuclear Gyroscopic Factor
g_S	Spin Gyroscopic Factor
Λ	Gauge Scalar Field
H	Hamiltonian
H_0	Non-Perturbative Hamiltonian
H_A	Atomic Hamiltonian
$\hbar$	Reduced Planck Constant
h_D	Dirac Hamiltonian
H_I	Interaction Hamiltonian
H_{M1}	M1 Interaction Hamiltonian
I	Nuclear Spin Angular Momentum Quantum Number
$\mathcal{I}$	Laser Intensity
$\vec{\mathbf{I}}$	Nuclear Spin Angular Momentum
J	Total Angular Momentum Quantum Number
$\vec{\mathbf{J}}_{EM}$	Current Density in Electromagnetic Field
$\vec{\mathbf{J}}$	Total Angular Momentum
$\vec{\mathbf{k}}$	Wave-Number
k_B	Boltzmann Constant
L	Orbital Angular Momentum Quantum Number
$\mathcal{L}$	Lagrangian
$\vec{\mathbf{L}}$	Orbital Angular Momentum
M	Mass of the Nucleus

m	Mass of Orbiting Particle
m_e	Mass of the Electron
$\vec{\mathcal{M}}^{\mathbf{E1}}_{k'k}$	Vector E1 Matrix Element
m_F	Atom Total Angular Momentum Magnetic Quantum Number
m_I	Nuclear Spin Angular Momentum Magnetic Quantum Number
m_J	Total Angular Momentum Magnetic Quantum Number
m_L	Orbital Angular Momentum Magnetic Quantum Number
$\vec{\mathcal{M}}^{\mathbf{M1}}_{k'k}$	Vector M1 Matrix Element
m_r	Reduced Mass of the Atom
m_S	Spin Angular Momentum Magnetic Quantum Number
m_μ	Mass of the Muon
μ_0	Vacuum Permeability
μ_B	Bohr's Magneton
μ_N	Nuclear Magneton
$\vec{\mu}$	Dipolar Magnetic Moment
$\mathcal{N}$	Photon Number Operator
$\Omega_{\kappa m_J}$	Spherical Spinor
P	Pressure
$\vec{\mathbf{p}}$	Linear Momentum
P_c	Degree of Circular Polarization
φ	Phase Between Electric Fields
φ_m	Initial Phase of State with $m_F = m$
$\varphi_{m'm}$	Initial Phase Difference Between States with $m_F = m'$ and $m_F = m$
ϕ_k	Large Component of ψ_k
ϕ	Scalar Potential
P_l	Degree of Linear Polarization
$P_{n\kappa}$	Wave-Function Large Component
$\hat{\varepsilon}$	Polarization vector
Ψ	Total Wave-Function
Ψ_0	Total Non-Pertubative Wave-Function
ψ_k	Non-Pertubative Wave-Function
q	Charge of particle
$Q_{n\kappa}$	Wave-Function Small Component
$\mathcal{V}^{m'_F m_F}_{F'F}$	Rabi Frequency Between States Fm_F and $F'm'_F$
$\mathcal{V}_{F'F}$	Rabi Frequency Between States F and F'

$\mathcal{V}_{ij}$	Rabi Frequency Between States i and j
$\hat{\mathcal{V}}$	Matrix of Rabi Frequencies
R_α	Charge Radius of the α particle
R_E	Charge Radius
$\rho_{F'F}^{m_F' m_F}$	Population Between States $F'm_F'$ and Fm_F
$\rho_{\mathbf{DS}}$	Population of the Dark State
ρ_E	Charge Density
ρ_e^{BG}	Total Population of Electrons
ρ_{EM}	Charge Density in Electromagnetic Field
ρ_e^m	Population of Electrons Resulting from Muon with $m_F = m$
$\rho_{F'F}$	Population Between States F and F'
ρ_{ii}	Population of State ψ_i
ρ_{ij}	Entry ij of Population of Matrix
ρ_M	Current Density
$\hat{\rho}$	Matrix of Populations
R_p	Charge Radius of the proton
R_∞	Rydberg Constant
R_Z	Zemach Radius
S	Spin Angular Momentum Quantum Number
$\vec{\sigma}$	Pauli Vector
$M_{k'k}^{\mathbf{M1}}$	Scalar M1 Matrix Element
Q_S	Q Stoke Parameter
V_S	V Stoke Parameter
$\vec{\mathbf{S}}$	Spin Angular Momentum
T	Temperature
$T_{k'k}^{\mathbf{abs}}$	Absorption Transition Matrix Element
τ	Laser Time
τ_μ	Muon Lifetime
T_e	Classic Kinetic Energy
$T_{k'k}^{\mathbf{ems}}$	Absorption Transition Matrix Element
U_e	Potential Energy in Electromagnetic Field
ω	Angular Frequency
$W_{mm'}$	Statistical Weight
$\omega_{kk'}$	Relative Angular Frequency

1

Introduction

1.1 Context

Since its discovery by Theodore Maiman in the sixties [1], lasers have revolutionize modern society. Its applications are wide and in a multitude of fields of knowledge and applications, from basic fundamental sciences to metallurgy and engineering. With respect to basic science, and in particularly to high-accuracy measurements, the scientific harvest made by laser spectroscopy was critical to the development of many fields, such as chemistry, atomic physics, and even biology and medicine [2]. Progresses in laser spectroscopy in terms of increasing accuracy and delivered power, allowed even studies in nuclear physics by probing the atomic structure with high accuracy. Nuclear properties such as its masses, radii and nuclear moments can be extracted from highly accurate frequency measurements [3]. It can be used for the determination of fundamental constants such as the Rydberg constant, R_∞, the electron to proton mass ratio and proton to deuteron mass ratio [3–7], as well as to test Quantum Electrodynamics (QED) effects [4, 8], in context of atomic physics.

With this powerful tool that is laser spectroscopy, the proton radius can be measured with higher precision than with previous electron-proton scattering methods. Furthermore, by using muonic hydrogen, μH, instead of conventional hydrogen, the accuracy and precision of the measure increases by an order of magnitude (see section 1.3) [9]. This reasoning works equally for the measure of the μ^3He^+ radius [10].

The CREMA collaboration measured the charge radius, R_p (see section 1.5), of the proton ($R_p{}^{\text{CREMA}} = 0.84087(39)$ fm [11–13]) and of the alpha particle ($R_\alpha = 1.67824(83)$ fm [14]) with an unprecedented accuracy. Their results gave origin to the proton radius puzzle: the CREMA's measure is an order of magnitude more precise but it was off by 7 variances of the accepted value (at the time, the Committee on Data for Science and Technology (CODATA) value, $R_p{}^{\text{CODATA}} = 0.8775(51)$ fm), which was obtained with electron-proton scattering experiments and hydrogen spectroscopy [15, 16]. This discrepancy arose some controversy within the scientific community, and a lot of effort was made from a theoretical point of view to check all the contributions for both the μH and

conventional H spectroscopy, as well as in new scattering experiments. Although some refinement occurred, they were not able to completely explain the discrepancy and solve the puzzle, meaning that either the fault was in the experiments, or some new physics is coming into play.

From an experimental point of view, there was a great discussion regarding the form factors (see section 1.5) measured in e-p scattering. Since experimentally, they can not be measured at $Q^2 = 0$ (Q is the four-momentum transfer), the proton radius which is the slope of the form factor can only be obtained by extrapolation to $Q^2 = 0$. This extrapolation is highly dependent on the model used for charge distribution within the nucleus. Several of the extrapolation based on the physics model of the proton obtain results compatible with μH spectroscopy [17].

Eventually, the muon spectroscopy results became widespread accepted in the community (and now appear in the CODATA-2018 database of fundamental constants [18, 19]), after a new e-p scattering and several new hydrogen spectroscopy experiments provided results consistent with CREMA's result.

CREMA's results also included a value of R_Z= 1.082(37)fm for the Zemach radius (see section 1.5) of H. This has a relative accuracy of 3.4% [12], which is comparable to results from electron spectroscopy [20, 21] and e-p scattering [22, 23]. The Zemach radius is directly connected to the HFS (see section 2.7), and thus this result was an initial motivation to perform measurements of the ground state HFS of muonic hydrogen, and similarly to the HFS muonic helium. Some motivations for measuring the Zemach radius are the impact on three aspects of fundamental physics: bound-state QED in H-like systems, the understanding of the internal structure of H and He, more specifically, the magnetic distribution and the low-energy spin distribution [10]. Understanding these phenomena will also help shedding light on the muon magnetic anomaly discrepancy (Muon g-2 experiment at FermiLab) [24], since both this experiment and the experiments with muonic atoms are testing the standard model by questioning the possibility of the muons not interacting with other particle in the exact the same way as electrons.

While previous experiments of the CREMA collaboration were based on the measurement of the Lamb-shift ($2S_{\frac{1}{2}} - 2P_{\frac{1}{2}}$) [11–13], new measurements are planned for the measurement of the HFS of the ground state of μH and $\mu^3\mathrm{He}^+$. This improvement can test for QED two-photon exchange contributions, expose possible lepton flavor violations and will establish benchmarks to modelling the proton and ^{3}He internal structure [10, 25].

1.2 Motivation and Organization of Thesis

Two different types of experiments where devised to measure the Zemach radius (see section 1.5) of the H (using μH), diffusion experiments (see section 1.6), such as the CREMA-HyperMu [10] and the FAMU [26] experiments, and an asymmetry experiment (see section 1.7) from the RIKEN center [27, 28]. To measure the Zemach radius of the

He (using μ^3He^+), there is only a proposal from the CREMA collaboration (section 1.8) using an asymmetry method [10].

Table 1.1: Proposed experiments for measuring the HFS of each atomic system.

	μH	μ^3He^+
Diffusion	CREMA-HyperMu FAMU	—
Asymmetry	RIKEN	CREMA

All these experiments in table 1.1 aim to measure the HFS with laser spectroscopy. The role of the polarization in each in these experiments is tightly connected to the atomic structure of the atom and how different polarizations of the incident laser induce transitions to different sub-levels (see section 1.4). The purpose of this thesis is to investigate the role of the polarization of the laser field in the planned experiments, i.e., if linear or circular (or anything in between) polarized light can have an impact in the optimization of CREMA's experiments (both μH and μ^3He^+) [29] as well as for similar ones like the RIKEN-RAL experiment [26–28].

In this thesis, the theoretical model to explain the time evolution of the population of each state for a general polarization is deduced along three chapters: In Chapter 2, the interaction of the laser with the atoms is described; In Chapter 3 the equations developed in Chapter 2 are applied to the particular atomic systems relevant for the experiments, and the various decay sources are included *a posteriori*; In Chapter 4, where some specificities of the experimental setup are included, such as muon decay, method of detection of events and the Doppler effect.

1.3 Why Mounic Atoms?

In muonic atoms, the electrons are replaced by muons, which have similar properties to the electron, except its mass that is much heavier: $m_\mu \approx 207 m_e$. For μH, the reduced mass of this system is $m_r \approx 186 m_e$, and thus, the Bohr's radius of the muon about 186 times closer to the nucleus, and the binding energy (in the Bohr's model) 186 times larger. Taking into account that the nucleus is not point-like, there is a greater overlap between the muon orbitals and the nucleus wave-function, relative to the electron orbitals. This is pictorially shown in figure 1.1. From the Bohr model, an estimate of the probability of being inside the nucleus is 6.5 million times more likely for muons than for electrons [12, 30, 31].

Due to this superposition, the nuclear effects in the atomic structure are enhanced in muonic atoms, and thus laser spectroscopy of muonic atoms has long been a goal since the 90's [31].

In muon experiments, the muon production, deceleration, formation of muonic atoms, and measurements must all be executed within the τ_μ= 2.2 μs lifetime of the muon [9, 11, 12, 28, 31, 32].

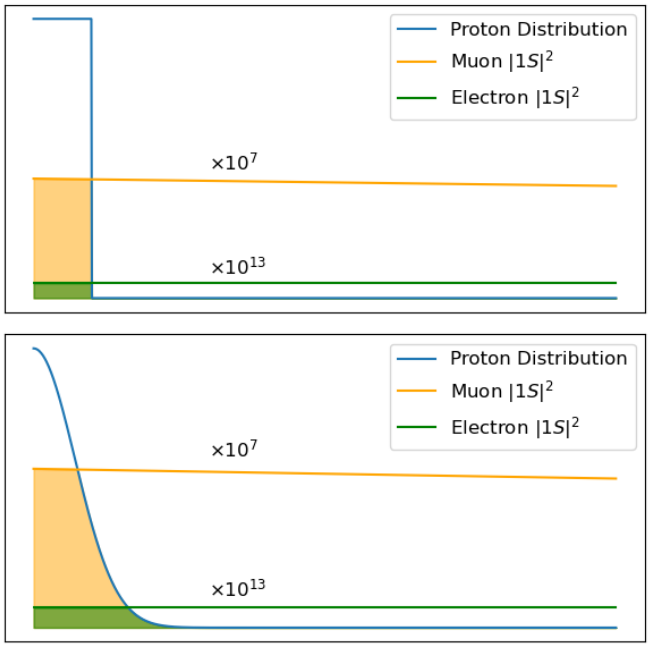

Figure 1.1: Probability of finding a $1S$ muon (yellow, line amplified by 10^7) or a $1S$ electron (green, line amplified by 10^{13}) inside the nucleus (blue). Two different types nucleus distributions are assumed, rectangular (top), gaussian (bottom).

The muon production method and the formation of muonic atoms is the same for all types of experiments [27, 29]. The muons are created by colliding protons from an accelerating ring to a target foil optimized for pion production, which decay into muons. The muons are then slowed down in gas target of H_2 (for μH experiments) or ^{3}He (for the μ^3He^+ experiment), forming highly excited muonic atoms. These decay in a cascade to the $1S_{\frac{1}{2}}$ ground state (99% of them), emitting x-rays, except for some that would decay to the long lived $2S$ level (1%). For μH, this process is represented in figure 1.2. For μ^3He^+ the process is similar just with different numerical values for the emitted x-rays and for the percentage of atoms reaching the $2S$-state.

In the CREMA Lamb-shift experiment [9, 11, 12, 33] were the charge radius was measured, the $2S$ atoms would be laser-excited to the $2P$ state, which promptly decays to the ground state ($2P$ has a lifetime of 8.5 ps [12]), emitting characteristic 1.9 keV x-rays, that could be detected, to expose a successful laser transition, allowing to identify the Lamb-shift transition energy [11, 12, 33].

1.4 Accurate Atomic Structure of H-Like Atoms

The atomic structure is the set of energy levels of the atom. In order to reach the level of nuclear finite-size effects, an accurate theory of the atomic structure must include the following effects:

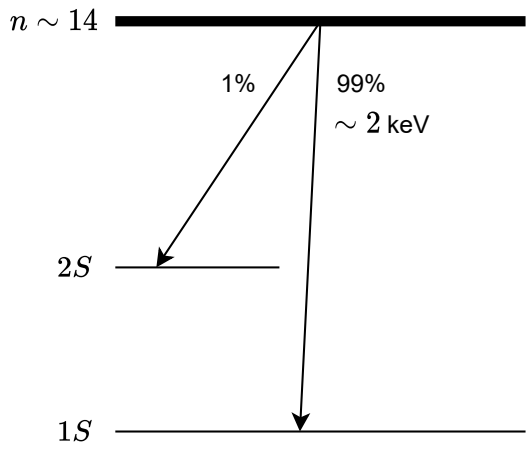

Figure 1.2: Process formation of muonic hydrogen. 99% will decay promptly to the ground state and 1% to the long lived $2S$ state.

1. Coulomb interaction: Starting point is to include the Coulomb potential into the Schrödinger equation to obtain the Bohr's energy levels.

2. Relativistic effects: Obtained by the Dirac equation (or Breit-Hamiltonian) and responsible for the fine structure (states with different total angular momentum $\vec{\mathbf{J}}$ have different energies. See section 2.3 for more details).

3. QED effects: Mainly the vacuum polarization (the background electromagnetic field produces a virtual particle pair that interacts with the atom, changing the energy of its states) and the self-energy (results of the interaction of the particles with the field that themselves create). Responsible for the Lamb-shift.

4. Nuclear Spin effects: Similarly to the fine structure, these affects result from the coupling of two angular momenta, the spin of the nucleus $\vec{\mathbf{I}}$ and the total angular momentum of the orbiting particle $\vec{\mathbf{J}}$. Responsible for the hyperfine structure (section 2.7).

5. Nuclear size effects: Result from not considering the nucleus as a point but as a distribution in space. Induce subtle effects called the two-photon-exchange, related to the polarization of the nucleus. Laser spectroscopy reaches this precision to sense even these tiny nuclear effects.

other effects must be also considered such as recoil corrections and weak interactions [10]. A representation of these effects is shown in the figure 1.3, there it can be seen that the nuclear size effects shift in conventional hydrogen 1.3(a) is six orders of magnitude lower than in muonic hydrogen 1.3(b), because of the large overlap between the atomic and nuclear wave-functions as shown in section 1.3.

In figure 1.3 the degeneracy of the magnetic sub-levels for different projections of angular momentum into z-axis is not visible, since by definition, degenerate levels have

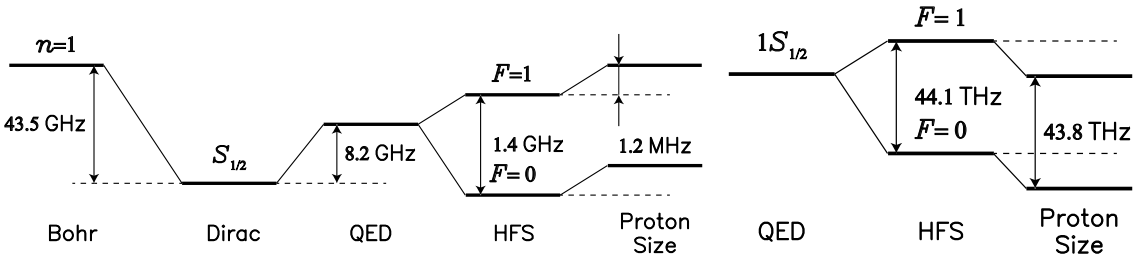

(a) Ground state of hydrogen.

(b) Ground state of muonic hydrogen.

Figure 1.3: Energy shifts in the ground state of H and μH. From left to right, the energy shifts decrease. In figure 1.3(b), only the effects after QED are represented. Energy shifts are not to scale.

the same energy. To consider these magnetic sub-levels we have to introduce the total angular momentum F. For each possible value of F, there is a possible energy level, with a degeneracy of $2F+1$, each sub-state is associated with a magnetic sub-level, m_F, which assumes every value between -F and F. For the $1S$-HFS of μH the ground state will be the singlet state $F=0$, while the excited state is a triplet state with $F=1$, figure 1.4(a). For the μ^3He^+ it is the other way around, the ground state is a triplet state, and the excited state is a singlet state, figure 1.4(b). The angular wave-functions for the $F=1$ states are symmetric, while the $F=0$ is antisymmetric, and they result from linear combinations of the four possibilities for the coupling of the muon spin with the nuclear spin. These four combinations are $\uparrow\uparrow$ (1/2,1/2), $\uparrow\downarrow$ (1/2,$-$1/2), $\downarrow\uparrow$ ($-$1/2,1/2) and $\downarrow\downarrow$ ($-$1/2,$-$1/2), and their linear combination to form the m_F sub-states is represented with the arrows in figure 1.4

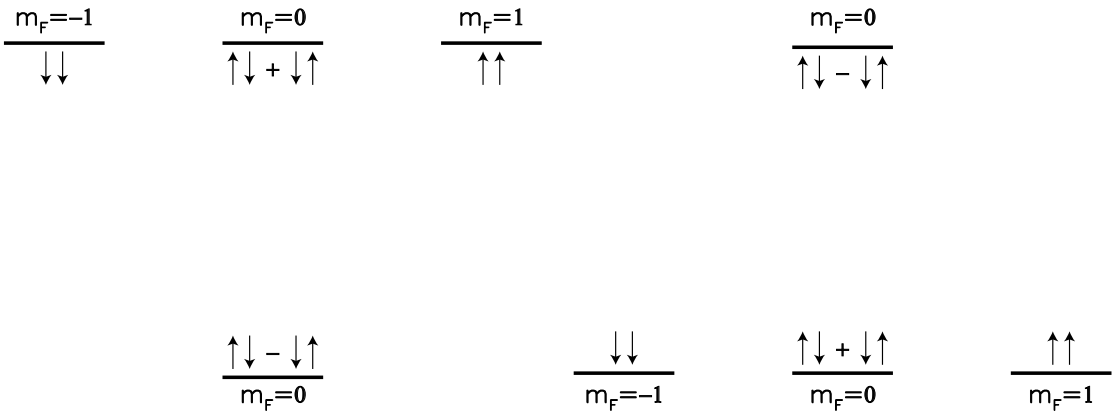

(a) Energy diagram of μH.

(b) Energy diagram of μ^3He^+.

Figure 1.4: Energy diagrams of μH and μ^3He^+. For μH the triplet state is the excited state, while for μ^3He^+ it is the ground state. The arrows represent the muon and the nuclear spin, respectively. Both these spins can assume two possible values 1/2 and $-$1/2.

1.5 Charge and Zemach Radii

When discussing the proton (H) or ^{3}He radius, it is necessary to first define what exactly is the radius of these particles. The particles are not solid spheres that have a concrete radius, but rather quantum objects and follow a distribution of where they are most likely to be. On the other hand, these are charged particles, there is distribution of charge in space due to them. As such, a charge radius can be approximated (non-relativistically) to be:

$$R_E^2 = -\frac{6\hbar^2}{G_E(0)}\frac{\mathrm{d}G_E(Q^2)}{\mathrm{d}Q^2}\bigg|_{Q^2=0} \approx \int \mathrm{d}\vec{\mathbf{r}}\rho_E(\vec{\mathbf{r}})r^2\,, \tag{1.1}$$

where $\rho_E(\vec{\mathbf{r}})$ is the charge density due to the nucleus in question (H or ^{3}He) [9, 34]. The charge radius is formally given as the derivative at $Q^2 = 0$ of the electric Sachs form factor, $G_E(Q^2)$, [35] (which is necessary to describe scattering processes between particles with internal structure, like protons and neutrons [10]), but can be approximated to the 2^{nd}-moment of the charge distribution given by the integral in equation (1.1).

The Zemach radius, that play a role in the HFS, can also be defined in terms of the electric and magnetic form factors, but it can be approximated (non-relativistically) to the 1^{st}-moment of the convolution of the electric and charge densities (double integral in equation (1.2)) [10, 12, 13, 29].

$$R_Z = -\frac{4}{\pi}\int_0^\infty \frac{\mathrm{d}Q}{Q^2}\left(\frac{\mu_N}{\mu_x}G_E(Q^2)G_M(Q^2) - 1\right) \approx \int \mathrm{d}\vec{\mathbf{r}}r \int \mathrm{d}\vec{\mathbf{r}}'\rho_E(\vec{\mathbf{r}}-\vec{\mathbf{r}}')\rho_M(\vec{\mathbf{r}}')\,, \tag{1.2}$$

where, μ_N is the nuclear magneton, and μ_x the magnetic dipole moment of the nucleus in investigation. On the other hand, the HFS energy of the ground state of μH can be deduced to be

$$\Delta E^{\text{HFS}} = 182.819(1) - 1.301R_Z + 0.064(21)(\text{meV})\,, \tag{1.3}$$

with the Zemach radius R_Z in femtometers [10, 20, 21]. The first term correspond to the cumulative of all the Dirac, QED and corrective effects that do not depend on R_Z. The second term corresponds to the contribution due to the finite size of the nucleus. The third term is due to the proton polarizability, and it is the least known contribution. Complementing μH measures with scattering measurements via a dispersive approach, provides an alternative route to compute this complex term, which can only be calculated theoretically *ab initio* via Chiral Perturbation Theory (ChPT) [36]. The wavelength of the $1S$-HFS transition of μH is 6.8 μm.

From a direct analysis of equation (1.3), it is obvious that measuring the HFS of the ground state of μH allows to calculate the Zemach radius of the proton, and if the Zemach radius of the proton is known, it allows to calculate the polarization contribution.

For $\mu^3\text{He}^+$, the situation is identical and the Zemach radius of ^{3}He is given by an equation of the same form as (1.3), but with different values for each contribution. There are no theoretical predictions for the polarizability term of $\mu^3\text{He}^+$. A rough approximation of the $1S$-HFS transition wavelength of $\mu^3\text{He}^+$ is 930nm.

The CREMA's measurements of the various $2S-2P$ transitions in μH where combined to obtain the Lamb Shift ($2S_{\frac{1}{2}} - 2P_{\frac{1}{2}}$) and the $2S$-HFS from which the charge and Zemach radius were extracted after comparing to their respective theoretical prediction [12].

1.6 CREMA-HyperMu Experiment

The HyperMu experiment was proposed with the goal of measuring the $1S$-HFS energy of μH at the ppm level, and with that, determine the two photon exchage contribution to a relative precision of 10^{-4} [25, 29, 34].

The CREMA-HyperMu is a diffusion type experiment similar to the FAMU experiment. In diffusion type experiments, the μH atoms are de-excited to the ground state ($F=0$) and thermalized to the gas temperature, and excited by a laser pulse to the upper state of the hyperfine structure ($F=1$), and these are de-excited back to the ground state, carrying some extra kinetic energy that allows them to reach the target walls where they are detected.

The process can thus be split into 3 steps, which are represented in the sketch of figure 1.5 (extracted from [29]). Step i) is the formation of μH as described in section 1.3, where 10 to 12 MeV/c muons delivered by the high intensity proton accelerator at Paul Scherrer Institut (PSI) pass an entrance detector. About 10% of them are stopped in the H_2 gas at 22 K and 0.5 bar, forming μH. In step ii) a high intensity laser excites the atoms from $F=0$ to the $F=1$ state. These decay back to the ground state via inelastic collisions with the surrounding H_2 gas, so that the HFS energy is converted to kinetic energy, where the μH acquires about 0.1 eV [37]. In step iii) the μH atoms with 0.1 eV diffuse in H_2 gas and reach the walls of the chamber [38] which are coated with gold. This material captures the muon in an excited state forming μAu^*. The muon cascades down emitting x-rays, which are detected by scintillators. When the laser frequency is at resonance with the $1S$-HFS transition, there will an increase detected x-rays after laser excitation.

The $F=0$ to $F=1$ transition is forbidden by the E1 selection rules, but it is allowed for M1 type. The M1 transitions have a probability of occurrence much lower than the E1, making the HyperMu experiment particularly challenging.

This experiment cannot resolve the magnetic sub-level structure of the $F=1$ state. Although the atom can be excited to any of the three sub-levels, $m_F=-1,0,1$, after it decay back to the ground state, it will be a fast atom that will be detected in the same way regardless of its previous m_F. As such considering a 2-level structure (one ground state, $F=0$, and one excited state, $F=1$) should be enough to describe the system. However it must be proven that the 4-levels structure (one ground state, $F=0$ with $m_F=0$, and three excited states, $F=1$ with $m_F=-1,0,1$) produces the same results as the 2-levels description. Here is where the polarization of the laser may play a role.

Depending on the polarization there might be a different transition probability to one sub-level comparing to the others. The goal of this thesis, among other, is to find out whether the polarization plays a role in the HyperMu experiment.

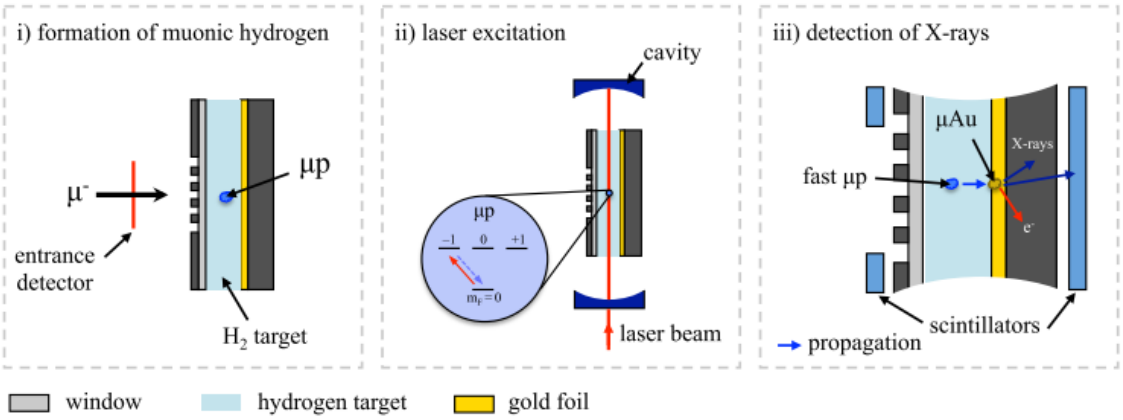

Figure 1.5: Sketch of the experimental setup of the HyperMu experiment. Step i) formation, de-excitaiton and thermalization of μH. Step ii) Laser excitation to the $F=1$ followed by collisions with the surrounding H_2 gas molecules which de-excites the atoms back to the ground state $F=0$. Step iii) The de-excited μH atoms have acquired 0.1 eV kinetic energy and reach the walls of the target where they are detected. Figure reproduced from [29].

1.7 RIKEN Experiment

The RIKEN experiment has the same goal as the HyperMu and FAMU experiments: measure the $1S$-HFS in μH. The difference is that this is an asymmetry type experiment.

In this asymmetry experiments, after the muonic atoms are formed and de-excited to the ground state ($F=0$), a circularly polarized laser excites the μH atoms to one specific sub-level (to the $m_F=\pm1$ depending whether the laser is left or right circularly polarized, see section 2.2, for more detail of the laser polarization and section 3.2.3 for more details on the respective possible transitions). Since only one of the sub-levels of the excited state is being populated, an asymmetry in the populations of the sub-levels $m_F=1$ and $m_F=-1$ will be created.

Because the muons decay to electrons and neutrinos occurs the parity violation via weak interaction,

$$\mu \rightarrow \nu_\mu + e^- + \overline{\nu}_e \,. \tag{1.4}$$

The electrons are emitted preferentially in the opposite direction of the z component of the muon spin (m_S) [28]. Hence the electrons can be detected in opposite sides of the target, relative to the muon spin. By applying a magnetic field, the z direction will be well defined, and the electrons will be mostly emitted along this axis, so that detectors can be placed in the positive and negative direction of the magnetic field, the front and back detectors, respectively. The setup can be found in figure 1.6, where the magnetic field is applied in the transverse direction comparatively to the direction of entrance of the muons in the chamber.

The possible states of the hyperfine structure are, for $F=0$, $m_F=0$ and for $F=1$, $m_F=-1,0,1$, which are given in terms of linear combinations of the nuclear spin projection m_I,

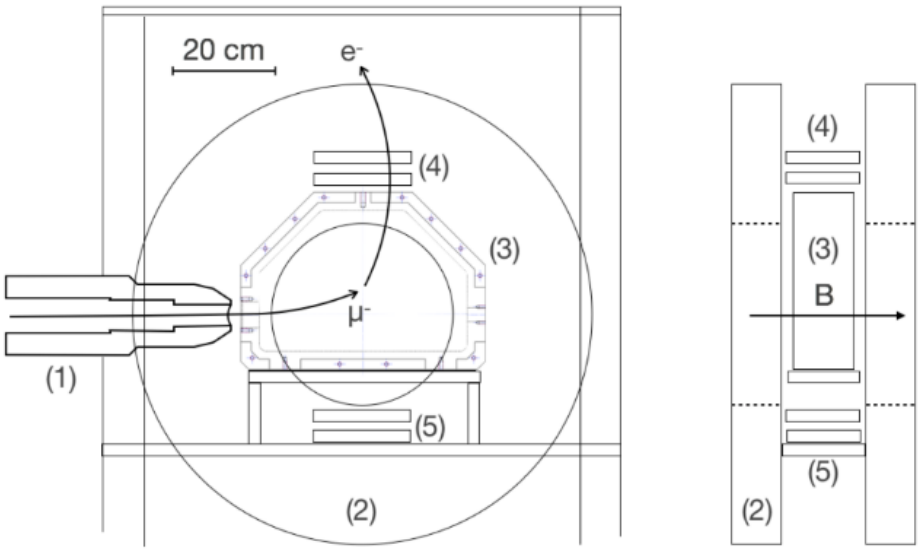

Figure 1.6: Sketch of the experimental setup of the RIKEN hyperfine splitting experiment. A muon beam enters in the chamber through (1), and its stopped in the H_2 gas target (3). The Helmholtz coils (2) create a magnetic field that orients the spin of the muons. The muons decay to electrons that are detected in the front and back detectors (not shown in figure). The upper detector (4), and lower detector (5) allow for a larger acceptance. Figure reproduced from [28].

and the muon spin m_S (considering that in the $1S$ orbital, the angular momentum $\vec{\mathbf{L}}$ is 0 as well as $m_L = 0$), that were represented in figure 1.4.

$$|F=0, m_F=0\rangle = \frac{1}{\sqrt{2}}\left|m_S=\frac{1}{2}, m_I=-\frac{1}{2}\right\rangle - \frac{1}{\sqrt{2}}\left|m_S=-\frac{1}{2}, m_I=\frac{1}{2}\right\rangle \tag{1.5a}$$

$$|F=1, m_F=-1\rangle = \left|m_S=-\frac{1}{2}, m_I=-\frac{1}{2}\right\rangle \tag{1.5b}$$

$$|F=1, m_F=0\rangle = \frac{1}{\sqrt{2}}\left|m_S=\frac{1}{2}, m_I=-\frac{1}{2}\right\rangle + \frac{1}{\sqrt{2}}\left|m_S=-\frac{1}{2}, m_I=\frac{1}{2}\right\rangle \tag{1.5c}$$

$$|F=1, m_F=1\rangle = \left|m_S=\frac{1}{2}, m_I=\frac{1}{2}\right\rangle \tag{1.5d}$$

Investigating these equations, we see that levels with $m_F = 0$ ((1.5a) and (1.5c)) have a fifty-fifty chance of having $m_S = \pm 1/2$, and thus a fifty-fifty change of the electron being emitted in either $\mp$z direction. The number of atoms detected in each detector due to these states with $m_F = 0$ is about the same so that they contribute only to a background of detections. The $m_F = -1$ state (1.5b) has the the muon spin pointing in the -z direction, and the electrons are emitted in the z direction. The $m_F = 1$ state has the muon spin pointing in the z direction and the electrons are thus emitted in the -z direction. In summary, the $m_F = -1$ muons (1.5d) will be detected preferentially in the front detector, the $m_F = 1$ in the back detector, and the $m_F = 0$ in both detectors with equal probability.

Overall, when the laser is at resonance with the transition, there will be maximal asymmetry in the populations of the $F=1$ sub-levels, and thus an asymmetry in the direction of the emitted electrons distributions. To quantify this asymmetry, the difference in detections between both detectors, normalized to the total detections (to account for the background) is computed [27]

$$\mathcal{A} = \frac{N_F - N_B}{N_F + N_B}\,, \tag{1.6}$$

where N_F is the number of detections in the front detector and N_B the number of the detections of the back detector.

The process of laser excitation and collisional quenching is the same as in HyperMu and FAMU experiments. In the diffusion experiments the collisional decays are beneficial since they create the fast μH atoms that can be detected, while in the asymmetry experiments, these collisional decays will return the atoms to the ground state undoing the asymmetry created by the laser. As such, in the asymmetry experiments, the pressure of the gas must be much lower than in diffusion experiments, to lower the rate of collisions between the μH($F=1$) atoms and the H_2 gas so that depolarization effects caused by inelastic collision quenching the μH atom to the $F=0$ state are minimized. On the other hand, if the pressure is too low, the number of μH formed is less, since the probability of the muons being stopped in the H_2 gas reduces, so that a trade-off preasure must be found [28].

The polarization needed in the asymmetry experiments is already well know, it must be such that all the excitations will be to one of the sub-levels, i.e. circular polarization. The focus of this thesis regarding this type of experiment is to explore how small deviations from circular polarization (i.e. elliptical polarization), affect the asymmetry of the $F=1$ sub-states, and moreover, the asymmetry of the electron distribution.

1.8 CREMA-μ^3He$^+$ Experiment

The CREMA-μ^3He$^+$ experiment [29] has the goal of measuring the Zemach radius of He, by measuring the $1S$-HFS of μ^3He$^+$ with the asymmetry method. In this experiment, ^{3}He is used instead of the more common ^{4}He, as ^{4}He nuclear spin is null, thus having no HFS.

The concept behind this method (experimental setup in figure 1.7) is the same as in the RIKEN experiment: The muons are stopped in a ^{3}He target, forming μ^3He$^+$ which quickly decay to the ground state (step i)). A circularly polarized laser excites the atom creating an asymmetry (step ii)). In step iii) the muon decays according to (1.4), emitting an electron in the opposite direction to the muon's z component of the spin (m_S). These electrons are then detected in opposite directions of the chamber (with the z direction being defined by an external magnetic field), allowing to detect the asymmetry in sub-levels (step iv)).

The process in which the asymmetry is created is a little bit different from the RIKEN experiment. Since in μ^3He$^+$ the $F=0$ state is the excited state and the $F=1$ the ground

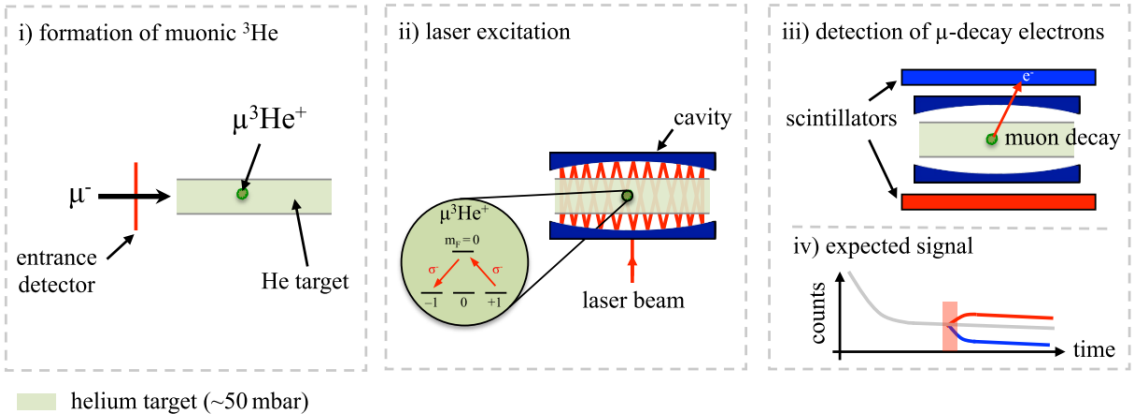

Figure 1.7: Sketch of the experimental setup of the CREMA-μ^3He$^+$ experiment. Step i) formation and de-excitation of μ^3He$^+$. Step ii) Laser excitation from the ground-state with $m_F = 1$ to the $F = 0$ state, followed by de-excitation to the $m_F = -1$ ground state due to stimulated emission, producing an asymmetry in the $m_F = \pm 1$ populations. Step iii) The symmetric population distribution in the magnetic sub-levels can be exposed by placing scintillators that detect the emitted electrons from μ-decay. Step iv) After the laser is turned on, an asymmetry in the counts of both detectors is created. Figure reproduced from [29].

state, the asymmetry must be created in the ground state. As such this asymmetry is created in a two-step process, first the ground state $m_F = \pm 1$ is excited to the $F = 0$ by applying a right or left circularly polarized laser, respectively. Then the atom decays to the $m_F = \mp 1$ state via stimulated emission due to the laser. In other words, transitions due to the laser reduces the m_F number by 1 for right polarization, or increases by 1 for left polarization, creating an asymmetry in the sub-level populations of the $F = 1$ state.

The levels can still be represented by equations (1.5), just with different meaning ($F = 0$ is the excited state, $F = 1$ is the triplet ground state), and thus the electrons are emitted in the same preferential way, in the z direction for $m_F = -1$, in the -z direction for $m_F = 1$ and with 50% change of either $\pm$z direction for $m_F = 0$, which creates a background in detections.

If the excited atoms decay due to collisions with the He gas, they have an equal chance of going to any of the sub-levels of the ground state (see appendix E.3), which still creates some asymmetry, instead of canceling the asymmetry like in the RIKEN case. As such, the problem with the pressure of the gas target does not exist in this experiment. Note that the collisional effect in the μ^3He$^+$ includes the formation of molecules, which is very different from the μH and cannot be treated in this study. As a simplification only interactions between the μ^3He$^+$ and the He that do not originate other species (like He_2 molecules) are considered.

As for the RIKEN experiment, we focus here only on the role of polarization in this experiment which will consist in analyzing how small deviations from circular polarization will affect the asymmetry measure.

2

Photon-Atom Interaction Theory

2.1 Electromagnetic Radiation: Classical Approach

To study the interaction of photons with an atom, or equivalently, radiation with matter, this radiation must be described precisely with the methods of quantum mechanics. Before delving into quantum theory, radiation can be classically described as an electromagnetic wave. This is accomplished with the classical electromagnetic Maxwell equations (S.I. Units):

$$\vec{\nabla}\cdot\vec{\mathbf{E}} = \frac{\rho_{EM}}{\varepsilon_0}\,, \tag{2.1}$$

$$\vec{\nabla}\cdot\vec{\mathbf{B}} = 0\,, \tag{2.2}$$

$$\vec{\nabla}\times\vec{\mathbf{E}} = -\frac{\partial\vec{\mathbf{B}}}{\partial t}\,, \tag{2.3}$$

$$\vec{\nabla}\times\vec{\mathbf{B}} = \mu_0\vec{\mathbf{J}}_{EM} + \mu_0\varepsilon_0\frac{\partial\vec{\mathbf{E}}}{\partial t}\,, \tag{2.4}$$

where $\vec{\mathbf{E}}$ and $\vec{\mathbf{B}}$ are the electric and magnetic fields, as well as ρ_{EM} and $\vec{\mathbf{J}}_{EM}$ being the charge and current densities. ε_0 and μ_0 are the vacuum's permittivity and permeability respectively. For simplicity it is often considered the description of the electromagnetic wave in vacuum, this is, in regions where there are no charges or currents, $\rho_{EM}=0$, $\vec{\mathbf{J}}_{EM}=0$. In this case, both the electric field and the magnetic field obey the wave equations (2.5) and (2.6) [39].

$$\nabla^2\vec{\mathbf{E}} - \frac{1}{c^2}\frac{\partial^2\vec{\mathbf{E}}}{\partial t^2} = 0 \tag{2.5}$$

$$\nabla^2\vec{\mathbf{B}} - \frac{1}{c^2}\frac{\partial^2\vec{\mathbf{B}}}{\partial t^2} = 0 \tag{2.6}$$

In these equations, $c = \frac{1}{\sqrt{\varepsilon_0 \mu_0}}$ is the light speed. These wave equations state that if there is an electromagnetic field in vacuum, it has to be a self-sustainable propagating (electromagnetic) wave traveling at light speed, which indicates that light itself is a electromagnetic propagating wave.

2.1.1 Electromagnetic Potentials

In order to obtain a quantum mechanical description of the electromagnetic field, it is practical to redefine the Maxwell equations in terms of electric potentials, because they allow for more compact equations. For this, the electric and magnetic field can be represented in terms of a vector potential $\vec{\mathbf{A}}$ and a scalar potential ϕ defined by the following equations:

$$\vec{\mathbf{E}} = -\vec{\nabla}\phi - \frac{\partial \vec{\mathbf{A}}}{\partial t} \tag{2.7}$$

$$\vec{\mathbf{B}} = \vec{\nabla} \times \vec{\mathbf{A}} \,. \tag{2.8}$$

Since the divergence of a curl is mathematically zero, and the divergence of $\vec{\mathbf{B}}$ is zero (presently no magnetic monopoles have been observed), then $\vec{\mathbf{B}}$ must be the curl of a vector potential, and thus the vector potential $\vec{\mathbf{A}}$ is identified as the Gauss' law for magnetism (2.2). Next, considering the Faraday's law (2.3) and combining it with (2.8), the quantity $\vec{\mathbf{E}} + \frac{\partial \vec{\mathbf{A}}}{\partial t}$ must be the gradient of a scalar potential, since the curl of a gradient is mathematically zero. The minus sign before the gradient in equation (2.7) allows to identify the electrostatic relation $\vec{\mathbf{E}} = -\vec{\nabla}\phi$.

With equations (2.7) and (2.8), the Maxwell equations can be reduced to equations

$$\nabla^2 \phi + \frac{\partial}{\partial t} \vec{\nabla} \cdot \vec{\mathbf{A}} = -\frac{\rho}{\varepsilon_0} \tag{2.9}$$

and

$$\nabla^2 \vec{\mathbf{A}} - \frac{1}{c^2} \frac{\partial^2 \vec{\mathbf{A}}}{\partial t^2} = -\mu_0 \vec{\mathbf{J}} + \vec{\nabla}\left(\vec{\nabla} \cdot \vec{\mathbf{A}} + \frac{1}{c^2} \frac{\partial \phi}{\partial t} \right). \tag{2.10}$$

Equations (2.9) and (2.10) have a total of four equations, one for the former and three for the latter, and four variables, ϕ, A_x, A_y and A_z, making them more compact than the classical Maxwell equations which have eight equations for six variables ($\vec{\mathbf{E}}$ and $\vec{\mathbf{B}}$ components).

2.1.2 Wave Equation Under Gauge Invariance

The definitions of the potentials in equations (2.7) and (2.8) allow for a gauge transformation that further simplifies equations (2.9) and (2.10). Moreover, as later discussed in section 2.4, the quantum mechanical description of radiation is described in particular gauges.

The gauge transformation, takes into consideration the curl of gradient property to conclude that replacing $\vec{\mathbf{A}} \rightarrow \vec{\mathbf{A}}'$ and $\phi \rightarrow \phi'$ in equations (2.7) and (2.8), with replacements defined by (2.11) and (2.12), guarantees that both the electric and magnetic fields stay the same.

$$\vec{\mathbf{A}} \rightarrow \vec{\mathbf{A}}' = \vec{\mathbf{A}} + \vec{\nabla}\Lambda \tag{2.11}$$

$$\phi \rightarrow \phi' = \phi - \frac{\partial \Lambda}{\partial t} \tag{2.12}$$

Here, Λ is a scalar field, and by choosing different Λ, i.e. different gauges, equations (2.9) and (2.10) can be simplified. A common gauge is the Lorenz gauge,

$$\vec{\nabla} \cdot \vec{\mathbf{A}}' + \frac{1}{c^2}\frac{\partial \phi'}{\partial t} = 0\,, \tag{2.13}$$

where the changes in $\vec{\mathbf{A}}$ and ϕ are such that the last term in equation (2.10) cancels after gauge transformation,

$$\nabla^2 \vec{\mathbf{A}}' - \frac{1}{c^2}\frac{\partial^2 \vec{\mathbf{A}}'}{\partial t^2} = -\mu_0 \vec{\mathbf{J}}_{EM}\,. \tag{2.14}$$

Additionally, inputting (2.13) into (2.9) after transformation results in a similar equation for the scalar potential:

$$\nabla^2 \phi' - \frac{1}{c^2}\frac{\partial^2 \phi'}{\partial t^2} = -\frac{\rho_{EM}}{\varepsilon_0}\,. \tag{2.15}$$

Notice that the primes can be dropped since these potentials are also valid potentials.

Another gauge, so-called Coulomb gauge, defined by $\vec{\nabla} \cdot \vec{\mathbf{A}}' = 0$ is also used. This gauge is particularly useful for source-free regions ($\rho_{EM} = 0$ and $\vec{\mathbf{J}}_{EM} = 0$) [39, 40]. In these conditions, the gauge implies that the scalar potential after transformation is $\phi = 0$, and equation (2.10) becomes the standard wave equation. The same result can also be obtained for the Lorenz gauge, i.e. in source-free regions, and equation (2.14) becomes the standard wave equation. The difference between the two gauges would be in the scalar potential, for the Coulomb gauge $\phi = 0$ while in the Lorenz gauge it would obey a standard wave equation just like the vector potential.

The solutions of the a standard wave equation can be written in terms of plane-wave expansion [41],

$$\vec{\mathbf{A}}(\vec{\mathbf{r}}, t) = \sum_{i\lambda} A_i \hat{\varepsilon}_{i\lambda}\, \mathrm{e}^{\mathrm{i}\left(\vec{\mathbf{k}}_i \cdot \vec{\mathbf{r}} - \omega_i t\right)} + A_i^* \hat{\varepsilon}_{i\lambda}^*\, \mathrm{e}^{-\mathrm{i}\left(\vec{\mathbf{k}}_i \cdot \vec{\mathbf{r}} - \omega_i t\right)}\,, \tag{2.16}$$

where the summation is over all the modes of the wave. A mode is defined by the set of values $(\vec{\mathbf{k}}_i, \hat{\varepsilon}_{i\lambda})$. Here, $\vec{\mathbf{k}}_i$ is the wave-number $k_i = \omega_i/c$ in the direction of propagation of the wave, while $\hat{\varepsilon}_{i\lambda}$ is the polarization of that mode, and is always perpendicular to $\vec{\mathbf{k}}_i$, i.e. it defines the direction of the transverse wave. For the same set i there are two linearly independent polarization directions (represented by the λ index). The discrete nature of the solutions is due the boundary conditions (confining the wave in a region of space only allows for a discrete number of solutions, if there is no boundary, there is a continuum of solutions). Separating the polarization vector into its components is not relevant in

classical theory, but it will be important in quantum theory, since the photon can only be measured to be in one of the polarizations. The polarization is an important quantity in this thesis so it will be discussed in detail in section 2.2. The complex amplitude A_i conveys information about the amplitude and the phase of the mode.

The definitions of electric and magnetic fields, given by (2.7) and (2.8) respectively, simplify to

$$\vec{\mathbf{E}} = -\frac{\partial \vec{\mathbf{A}}}{\partial t} = \sum_{i\lambda} \mathrm{i}\,\omega_i A_i \hat{\varepsilon}_{i\lambda}\, \mathrm{e}^{\mathrm{i}\left(\vec{\mathbf{k}}_i\cdot\vec{\mathbf{r}}-\omega_i t\right)} + \text{c.c.} \tag{2.17}$$

$$\vec{\mathbf{B}} = \vec{\nabla}\times\vec{\mathbf{A}} = \sum_{i\lambda} \mathrm{i}\, A_i\left(\vec{\mathbf{k}}_i \times \hat{\varepsilon}_{i\lambda}\right)\mathrm{e}^{\mathrm{i}\left(\vec{\mathbf{k}}_i\cdot\vec{\mathbf{r}}-\omega_i t\right)} + \text{c.c.} \tag{2.18}$$

where it can be noticed that the polarization vectors of the potential $\vec{\mathbf{A}}$ are the same of the electric field and, naturally, orthogonal to the those of the magnetic field. In the context of the experimental setup described in section 1.3, the consideration of source-free region is valid: Although the medium is not vacuum, but a pressurized gas of H_2 or He, the laser weakly interacts with the gas (except with the relatively few muonic atoms), this is, it is not dampened by the gas in the chamber, which is equivalent to an overall null charge density. Furthermore, since these are neutral gases, the current density is also null.

For a monochromatic field, for example an ideal laser with a single coherent mode ($\vec{\mathbf{k}}$, $\hat{\varepsilon}$), equation (2.16) can be further simplified to equation (2.19)

$$\vec{\mathbf{A}}(\vec{\mathbf{r}}, t) = A\hat{\varepsilon}\, \mathrm{e}^{\mathrm{i}\left(\vec{\mathbf{k}}\cdot\vec{\mathbf{r}}-\omega t\right)} + \text{c.c.}\,. \tag{2.19}$$

2.1.3 Momentum in Electromagnetic Field

Another quantity that is useful for the quantum mechanical description of the electromagnetic field is the momentum of a particle in the field. Considering the potential description of the Maxwell equations (2.7) and (2.8), it can be shown [39, 42] that a particle moving in an electromagnetic field has a potential energy, U_e, given by equation (2.20)

$$U_e = q\left(\phi - \vec{\mathbf{v}}\cdot\vec{\mathbf{A}}\right), \tag{2.20}$$

where q is the charge of the particle and $\vec{\mathbf{v}}$ its velocity.

Setting up the Lagrangian $\mathcal{L} = T_e - U_e$, with $T_e = m\vec{\mathbf{v}}^2/2$ being the kinetic energy, the canonical moment, $\vec{\mathbf{p}}_{can}$, associated to the position $\vec{\mathbf{r}}$ of the particle is given by equation (2.21)

$$\vec{\mathbf{p}}_{can} = \frac{\partial \mathcal{L}}{\partial \vec{\mathbf{v}}} = m\vec{\mathbf{v}} + q\vec{\mathbf{A}} = \vec{\mathbf{p}}_{kin} + q\vec{\mathbf{A}}\,. \tag{2.21}$$

The canonical momentum however is not gauge invariant, when the transformation (2.11) is applied, the resulting canonical momentum differs from the original, so it is not measurable. To work around this issue, the kinetic momentum $\vec{\mathbf{p}}_{kin}$, which is gauge invariant, is used instead. The kinetic momentum, is given by

$$\vec{\mathbf{p}}_{kin} = \vec{\mathbf{p}}_{can} - q\vec{\mathbf{A}} \tag{2.22}$$

and it is this expression that is later inputted into the Schrödinger or Dirac equations, by replacing the classical momentum with its quantum operator (when an electromagnetic field is present).

2.2 Classical Light Polarization

In section 2.1, a light beam is interpreted as a transverse wave of an oscillating electromagnetic field, i.e. an electric field and a perpendicular magnetic field that propagates perpendicularly to their direction of oscillation. The polarization of the beam is a unit vector with the direction of oscillation of the electric field.

A light beam is deemed unpolarized if the polarization vector over all the photons averages to zero. On the other hand if this average is non-null the beam is polarized with polarization equal to that average. Typical beam polarizations are the linear, circular and elliptical polarization. These will be discussed in detail in the following subsections.

Generally speaking, it can be considered that light travels in the $\hat{\mathbf{e}}_z$ direction (along the positive z axis, or $\hat{\mathbf{k}}$ direction) and oscillates in the xy plane, having two components, one in the $\hat{\mathbf{e}}_x$ direction (positive x axis) and the other in the $\hat{\mathbf{e}}_y$ direction (positive y axis) [1]. Each of these orthogonal components corresponds to a mode of oscillation. The y component has a phase shift of φ with respect to the x component. For these two modes with angular frequency ω and wavenumber k, the x and y components of the electric field are respectively,

$$\vec{\mathbf{E}}_x(z,t) = \hat{\mathbf{e}}_x E_{0x} \cos(kz - \omega t) \tag{2.23}$$

and,

$$\vec{\mathbf{E}}_y(z,t) = \hat{\mathbf{e}}_y E_{0y} \cos(kz - \omega t + \varphi)\,. \tag{2.24}$$

The total electric field is given by the sum of these perpendicular modes, equations (2.23) and (2.24), resulting in equation (2.25).

$$\vec{\mathbf{E}}(z,t) = \vec{\mathbf{E}}_x(z,t) + \vec{\mathbf{E}}_y(z,t) \tag{2.25}$$

By changing the phase shift φ, the different polarizations can be obtained.

2.2.1 Linear Polarization

In linearly polarized beams, the polarization vector is constant in both time and space, this is, the electric field oscillates in this constant direction, figure 2.1, and as such the projection of the field in the xy plane becomes a line, figure 2.1(b).

The phase difference between the x and y components is $\varphi = 0$ for linearly polarized beams [1]. From equations (2.23), (2.24), and considering the phase shift for linear polarization, the total electric field is

$$\vec{\mathbf{E}}(z,t) = (\hat{\mathbf{e}}_x E_{0x} + \hat{\mathbf{e}}_y E_{0y}) \cos(kz - \omega t) \tag{2.26}$$

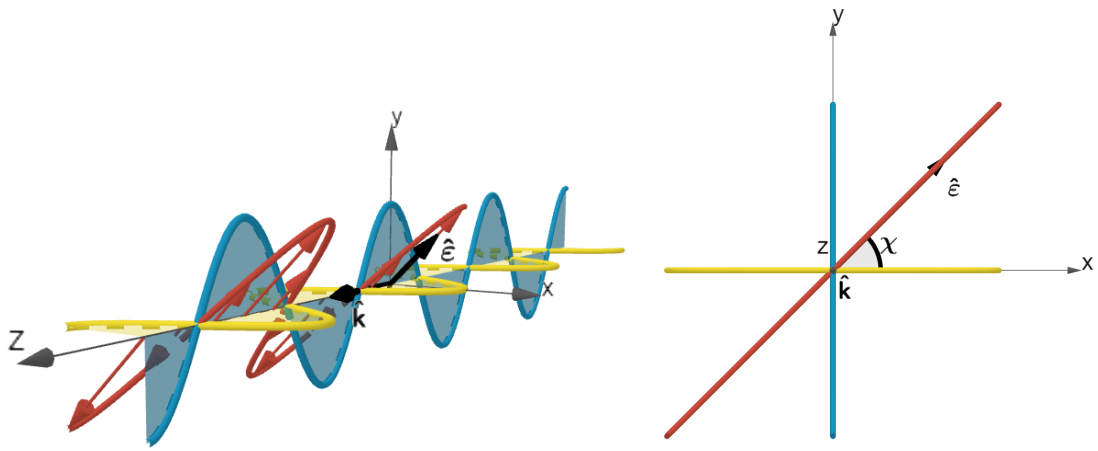

(a) Propagating linearly polarized beam.

(b) Projection of a linearly polarized beam into the xy plane.

Figure 2.1: Schematic of a linearly polarized beam (red), with the x and y components represented horizontally (in yellow) and vertically (blue), respectively. For visualization purposes, the x and y magnitudes are the same in the figures.

and the tilt angle, χ, can be calculated with

$$\tan(\chi) = \frac{E_{0y}}{E_{0x}} \,. \tag{2.27}$$

In the example of figure 2.1, $E_{0x} = E_{0y}$ which means the tilt angle is $\chi = 45°$, which can be visually verified in figure 2.1(b). Introducing equation (2.27) in equation (2.26), the electric field can be written as

$$\vec{\mathbf{E}}(z,t) = \sqrt{E_{0x}^2 + E_{0y}^2}\cos(kz - \omega t)\hat{\varepsilon} \,. \tag{2.28}$$

The polarization vector, $\hat{\varepsilon}$, in equation (2.28) is given by

$$\hat{\varepsilon} = \cos(\chi)\hat{\mathbf{e}}_x + \sin(\chi)\hat{\mathbf{e}}_y \,. \tag{2.29}$$

Note that the magnitudes of the x and y components are not necessarily positive, allowing for angles in the even quadrants of the xy plane. This is equivalent to just consider the phase shift as $\varphi = \pi$ and the magnitudes always positive.

2.2.2 Circular Polarization

In circular polarized beams, the polarization vector rotates with the propagation of the wave, which means that the direction of oscillation of the electric field rotates periodically in space, figure 2.2(a). Analogous to linear polarization, the projection of a circular polarized beam into the xy plane forms a circumference, figure 2.2(b).

The magnitudes of the x and y components are the same for circular polarization, i.e. $E_{0x} = E_{0y} = E_0$. Additionally, the phase difference is $\varphi = \pm\frac{\pi}{2}$ for clockwise or counter-clockwise polarized beams, respectively [1]. Clockwise polarization is also known as left

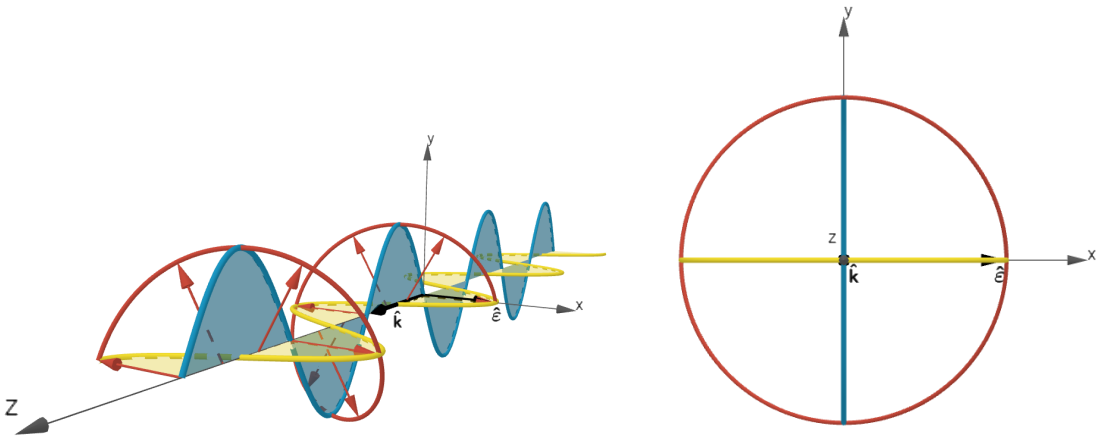

(a) Propagating right-circularly polarized beam.

(b) Projection of a circularly polarized beam into the xy plane.

Figure 2.2: Schematic of a circularly polarized beam (red), with the x and y components represented horizontally (in yellow) and vertically (blue), respectively.

circular polarization. Here, the polarization vector rotates clockwise, according to the direction of propagation, ditto for counterclockwise polarization.

The electric field for the circularly polarized beam, given by (2.25) is, for right and left polarization respectively

$$\vec{\mathbf{E}}(z,t) = E_0\Big(\hat{\mathbf{e}}_x \cos(kz-\omega t) \pm \hat{\mathbf{e}}_y \sin(kz-\omega t)\Big). \tag{2.30}$$

From equation (2.30), the electric field has always the same magnitude, but the direction changes with the propagation of the wave. These two modes given in exponential form (as in equation (2.17)) becomes

$$\begin{aligned}\vec{\mathbf{E}}(z,t) &= \frac{E_0}{2}\Big(\mathrm{e}^{\mathrm{i}(kz-\omega t)}\left(\hat{\mathbf{e}}_x \mp \mathrm{i}\,\hat{\mathbf{e}}_y\right) + \mathrm{e}^{-\mathrm{i}(kz-\omega t)}\left(\hat{\mathbf{e}}_x \pm \mathrm{i}\,\hat{\mathbf{e}}_y\right)\Big) \\ &= \frac{E_0}{2}\,\mathrm{e}^{\mathrm{i}(kz-\omega t)}\left(\hat{\mathbf{e}}_x \mp \mathrm{i}\,\hat{\mathbf{e}}_y\right) + \text{c.c.}\end{aligned} \tag{2.31}$$

with c.c. meaning complex conjugate. The polarization (normalized) vector is

$$\hat{\varepsilon} = \frac{\hat{\mathbf{e}}_x \mp \mathrm{i}\,\hat{\mathbf{e}}_y}{\sqrt{2}} \tag{2.32}$$

for right and left polarization respectively.

Analogous to linear polarization, the magnitudes of the x and y components of the electric field do not have to necessarily be equal, they can be the negative of one another, if $\varphi = -\frac{\pi}{2}$ is always considered. In this analysis, when $E_{0x} = E_{0y}$ the beam is right polarized, if $E_{0x} = -E_{0y}$ the beam is left polarized.

2.2.3 Elliptical Polarization

Elliptical polarization happens for phase shifts other than a multiple of $\frac{\pi}{2}$. Analogous to the other polarizations, elliptical polarization gets it's name from the projection of the electric field into the xy plane, figure 2.3(b).

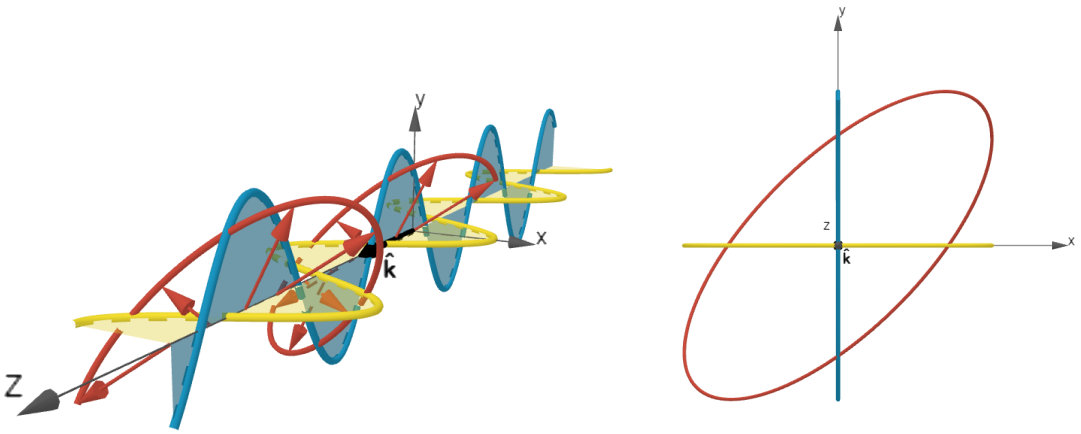

(a) Propagating right-elliptically polarized beam. Tilted ellipse.

(b) Projection of an elliptically polarized beam into the xy plane. Tilted ellipse.

Figure 2.3: Schematic of an elliptically (tilted ellipse) polarized beam (red), with the x and y components represented horizontally (in yellow) and vertically (blue), respectively.

The approach of a general elliptical polarization follows from [1] and this reference contains a deduction for the form of the projection in xy plane by expanding $\cos(kz-\omega t+\varphi)$ into a sum of cosines. Although helpful to understand the shape of the electric field, it is not appropriate for a quantum description of the polarization vector.

Instead a different approach will be considered by choosing an arbitrary amplitude in one of the modes, e.g. $\hat{\mathbf{e}}_x$, and fixing a relative amplitude for the other mode. The phase between the modes is $\varphi = \pi/2$, as in the circular right polarization case.

By considering this phase shift, the axis of the ellipse are coincident with the x and y axis. Their magnitudes however are not the same, they differ by a factor of η, $E_{0y} = \eta E_{0x}$, figure 2.4(b). This value η can be anything between -1 and 1, which guaranties that the major axis of the ellipse is in the x axis and the minor axis is in the y axis, and allows for left and right polarizations.

The electric field thus become

$$\vec{\mathbf{E}}(z,t) = E_0\Big(\hat{\mathbf{e}}_x \cos(kz-\omega t) + \hat{\mathbf{e}}_y \eta \sin(kz-\omega t)\Big), \tag{2.33}$$

where $E_0 = E_{0x}$. Expanding the sine and cosine to their exponential forms, results in

$$\begin{aligned}\vec{\mathbf{E}}(z,t) &= \frac{E_0}{2}\Big(\mathrm{e}^{\mathrm{i}(kz-\omega t)}\Big(\hat{\mathbf{e}}_x - \eta\,\mathrm{i}\,\hat{\mathbf{e}}_y\Big) + \mathrm{e}^{-\mathrm{i}(kz-\omega t)}\Big(\hat{\mathbf{e}}_x + \eta\,\mathrm{i}\,\hat{\mathbf{e}}_y\Big)\Big) \\ &= \frac{E_0}{2}\,\mathrm{e}^{\mathrm{i}(kz-\omega t)}\Big(\hat{\mathbf{e}}_x - \eta\,\mathrm{i}\,\hat{\mathbf{e}}_y\Big) + \text{c.c.}\,,\end{aligned} \tag{2.34}$$

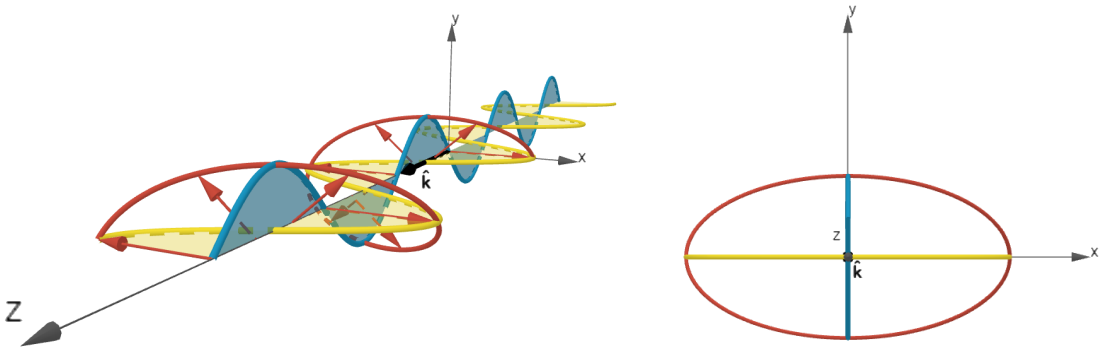

(a) Propagating right-elliptically polarized beam. Horizontal ellipse.

(b) Projection of an elliptically polarized beam into the xy plane. Horizontal ellipse.

Figure 2.4: Schematic of an elliptically (horizontal ellipse) polarized beam (red), with the x and y components represented horizontally (in yellow) and vertically (blue), respectively.

and the (normalized) polarization vector is

$$\hat{\varepsilon} = \frac{\hat{\mathbf{e}}_x - \eta\, \mathrm{i}\, \hat{\mathbf{e}}_y}{\sqrt{1+\eta^2}}\,. \tag{2.35}$$

which is the form used in references [43, 44].

From equations (2.33), (2.34) and (2.35), four important observations are:

- if $\eta < 0$, $\vec{\mathbf{E}}$ rotates clockwise and is left polarized;
- if $\eta > 0$, $\vec{\mathbf{E}}$ rotates counter-clockwise and is right polarized;
- if $\eta = 0$, $\vec{\mathbf{E}}$ is linear polarized in the $\hat{\mathbf{e}}_x$ direction;
- if $\eta = \pm 1$, right or left circular polarizations are obtained, respectively.

The last four statements allows to conclude that the parameter η generalizes the type of polarization. Within its range, linear, circular and elliptical polarizations can be obtained, including left and right polarizations.

To generalize to tilted ellipses, see figure 2.5, a rotation to the frame has to be applied, i.e., instead of the major axis of the ellipse being in the x direction, it is in a generic $\hat{\varepsilon}_{\parallel}$ direction, and the minor axis is in a perpendicular direction, $\hat{\varepsilon}_{\perp} = \hat{\mathbf{k}} \times \hat{\varepsilon}_{\parallel}$. Changing these two vectors in equation (2.35), a final expression for the polarization vector is obtained in (2.36)

$$\hat{\varepsilon} = \frac{\hat{\varepsilon}_{\parallel} - \eta\, \mathrm{i}\, \hat{\varepsilon}_{\perp}}{\sqrt{1+\eta^2}}\,. \tag{2.36}$$

To further generalize to any direction of propagation, the kz term in the exponential just has to be replaced by $\vec{\mathbf{k}} \cdot \vec{\mathbf{r}}$, and the polarization vector is a generalized unit vector of

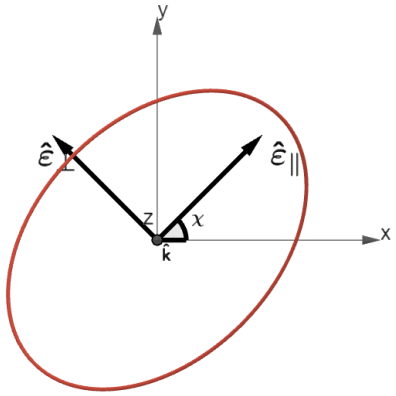

Figure 2.5: Projection of elliptically polarized beam into the xy plane, with the vector units of direction of each component of the electric field.

the form (2.36). The electric field is then expressed has

$$\vec{\mathbf{E}}(\vec{\mathbf{r}},t) = \sqrt{1+\eta^2}\frac{E_0}{2}\hat{\varepsilon}\,\mathrm{e}^{\mathrm{i}\left(\vec{\mathbf{k}}\cdot\vec{\mathbf{r}}-\omega t\right)} + \text{c.c.}\,. \tag{2.37}$$

Here, it is important to notice the similarity between this electric field and the one deduced in equation (2.17), considering only one mode.

Without loss of generality, $\hat{\varepsilon}_\parallel$ can be considered to make an angle of χ with the x axis, then it can be expressed as

$$\hat{\varepsilon}_\parallel = \cos(\chi)\hat{\mathbf{e}}_x + \sin(\chi)\hat{\mathbf{e}}_y = -\frac{\mathrm{e}^{-\mathrm{i}\chi}}{\sqrt{2}}\hat{\mathbf{e}}_+ + \frac{\mathrm{e}^{\mathrm{i}\chi}}{\sqrt{2}}\hat{\mathbf{e}}_-\,, \tag{2.38}$$

and

$$\hat{\varepsilon}_\perp = -\sin(\chi)\hat{\mathbf{e}}_x + \cos(\chi)\hat{\mathbf{e}}_y = \mathrm{i}\frac{\mathrm{e}^{-\mathrm{i}\chi}}{\sqrt{2}}\hat{\mathbf{e}}_+ + \mathrm{i}\frac{\mathrm{e}^{\mathrm{i}\chi}}{\sqrt{2}}\hat{\mathbf{e}}_-\,, \tag{2.39}$$

where $\hat{\mathbf{e}}_+$ and $\hat{\mathbf{e}}_-$ are two orthogonal vectors of the spherical basis set. This basis is more convenient when evaluating matrix elements, see more details in appendix A. Introducing equations (2.38) and (2.39) into (2.36), results in

$$\hat{\varepsilon} = \frac{\mathrm{e}^{-\mathrm{i}\chi}}{\sqrt{2}}\frac{\eta-1}{\sqrt{\eta^2+1}}\hat{\mathbf{e}}_+ + \frac{\mathrm{e}^{\mathrm{i}\chi}}{\sqrt{2}}\frac{\eta+1}{\sqrt{\eta^2+1}}\hat{\mathbf{e}}_-\,, \tag{2.40}$$

and here it can be noticed again that the electric field (and consequently, the magnetic field), will not have any component in the direction of propagation (z axis).

Two quantities can be defined, the degree of circular polarization (which is the Stoke parameter V_S),

$$P_c = |\hat{\varepsilon}_-|^2 - |\hat{\varepsilon}_+|^2 = \frac{2\eta}{\eta^2+1}\,, \tag{2.41}$$

and the degree of linear polarization (which is the Stoke parameter Q_S) with equation (2.36)

$$P_l = \left|(\hat{\varepsilon})_\parallel\right|^2 - |(\hat{\varepsilon})_\perp|^2 = \frac{1-\eta^2}{\eta^2+1}\,. \tag{2.42}$$

Note that $(\hat{\varepsilon})_{\|}$ is not the same as $\hat{\varepsilon}_{\|}$, it is rather the parallel component of the $\hat{\varepsilon}$ vector, i.e. the quantity that multiplies by $\hat{\varepsilon}_{\|}$ in equation (2.36). Same goes for the perpendicular component.

2.3 Quantum Description of the Atom

Before proceeding with the quantum description of the interaction of the electromagnetic with the atom is worthwhile to review the necessary quantum theory of the atom.

Following standard quantum mechanics, the atomic structure of an atom is the set of eigenstates that satisfy the eigenvalue equation of the Hamiltonian,

$$H\Psi = E\Psi\,, \tag{2.43}$$

where H is the Hamiltonian operator and Ψ an eigenstate with eigenvalue (energy) E.

The Hamiltonian is very general and can be applied to a diverse range of quantum systems with arbitrary number of particles, as well as mutual interactions and external fields. In the particular case of an two-particle system, such as hydrogen, or muonic hydrogen, the Hamiltonian can be further reduced to the single-particle Hamiltonian for the center-of-mass coordinates. Furthermore, in the present system of the single one-charge plus nucleus, only the Coulomb potential is present as the interaction in the Hamiltonian. We also do not consider relativistic and recoil effects in this instantaneous Coulomb interaction. From now on we only consider the atomic Hamiltonian, which is known as a central-field or radial Hamiltonian.

In order to have an accurate description of the atom, both relativistic (with the Dirac Hamiltonian) and QED effects must be considered. In this thesis, only the Dirac Hamiltonian will be considered, and the QED effects will be included later (in the gyroscopic factor).

Although the atomic system is well-defined by the non-relativistic Schrödinger equation, it is more convenient to consider the relativistic equation for retrieving the magnetic dipole transition, which easier to obtain with a relativistic treatment. The Dirac Hamiltonian, equation (2.44) is a relativistic version of the Schrödinger Hamiltonian. It was first constructed by turning linear the relativistic kinetic energy of a particle, $E^2 = p^2c^2 + m^2c^4$. Dirac realized this could be done if the coefficients were matrices

$$h_D = c\vec{\alpha}\cdot\vec{\mathbf{p}} + \beta mc^2 + V(\vec{\mathbf{r}})\,. \tag{2.44}$$

In the Dirac Hamiltonian h_D, m is the particle rest mass, c the speed of light, and $V(\vec{\mathbf{r}})$ is the potential energy. $\vec{\alpha}$ and β are 4×4 matrices given by (2.45)

$$\vec{\alpha} = \begin{bmatrix} 0 & \vec{\sigma} \\ \vec{\sigma} & 0 \end{bmatrix}, \quad \beta = \begin{bmatrix} \mathbb{1}_{2\times 2} & 0 \\ 0 & -\mathbb{1}_{2\times 2} \end{bmatrix} \tag{2.45}$$

where $\vec{\sigma}$ is the Pauli vector given by

$$\vec{\sigma} = \sigma_x\hat{\mathbf{e}}_x + \sigma_y\hat{\mathbf{e}}_y + \sigma_z\hat{\mathbf{e}}_z\,, \tag{2.46}$$

which takes the corresponding Pauli matrix for each direction.

$$\sigma_x = \begin{bmatrix} 0 & 1 \\ 1 & 0 \end{bmatrix}, \quad \sigma_y = \begin{bmatrix} 0 & -i \\ i & 0 \end{bmatrix}, \quad \sigma_z = \begin{bmatrix} 1 & 0 \\ 0 & -1 \end{bmatrix}. \tag{2.47}$$

The Dirac Hamiltonian does not commute with the angular momentum $\vec{\mathbf{L}}^2$ and neither with spin $\vec{\mathbf{S}}^2$, which means these are no longer good quantum numbers unlike in the Schrödinger Hamiltonian. However, it does commute with J^2, where $\vec{\mathbf{J}}$ is the total angular momentum $\vec{\mathbf{J}} = \vec{\mathbf{L}} + \vec{\mathbf{S}}$. The eigenstates of h_D are also eigenstates of $\vec{\mathbf{J}}^2$ and J_z.

Spherical spinors, $\Omega_{\kappa m_J}$, can be constructed by coupling the angular orbital momentum and with the spin [41]. These spinors convey the complete angular distribution of the wave-function, they are analogous to the spherical harmonics in the non-relativistic case.

The complete solution for the eigenvalue problem with a central field ($V(\vec{\mathbf{r}}) = V(r)$) is given by equation (2.48)

$$\Psi_{n\kappa} = \frac{1}{r}\begin{bmatrix} \mathrm{i}\, P_{n\kappa}(r)\Omega_{\kappa m_J} \\ Q_{n\kappa}(r)\Omega_{-\kappa m_J} \end{bmatrix}. \tag{2.48}$$

This solution has four components (each spinor has two components), but can be analyzed as if it has two components, a large component, the $P_{n\kappa}$ term, and a small component, the $Q_{n\kappa}$ term. The m_J index is the quantum number associated with J_z, and κ is a quantum number related with the operator $\vec{\mathbf{J}}$, such that $\kappa = \mp(j+1/2)$ for $j = l \pm 1/2$ and l is the orbital angular momentum of the large component (note that $\vec{\mathbf{L}}^2$ computes different expectation values for the large and small component, $l_{large} = l_{small} \mp 1$ for $j = l_{large} \pm 1/2$).

Introducing the solution (2.48) into the tridimensional Hamiltonian, it is obtained a coupled system of radial equations for $P_{n\kappa}$ and $Q_{n\kappa}$

$$\left(V + mc^2\right)P_{n\kappa} + \hbar c\left(\frac{\mathrm{d}}{\mathrm{d}r} - \frac{\kappa}{r}\right)Q_{n\kappa} = E_{n\kappa}P_{n\kappa} \tag{2.49}$$

$$-\hbar c\left(\frac{\mathrm{d}}{\mathrm{d}r} + \frac{\kappa}{r}\right)P_{n\kappa} + \left(V - mc^2\right)Q_{n\kappa} = E_{n\kappa}Q_{n\kappa}\,. \tag{2.50}$$

For a Coulomb potential, $V(r) = \frac{-\hbar c\alpha Z}{r}$, with α the fine structure constant and Z the number of protons in the nucleus, the energy eigenvalues can be found to be

$$E_{n\kappa} = \frac{mc^2}{\sqrt{1 + \frac{\alpha^2 Z^2}{\left(n - |\kappa| + \sqrt{|\kappa|^2 - \alpha^2 Z^2}\right)^2}}}\,. \tag{2.51}$$

where the principal quantum number n, has the same meaning as in the Schrödinger solution.

2.3.1 Pauli Approximation

The relativistic expression for the kinetic energy is $E - V = \sqrt{m^2c^4 + p^2c^2}$, with E being the total energy and V the potential energy. The m^2c^4 term is usually much greater than the p^2c^2 term, so this energy can be approximated to $E - V \approx mc^2$. With this information, equation (2.50) simplifies to

$$Q_\kappa = -\frac{\hbar c}{2mc^2}\left(\frac{\mathrm{d}}{\mathrm{d}r} + \frac{\kappa}{r}\right)P_\kappa \,, \tag{2.52}$$

and equation (2.49) simplifies to

$$\left(-\frac{\hbar^2}{2m}\left(\frac{\mathrm{d}^2}{\mathrm{d}r^2}\right) - \frac{\kappa(\kappa+1)}{r^2} + V(r)\right)P_\kappa = \left(E_{n\kappa} - mc^2\right)P_\kappa \,. \tag{2.53}$$

Equation (2.53) is the non-relativistic Schrödinger equation for a particle with energy $E_{n\kappa} - mc^2$, which is the energy relative to the rest mass energy. It is also important to notice that the product $\kappa(\kappa+1)$ is always $l(l+1)$, for either $j = l \pm 1/2$. With the same approximation, the generic solution for the Dirac Hamiltonian is

$$\Psi \approx \begin{bmatrix} \Phi \\ \frac{\vec{\sigma}\cdot\vec{\mathbf{p}}}{2mc}\Phi \end{bmatrix}, \tag{2.54}$$

which generalizes equation (2.53) to

$$\frac{\vec{\mathbf{p}}^2}{2m}\Phi + V(r)\Phi = \left(E_{nl} - mc^2\right)\Phi \,. \tag{2.55}$$

2.4 Quantized Electromagnetic field

A quantum description of the electromagnetic field in a box of volume V can be achieved by turning the A_i and A_i^* of equation (2.16) into operators c_i and $c_i^\dagger$ respectively, with a normalization factor coming from boundary conditions of $\sqrt{\hbar/2\varepsilon_0\omega_i V}$, obtaining equation (2.56)

$$\vec{\mathbf{A}}(\vec{\mathbf{r}},t) = \sum_{i\lambda}\sqrt{\frac{\hbar}{2\varepsilon_0\omega_i V}}\left(c_i\hat{\varepsilon}_{i\lambda}\,\mathrm{e}^{\mathrm{i}\left(\vec{\mathbf{k}}_i\cdot\vec{\mathbf{r}}-\omega_i t\right)} + c_i^\dagger\hat{\varepsilon}_{i\lambda}^*\,\mathrm{e}^{-\mathrm{i}\left(\vec{\mathbf{k}}_i\cdot\vec{\mathbf{r}}-\omega_i t\right)}\right). \tag{2.56}$$

The c_i and $c_i^\dagger$ are the annihilation and creation operators that follow the commutator relations in equation (2.57)

$$\left[c_i, c_j\right] = 0\,, \quad \left[c_i^\dagger, c_j^\dagger\right] = 0\,, \quad \left[c_i, c_j^\dagger\right] = \delta_{ij}\,. \tag{2.57}$$

The electromagnetic Hamiltonian can be obtained from classical electromagnetic relations [39, 41], by using the quantified form of the vector potential (2.56) and the classical relations (2.17) and (2.18). With the commutation relations, the total energy of the quantized electromagnetic field is given by

$$H_{EM} = \frac{\varepsilon_0}{2}\int \mathrm{d}^3\vec{\mathbf{r}}\,\vec{\mathbf{E}}(\vec{\mathbf{r}},t)\cdot\vec{\mathbf{E}}(\vec{\mathbf{r}},t) + \frac{1}{2\mu_0}\int \mathrm{d}^3\vec{\mathbf{r}}\,\vec{\mathbf{B}}(\vec{\mathbf{r}},t)\cdot\vec{\mathbf{B}}(\vec{\mathbf{r}},t)$$

$$= \sum_i \hbar\omega_i \left(\mathcal{N}_i + \frac{1}{2}\right), \tag{2.58}$$

where $\mathcal{N}_i = c_i^\dagger c_i$ is photon number operator. Equation (2.58), implies that the vacuum state has an energy of $\sum_i \frac{\hbar\omega_i}{2}$, the zero-point energy. This value is not measurable, so it is not considered in the Hamiltonian. It can be concluded that a state $|n\rangle$, of n photons with frequency ω, has a total energy of $n \times \hbar\omega$, which is the known Planck relation of each photon having an energy of $\hbar\omega$.

The creation and annihilation operators have the effect of raising or lowering, respectively, the number of photons of the state and can be evaluated to

$$c^\dagger |n\rangle = \sqrt{n+1}\,|n+1\rangle \tag{2.59}$$

$$c\,|n\rangle = \sqrt{n}\,|n-1\rangle\ , \tag{2.60}$$

where the states represent the number of photons of the particular energy in consideration.

2.5 Interaction Hamiltonian

The interaction Hamiltonian for a charged particle in an electromagnetic field is obtained by replacing the momentum operator in the Dirac Hamiltonian with the classical momentum shown in equation (2.22). Additionally, the time derivative in the time dependent Hamiltonian, $\mathrm{i}\hbar\frac{\partial}{\partial t}$ (zeroth component of the momentum four-vector), must be replaced with $\mathrm{i}\hbar\frac{\partial}{\partial t} - q\phi$ (zeroth component of the four potential in an electromagnetic field). To maintain the conventional forms of the momentum and the time dependent Hamiltonian, the atomic Hamiltonian, H_A, can thus be written with equation (2.61).

$$\begin{aligned} H_A &= c\vec{\alpha}\cdot\left(\vec{\mathbf{p}} - q\vec{\mathbf{A}}\right) + \beta mc^2 + V(\vec{\mathbf{r}}) + q\phi \\ &= h_D - cq\vec{\alpha}\cdot\vec{\mathbf{A}}(\vec{\mathbf{r}}, t) + q\phi \\ &= h_D + H_I(t) \end{aligned} \tag{2.61}$$

For the Coulomb gauge discussed in section 2.1.2, $\phi = 0$, and the interaction Hamiltonian (2.62) is obtained with equation (2.56)

$$H_I(t) = \sum_{i\lambda} h_I(\vec{\mathbf{r}}, \omega_i) c_i\, \mathrm{e}^{-\mathrm{i}\omega_i t} + h_I^\dagger(\vec{\mathbf{r}}, \omega_i) c_i^\dagger\, \mathrm{e}^{\mathrm{i}\omega_i t}\ , \tag{2.62}$$

where the charge q was replaced by the charge of the orbiting particle, in this case a muon which has the same charge of an electron, $-e$. The $h_I(\vec{\mathbf{r}}, \omega)$ Hamiltonian is given by

$$h_I(\vec{\mathbf{r}}, \omega) = ec\sqrt{\frac{\hbar}{2\varepsilon_0 \omega V}}\,\vec{\alpha}\cdot\hat{\varepsilon}_\lambda\, \mathrm{e}^{\mathrm{i}\vec{\mathbf{k}}\cdot\vec{\mathbf{r}}} \tag{2.63}$$

2.6 Dynamic of Photon - Atomic System

Considering now a system composed of atoms and the radiation field, the total Hamiltonian is given by the atomic Hamiltonian, plus the electromagnetic Hamiltonian, $H = H_A + H_{EM} = h_D + H_{EM} + H_I$. This total Hamiltonian can be separated in two parts, a non-perturbative Hamiltonian $H_0 = h_D + H_{EM}$, and a perturbation Hamiltonian, H_I. A solution to the non-perturbative Hamiltonian is

$$H_0 \left|\psi_k(t), \{n\}\right\rangle = \mathrm{i}\hbar \frac{\partial \left|\psi(t), \{n\}\right\rangle}{\partial t} = \left(E_k + \sum_j n_j \hbar \omega_j \right) \left|\psi_k(t), \{n\}\right\rangle , \tag{2.64}$$

where the eigenstate $\left|\psi_k(t), \{n\}\right\rangle = \left|\psi_k(t)\right\rangle |\{n\}\rangle$ is the product of the Dirac Hamiltonian eigenstate, $\left|\psi_k(t)\right\rangle = \mathrm{e}^{-i\frac{E_k}{\hbar}t} \left|\psi_k\right\rangle$, with the electromagnetic Hamiltonian eigenstate $|\{n\}\rangle = |n_0\rangle |n_1\rangle |n_2\rangle ....$ The individual states $|n_i\rangle$ represent a state of n_i photons with frequency ω_i, and the initial state of the radiation field is imposed by the radiation that is being applied to the system, i.e. the laser light. A complete solution for (2.64), is just the sum over all possible $\left|\psi_k(t)\right\rangle$ states

$$|\Psi_0(t)\rangle = \sum_k a_k \left|\psi_k(t), \{n\}\right\rangle , \tag{2.65}$$

with the amplitude coefficients a_k, acting as complex amplitudes for each solution $\left|\psi_k(t), \{n\}\right\rangle$.

Assuming that the eigenstates of the total Hamiltonian can be written with linear combinations of the eigenstates of the non-perturbative Hamiltonian, this is, they share a basis set of solutions, then the $|\Psi_0(t)\rangle$ solution of equation (2.65) can be inputted into the total Hamiltonian $H_0 + H_I = \mathrm{i}\hbar \frac{\partial}{\partial t}$, and the a_k coefficients are allowed to vary with time, as long as the normalization of $|\Psi_0(t)\rangle$ holds. With the explicit time dependence of the coefficients a_k, and by applying the time derivative to the $|\Psi_0(t)\rangle$ state, equation (2.66) is obtained,

$$\sum_k \mathrm{i}\hbar \frac{\partial a_k(t)}{\partial t} \left|\psi(t), \{n\}\right\rangle + \mathrm{i}\hbar a_k(t) \frac{\partial \left|\psi(t), \{n\}\right\rangle}{\partial t} = \sum_k a_k(t) H_0 \left|\psi(t), \{n\}\right\rangle + a_k(t) H_I \left|\psi(t), \{n\}\right\rangle . \tag{2.66}$$

With help from equation (2.64), it is immediate that the second term of the left-hand side of equation (2.66) is the same as the first term from the right-hand side, which simplifies equation (2.66) to

$$\sum_k \mathrm{i}\hbar \frac{\partial a_k(t)}{\partial t} \left|\psi(t), \{n\}\right\rangle = \sum_k a_k(t) H_I \left|\psi(t), \{n\}\right\rangle \tag{2.67}$$

Equation (2.67) can now be projected into the another state $\sum_{\{n'\}} \left|\psi'_k(t), \{n'\}\right\rangle$, for which there is no interest in the final state of the radiation field, thus the summation for all possible $|\{n'\}\rangle$, defining $\omega_{kk'} = \frac{E_{k'} - E_k}{\hbar}$ gives

$$\mathrm{i}\hbar \frac{\partial a_{k'}(t)}{\partial t} = \sum_{k\{n'\}} a_k(t) \mathrm{e}^{\mathrm{i}\omega_{k'k}t} \sum_{i\lambda} \left\langle \psi_{k'} \right| h_I(\vec{\mathbf{r}}, \omega_i) \left|\psi_k\right\rangle \left\langle \{n'\} \right| c_i \left|\{n\}\right\rangle \mathrm{e}^{-\mathrm{i}\omega_i t}$$

$$+\langle\psi_{k'}\big|h_I^\dagger(\vec{\mathbf{r}},\omega_i)\big|\psi_k\rangle\,\langle\{n'\}\big|c_i^\dagger\big|\{n\}\rangle\,\mathrm{e}^{\mathrm{i}\omega_i t}\ .$$

For each mode i, there are only two possible $\{n'\}$ for which the terms in the summation are not null, one for photon absorption (first term on right-hand side of (2.68)) and the other for photon emission (second term on right-hand side of (2.68))

$$\mathrm{i}\hbar\frac{\partial a_{k'}(t)}{\partial t}=\sum_{ki\lambda}a_k(t)\,\mathrm{e}^{\mathrm{i}\omega_{k'k}t}\Big(\langle\psi_{k'}\big|h_I(\vec{\mathbf{r}},\omega_i)\big|\psi_k\rangle\,\langle n_i-1|c_i|n_i\rangle\,\mathrm{e}^{-\mathrm{i}\omega_i t}$$
$$+\langle\psi_{k'}\big|h_I^\dagger(\vec{\mathbf{r}},\omega_i)\big|\psi_k\rangle\,\langle n_i+1|c_i^\dagger|n_i\rangle\,\mathrm{e}^{\mathrm{i}\omega_i t}\Big)\,. \tag{2.68}$$

Equation (2.68), describes the motion of the wave-function (closely related to the probabilities of finding the particle in a particular state, see chapter 3).

2.6.1 Transition Matrix Elements

In order to further simplify equation (2.68), it is necessary to evaluate the matrix elements $T^{\mathrm{abs}}_{k'k}=\langle\psi_{k'}\big|h_I(\vec{\mathbf{r}},\omega)\big|\psi_k\rangle$ and $T^{\mathrm{ems}}_{k'k}=\langle\psi_{k'}\big|h_I^\dagger(\vec{\mathbf{r}},\omega)\big|\psi_k\rangle$. This evaluation is obtained via two approximations, the Pauli approximation (section 2.3.1) and the multipole expansion.

Firstly, to avoid repetition, the proportionality coefficient in the interaction Hamiltonian (2.63), $ec\sqrt{\frac{\hbar}{2\varepsilon_0\omega V}}$, will be omitted. The absorption matrix element is then given by equation (2.69),

$$\begin{aligned}T^{\mathrm{abs}}_{k'k}&\propto\langle\psi_{k'}\big|\vec{\alpha}\cdot\hat{\varepsilon}_\lambda\,\mathrm{e}^{\mathrm{i}\vec{\mathbf{k}}\cdot\vec{\mathbf{r}}}\big|\psi_k\rangle\\&=\int\mathrm{d}^3\vec{\mathbf{r}}\begin{bmatrix}\phi^\dagger_{k'} & \phi^\dagger_{k'}\frac{\vec{\sigma}\cdot\vec{\mathbf{p}}}{2mc}\end{bmatrix}\begin{bmatrix}0 & \vec{\sigma}\cdot\hat{\varepsilon}_\lambda\\ \vec{\sigma}\cdot\hat{\varepsilon}_\lambda & 0\end{bmatrix}\mathrm{e}^{\mathrm{i}\vec{\mathbf{k}}\cdot\vec{\mathbf{r}}}\begin{bmatrix}\phi_k\\ \frac{\vec{\sigma}\cdot\vec{\mathbf{p}}}{2mc}\phi_k\end{bmatrix}\\&=\int\mathrm{d}^3\vec{\mathbf{r}}\,\frac{\mathrm{e}^{\mathrm{i}\vec{\mathbf{k}}\cdot\vec{\mathbf{r}}}}{2mc}\phi^\dagger_{k'}\Big(2\vec{\mathbf{p}}\cdot\hat{\varepsilon}_\lambda+\mathrm{i}\hbar\vec{\sigma}\cdot\big(\vec{\mathbf{k}}\times\hat{\varepsilon}_\lambda\big)\Big)\phi_k\,,\end{aligned} \tag{2.69}$$

where ϕ_k represents the large component of the corresponding ψ_k wave-function.

While it is usual to expand the term $\mathrm{e}^{\mathrm{i}\vec{\mathbf{k}}\cdot\vec{\mathbf{r}}}$ in so-called irreducible tensors [41], to obtain the most important multipoles is sufficient to make the simple approximation $\mathrm{e}^{\mathrm{i}\vec{\mathbf{k}}\cdot\vec{\mathbf{r}}}\approx 1+\mathrm{i}\,\vec{\mathbf{k}}\cdot\vec{\mathbf{r}}$, and neglect the $\vec{\mathbf{k}}\cdot\vec{\mathbf{r}}\vec{\sigma}\cdot\big(\vec{\mathbf{k}}\times\hat{\varepsilon}_\lambda\big)$ term, in order to obtain the M1 transition, which as we shall see, is the multipole of the HFS transition. . In the following equation, it was taken into account that the spin operator is $\vec{\mathbf{S}}=\frac{\hbar}{2}\vec{\sigma}$.

$$\begin{aligned}T^{\mathrm{abs}}_{k'k}&\propto\int\mathrm{d}^3\vec{\mathbf{r}}\frac{1}{2mc}\phi^\dagger_{k'}\Big(2\vec{\mathbf{p}}\cdot\hat{\varepsilon}_\lambda+2\,\mathrm{i}\,\vec{\mathbf{k}}\cdot\vec{\mathbf{r}}\vec{\mathbf{p}}\cdot\hat{\varepsilon}_\lambda+2\,\mathrm{i}\,\vec{\mathbf{S}}\cdot\big(\vec{\mathbf{k}}\times\hat{\varepsilon}_\lambda\big)\Big)\phi_k\\&=\frac{1}{mc}\langle\phi_{k'}\big|\vec{\mathbf{p}}\cdot\hat{\varepsilon}_\lambda\big|\phi_k\rangle+\frac{\mathrm{i}}{2mc}\langle\phi_{k'}\big|\big(\vec{\mathbf{L}}+2\vec{\mathbf{S}}\big)\cdot\big(\vec{\mathbf{k}}\times\hat{\varepsilon}_\lambda\big)\big|\phi_k\rangle+\frac{\mathrm{i}}{2mc}\langle\phi_{k'}\big|\vec{\mathbf{k}}\cdot\vec{\mathbf{r}}\vec{\mathbf{p}}\cdot\hat{\varepsilon}_\lambda+\vec{\mathbf{r}}\cdot\hat{\varepsilon}_\lambda\vec{\mathbf{p}}\cdot\vec{\mathbf{k}}\big|\phi_k\rangle\\&=\mathcal{M}^{E1}_{k'k}\cdot\hat{\varepsilon}_\lambda+\mathrm{i}\,\mathcal{M}^{M1}_{k'k}\cdot\big(\vec{\mathbf{k}}\times\hat{\varepsilon}_\lambda\big)+\ldots\,,\end{aligned} \tag{2.70}$$

Where the matrix element $\vec{\mathcal{M}}^{\mathrm{E1}}_{k'k}$ corresponds to the E1 transition,

$$\vec{\mathcal{M}}^{\mathrm{E1}}_{k'k}=\frac{1}{mc}\langle\phi_{k'}\big|\vec{\mathbf{p}}\big|\phi_k\rangle\,, \tag{2.71}$$

and $\vec{\mathcal{M}}^{\mathrm{M1}}_{k'k}$ corresponds to the M1 transition

$$\vec{\mathcal{M}}^{\mathrm{M1}}_{k'k} = \frac{1}{2mc}\langle\phi_{k'}\big|\vec{\mathbf{L}} + 2\vec{\mathbf{S}}\big|\phi_k\rangle\,. \tag{2.72}$$

On the second line of (2.70), the last term corresponds to the electric quadrupole transition, but this term has no relevance for this thesis, as the transition between the $F = 0$ and $F = 1$ states is forbidden due to selection rules of the Electric Quadrupole (E2) transition [45] ($\Delta F = 0, \pm 1, \pm 2$ but $F = 0 \nrightarrow F = 0, 1$ and $F = 1/2 \nrightarrow F = 1/2$). This term was then dropped for simplicity.

The selection rules arises from the evaluation of these matrix elements. For example, for E1 transitions, selection rules prevents transitions between states with same principal quantum number and L, which is the type of transition of the HFS. Thus the E1 is forbidden and suppressed. The next relevant term is the M1 multipole which gives the majority of the contribution.

Finally the coefficients omitted at the beginning can be brought back,

$$T^{\mathrm{abs}}_{k'k} = ec\vec{\mathcal{M}}^{\mathrm{M1}}_{k'k}\cdot\left(\mathrm{i}\sqrt{\frac{\hbar}{2\varepsilon_0\omega V}}\vec{\mathbf{k}}\times\hat{\varepsilon}_\lambda\right), \tag{2.73}$$

and applying the same reasoning for the emission matrix element gives

$$T^{\mathrm{ems}}_{k'k} = ec\vec{\mathcal{M}}^{\mathrm{M1}}_{k'k}\cdot\left(-\mathrm{i}\sqrt{\frac{\hbar}{2\varepsilon_0\omega V}}\vec{\mathbf{k}}\times\hat{\varepsilon}^*_\lambda\right). \tag{2.74}$$

Equations (2.73) and (2.74), can now be introduced into equation (2.68),

$$\begin{aligned}
\mathrm{i}\hbar\frac{\partial a_{k'}(t)}{\partial t} &= \sum_{ki\lambda} a_k(t)\,\mathrm{e}^{\mathrm{i}\omega_{k'k}t}\,ec\vec{\mathcal{M}}^{\mathrm{M1}}_{k'k}\cdot\Bigg(\langle n_i-1|\mathrm{i}\sqrt{\frac{\hbar}{2\varepsilon_0\omega_i V}}c_i\vec{\mathbf{k}}_i\times\hat{\varepsilon}_{i\lambda}\,\mathrm{e}^{-\mathrm{i}\omega_i t}|n_i\rangle \\
&\qquad + \langle n_i+1|-\mathrm{i}\sqrt{\frac{\hbar}{2\varepsilon_0\omega_i V}}c_i^\dagger\vec{\mathbf{k}}_i\times\hat{\varepsilon}^*_{i\lambda}\,\mathrm{e}^{\mathrm{i}\omega_i t}|n_i\rangle\Bigg) \\
\mathrm{i}\hbar\frac{\partial a_{k'}(t)}{\partial t} &= \sum_{ki\lambda} a_k(t)\,\mathrm{e}^{\mathrm{i}\omega_{k'k}t}\,ec\vec{\mathcal{M}}^{\mathrm{M1}}_{k'k}\cdot\Big(\langle n_i-1|\vec{\mathbf{b}}_i(t)|n_i\rangle + \langle n_i+1|\vec{\mathbf{b}}^*_i(t)|n_i\rangle\Big)
\end{aligned} \tag{2.75}$$

where the coefficients $\mathrm{i}\sqrt{\frac{\hbar}{2\varepsilon_0\omega_i V}}$ are included in the matrix elements of the radiation field. This quantity is identified to be the magnetic field for the mode i, as defined by equations (2.18) and (2.56) and evaluated at $\vec{\mathbf{r}} = 0$, i.e. $\vec{\mathbf{b}}_i(t) = \mathrm{i}\sqrt{\frac{\hbar}{2\varepsilon_0\omega_i V}}c_i\vec{\mathbf{k}}_i\times\hat{\varepsilon}_{i\lambda}\,\mathrm{e}^{-\mathrm{i}\omega_i t}$.

The matrix elements of the radiation field in (2.75) can be approximated to the value of the applied magnetic field for that mode, $\vec{\mathbf{B}}_i(t)$. Since the radiation field needs to have a great intensity for the experiment, the number of photons before and after absorption (or emission), is about the same, i.e. $|n_i - 1\rangle \approx |n_i + 1\rangle \approx |n_i\rangle$, and the matrix elements are approximated to $\langle n_i|\vec{\mathbf{b}}_i(t) + \vec{\mathbf{b}}^*_i(t)|n_i\rangle$. Noting now that magnetic field in this matrix element is of the form (2.18) (with the A_i and A_i^* in their operator form), which means that $\vec{\mathbf{B}}_i(t) = \vec{\mathbf{b}}_i(t) + \vec{\mathbf{b}}^*_i(t)$ is a magnetic field in its operator form, and the matrix element becomes $\langle n_i|\vec{\mathbf{B}}_i(t)|n_i\rangle$. Changing the magnetic field to its classic form (equivalent to (2.37)

but with amplitude B_i and direction $\vec{\mathbf{k}_\mathbf{i}} \times \hat{\varepsilon}_{i\lambda}$), the matrix element just evaluates to the classical $\vec{\mathbf{B}}_i(t)$. With this approximation the quantization of the magnetic field is lost, allowing for a more practical description of the system dynamic, depending only on the applied magnetic field, given generically for each mode by $\vec{\mathbf{B}}_i(t) = \vec{\mathbf{b}}_i(t) + \text{c.c.}$ with $\vec{\mathbf{b}}_i(t) = \frac{B_i}{2} e^{-i\omega_i t} \hat{\mathbf{k}}_i \times \hat{\varepsilon}_{i\lambda}$, and the magnetic field intensity is related to the electric field intensity, $cB_i = E_i$. The magnetic field can then be written in a way that resembles (2.37) (more exactly, an equivalent to (2.37) but for the magnetic field).

$$i\hbar \frac{\partial a_{k'}(t)}{\partial t} = \sum_{ki\lambda} a_k(t) e^{i\omega_{k'k}t} \vec{\mathcal{M}}^{\text{M1}}_{k'k} \cdot \left(\frac{eE_i}{2} e^{-i\omega_i t} \hat{\mathbf{k}}_i \times \hat{\varepsilon}_{i\lambda} + \text{c.c.} \right) \tag{2.76}$$

Since we are focused on the polarization of the laser, we perform the calculations for one mode of radiation, and investigate the modes of the polarization. Noticing that only the polarization depends on λ, and realizing that the sum for all polarization modes is the polarization vector itself, $\sum_\lambda \hat{\varepsilon}_\lambda = \hat{\varepsilon}$, equation (2.76) reduces to

$$i\hbar \frac{\partial a_{k'}(t)}{\partial t} = \sum_{k} a_k(t) e^{i\omega_{k'k}t} \vec{\mathcal{M}}^{\text{M1}}_{k'k} \cdot \left(\frac{eE}{2} e^{-i\omega t} \hat{\mathbf{k}} \times \hat{\varepsilon} + \text{c.c.} \right). \tag{2.77}$$

A more familiar expression for the dot product of (2.77) is in the magnetic dipole moment form, $\vec{\mu}$. The quantum magnetic dipole is given by [42]

$$\vec{\mu} = -\frac{e}{2m} \left(g_L \vec{\mathbf{L}} + g_S \vec{\mathbf{S}} \right), \tag{2.78}$$

where the gyroscopic factors for the angular momentum $g_L = 1$, and spin $g_S \approx 2$ are considered. The (spin) gyroscopic factor for the muon is slightly higher than 2, and its actual value can only be deduced with QED analysis.

The dot product in (2.77), considering the matrix element (2.72), the magnetic dipole moment (2.78) and the magnetic field described earlier, thus becomes

$$M^{M1}_{k'k} = \vec{\mathcal{M}}^{\text{M1}}_{k'k} \cdot \left(\frac{eE}{2} e^{-i\omega t} \hat{\mathbf{k}} \times \hat{\varepsilon} + \text{c.c.} \right) = \langle \phi_{k'} | -\vec{\mu} \cdot \vec{\mathbf{B}}(t) | \phi_k \rangle \,. \tag{2.79}$$

Here it can be noticed that the operator in the matrix element of (2.79), is the energy of a magnetic dipole $\vec{\mu}$ in a magnetic field $\vec{\mathbf{B}}(t)$ [39]. Since this dot product results from the matrix element of the interaction Hamiltonian (2.62), equation (2.79) states that the interaction Hamiltonian can be simplified to the classically defined energy of a magnetic dipole moment.

Dividing (2.79) by $\hbar$, a quantity with dimensions of frequency is obtained,

$$\begin{aligned} \frac{M^{M1}_{k'k}}{\hbar} &= \frac{E}{2c\hbar} \langle \phi_{k'} | -\vec{\mu} | \phi_k \rangle \cdot \left(\hat{\mathbf{k}} \times \hat{\varepsilon} \right) e^{-i\omega t} + \frac{E^*}{2c\hbar} \langle \phi_{k'} | -\vec{\mu} | \phi_k \rangle \cdot \left(\hat{\mathbf{k}} \times \hat{\varepsilon}^* \right) e^{i\omega t} \\ &= \frac{\mathcal{V}_{k'k}}{2} e^{-i\omega t} + \frac{\mathcal{V}^*_{kk'}}{2} e^{i\omega t} \,. \end{aligned} \tag{2.80}$$

This quantity is directly related with the Rabi frequency for the M1 multipole [46],

$$\mathcal{V}_{k'k} = \frac{E}{c\hbar} \langle \phi_{k'} | -\vec{\mu} | \phi_k \rangle \cdot \left(\hat{\mathbf{k}} \times \hat{\varepsilon} \right). \tag{2.81}$$

Equation (2.77) can be written compactly with use of equation (2.80) as

$$\frac{\partial a_{k'}(t)}{\partial t} = \sum_k \frac{-\mathrm{i}}{2} a_k(t)\, \mathrm{e}^{\mathrm{i}\omega_{k'k}t}\left(\mathcal{V}_{k'k}\,\mathrm{e}^{-\mathrm{i}\omega t} + \mathcal{V}^*_{kk'}\,\mathrm{e}^{\mathrm{i}\omega t}\right). \tag{2.82}$$

With equation (2.82), the differential equations for the amplitudes of each level, are completed. In chapter 3 the equivalent differential equations for the population of each state are deduced.

2.7 Hyperfine Structure

The hyperfine structure emerges from the interaction of electric and magnetic multipoles of the nucleus with the orbiting particle.

Considering the total angular momentum $\vec{\mathbf{J}}$ for the orbiting particle, and a nuclear spin $\vec{\mathbf{I}}$, a third angular momentum $\vec{\mathbf{F}}$ for the nucleus-particle system can be obtained with standard coupling rules, $\vec{\mathbf{F}} = \vec{\mathbf{J}} + \vec{\mathbf{I}} \implies |J+I| \leq F \leq J+I$ and $m_F = m_J + m_I$. On the other hand, $\vec{\mathbf{J}}$ results from the coupling of the angular momentum $\vec{\mathbf{L}}$ and spin $\vec{\mathbf{S}}$ of the orbiting particle, which allows us to write the total angular momentum $\vec{\mathbf{F}}$ as the coupling of $\vec{\mathbf{L}}$, $\vec{\mathbf{S}}$ and $\vec{\mathbf{I}}$, i.e. $\vec{\mathbf{F}} = \vec{\mathbf{L}} + \vec{\mathbf{S}} + \vec{\mathbf{I}}$ and $m_F = m_L + m_S + m_I$.

Coupling the spin $\vec{\mathbf{S}}$ with the angular momentum $\vec{\mathbf{L}}$, which is implied in the Dirac equation in section 2.3, gives rise to the fine structure, a separation of the nl level in two other levels, $nl_{J=l-1/2}$ and $nl_{J=l+1/2}$ (except for $l = 0$ in which only $J = l + 1/2$ exists). In a similar manner, the coupling of the nuclear spin $\vec{\mathbf{I}}$ with $\vec{\mathbf{J}}$ also gives rise to a separation of the J levels, the hyperfine structure. For example, the ground state of μH is $1S_{J=1/2}$ and it's nuclear spin is $\vec{\mathbf{I}} = 1/2$, the possibilities for the total angular momentum $\vec{\mathbf{F}}$ are $|1/2 - 1/2| \leq F \leq 1/2 + 1/2 \implies F = 0, 1$. This is, the ground state separates into $1S^{F=0}_{1/2}$ and $1S^{F=1}_{1/2}$. Like any quantized angular momentum there is a corresponding azimuthal value m_F that ranges between $-F$ and F.

The nuclear spin also affects the magnetic dipole moment. Equation (2.78) gives the contribution of the orbiting particle to the magnetic dipole moment, to account for the nucleus, one must add a similar expression but in terms of $\vec{\mathbf{I}}$ and the nucleus mass M [41]. The gyroscopic factor for the nucleus in equation (2.83) is $g_N = -5.5856946893(16)$ for the proton and $g_N = 4.255250615(50)$ for ^{3}He [5].

$$\vec{\mu}_N = -\frac{e}{2M} g_N \vec{\mathbf{I}} \tag{2.83}$$

Combining now the magnetic moments of the nucleus (2.83) and the orbiting particle (2.78), the total magnetic moment of this system is

$$\vec{\mu} = -\frac{e}{2m}\left(g_L \vec{\mathbf{L}} + g_S \vec{\mathbf{S}} + \frac{m}{M} g_N \vec{\mathbf{I}}\right). \tag{2.84}$$

This magnetic moment is the one used in the calculations of the Rabi frequency (2.81).

3

Time Dynamics

In chapter 2, it was constructed the mathematical formalism regarding the behaviour of the wave-function of the muon plus H (or He) atomic system, whilst in interaction with an electromagnetic field. The differential equations for the coefficients of the wave-function were obtained in terms of the energy of each level, and in terms of the Rabi frequency. These equations however, do not directly give out information about the population of each state.

In the present chapter, the differential equations for the population of each state are derived. These differential equations are the Bloch equations, and are derived for the different experiments discussed in chapter 1:

- 2-levels and 4-levels Bloch equations for μH, with application in the CREMA-HyperMu and FAMU (diffusion) experiments and in the RIKEN (asymmetry) experiment;

- 4-levels Bloch equations for μ^3He^+, with application in the CREMA-μ^3He^+ (asymmetry) experiment.

3.1 General Bloch equations

Standard quantum mechanics mentions that for wave-function of the form (2.65), the probability of finding the system in the state ψ_k is given by $|a_k|^2$, provided that the wave-function is normalized. This probability is the population of the ψ_k state. More generically, the population matrix can be written as [46]

$$\rho_{ij} = a_i a_j^* \,, \tag{3.1}$$

where the diagonal terms, $i = j$, represent the probability of finding the system in the state i, i.e. is the population of state i, and the off-diagonal terms represent the coherence between states i and j. From this definition it is obvious that $\rho_{ij} = \rho_{ji}^*$ and that ρ_{ii} is real, and from the normalization of the wave-function, $\sum_i \rho_{ii} = 1$.

The derivative of equation (3.1) gives the set of differential equations for the populations.

$$\begin{aligned}\frac{\partial \rho_{ij}(t)}{\partial t} &= a_i(t)\frac{\partial a_j^*(t)}{\partial t} + a_j^*(t)\frac{\partial a_i(t)}{\partial t} \\ &= \sum_k \frac{\mathrm{i}}{2}\rho_{ik}\,\mathrm{e}^{-\mathrm{i}\,\omega_{jk}t}\left(\mathcal{V}_{jk}^*\,\mathrm{e}^{\mathrm{i}\,\omega t} + \mathcal{V}_{kj}\,\mathrm{e}^{-\mathrm{i}\,\omega t}\right) - \frac{\mathrm{i}}{2}\rho_{kj}\,\mathrm{e}^{\mathrm{i}\,\omega_{ik}t}\left(\mathcal{V}_{ik}\,\mathrm{e}^{-\mathrm{i}\,\omega t} + \mathcal{V}_{ki}^*\,\mathrm{e}^{\mathrm{i}\,\omega t}\right)\end{aligned} \tag{3.2}$$

Equation (3.2) was simplified with the help of (2.82).

For a n-levels system, there should be a total of n^2 differential equations, but noticing the symmetry $\rho_{ij} = \rho_{ji}^*$, only $n(n+1)/2$ equations are required, e.g. 3 for a 2-levels system and 10 for a 4-levels system.

In the following sections, the rotating wave approximation will be referenced several times. In short, this approximation states that the terms that oscillate much faster, have little effect to the time derivative of the populations when compared to the slow oscillating terms, and therefore they can be dropped from the equations. More detail on the rotating wave approximation can be found in appendix C.

3.2 μH Bloch Equations

As described in section 1.4, for μH, there are a total of four states, a singlet ground state $|F=0, m_F=0\rangle$, and a triplet excited state with $F=1$, $|F=1, m_F=-1\rangle$, $|F=1, m_F=0\rangle$ and $|F=1, m_F=1\rangle$. The energy of the ground state is $E^{F=0}$, and the energy of the degenerate excited state is $E^{F=1}$, which is necessarily greater than $E^{F=0}$. The relative energy is given by $\hbar\omega_r = E^{F=1} - E^{F=0} = \hbar\omega_{10}$. In the asymmetry experiment, there is a magnetic field of 0.06 T, to define the z direction. This magnetic field produces a splitting of the m_F sub-levels due to the Zeeman effect, and they will not all have the same energy. Each m_F sub-levels gains an extra energy of $\mu_B g_F B m_F$, where μ_B is the Bohr's magneton, B the magnetic field intensity, g_F is the gyroscopic Landé factor, which is calculated with

$$g_F = g_J \frac{F(F+1) + J(J+1) - I(I+1)}{2F(F+1)} + \frac{m}{M} g_N \frac{F(F+1) - J(J+1) + I(I+1)}{2F(F+1)},$$

which is $g_F = 1/2(g_J + m/M g_N)$ for the $1S_{\frac{1}{2}}^{F=1}$, and the g_J factor is the same as g_S since $L=0$. In the RIKEN experiment, the magnetic field is $B = 0.06$ T [28], and thus the shift in energy is ≈ 0.58 GHz, which is five orders of magnitude lower than the expected value for the transition frequency of 44.2 THz [47]. The Zeeman effect will therefore not be considered in the energy of the sub-levels, since the energy shift is negligible.

The CREMA-HyperMu and FAMU measurements are not (see section 1.6) sensitive to the sub-levels of the excited level. The system could therefore be seen as a 2-levels system, the degenerate $1\,\mathrm{S}_{\frac{1}{2}}{}^{\mathrm{F}=1}$ excited level, and the $1\,\mathrm{S}_{\frac{1}{2}}{}^{\mathrm{F}=0}$ ground state. This approach has the difficulty that the Rabi frequency is not well defined for transitions between degenerate levels. Alternatively, the 2-levels Bloch equations for μH could be obtained by reducing the 4-levels Bloch equations to the 2-levels case. The Rabi frequencies for the 4-levels

case are all well defined, and with those, the Rabi frequency for the 2-levels case can be obtained.

3.2.1 2-Levels Case

In the 2-levels case, the two possible states are $|F = 0\rangle$ and $|F = 1\rangle$, and their energy difference is still given by $\hbar\omega_{10} = \hbar\omega_r$. The difference in frequency between the transition energy and the laser energy is $\Delta = \omega_r - \omega$. The nomenclature for the indices in the populations and in the Rabi frequencies is ρ_{ij}=$\rho_{F'F}$ and $\mathcal{V}_{ij}$=$\mathcal{V}_{F'F}$, where F and F' are the total angular momenta, and can be 0 or 1 (for the ground state and excited state respectively). This system can be represented with the energy diagram of figure 3.1.

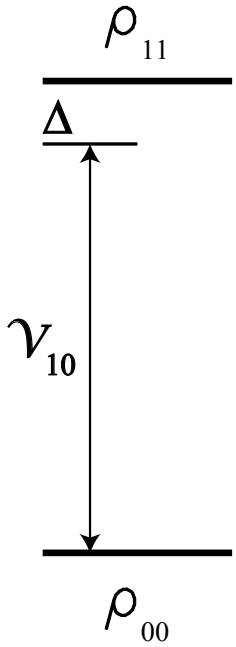

Figure 3.1: 2-levels system energy diagram for μH. ρ_{11} is the triplet excited state and ρ_{00} the singlet ground state. There are transitions due to the laser, with strength given by the Rabi frequency $\mathcal{V}_{10}$.

The populations are computed (in detail in appendix B.1) according to (3.2) and applying the rotating wave approximation, resulting in

$$\frac{\partial\rho_{00}(t)}{\partial t} \approx \frac{\mathrm{i}}{2}\rho_{01}\,\mathcal{V}_{10}\,\mathrm{e}^{\mathrm{i}\Delta t} + \text{c.c.} \tag{3.3}$$

and

$$\frac{\partial\rho_{01}(t)}{\partial t} \approx \frac{\mathrm{i}}{2}(\rho_{00} - \rho_{11})\,\mathcal{V}_{10}^{*}\,\mathrm{e}^{-\mathrm{i}\Delta t} \tag{3.4}$$

The excited state population can be easily computed by taking into account the normalization $\rho_{00} + \rho_{11} = 1$, or in the differential form $\frac{\partial\rho_{00}(t)}{\partial t} = -\frac{\partial\rho_{11}(t)}{\partial t}$, and the ρ_{10} can be found with the symmetry $\rho_{10} = \rho_{01}^{*}$.

In order to solve equations (3.3) and (3.4), the Rabi frequency $\mathcal{V}_{10}$ must be calculated for any atomic transition. This frequency was not defined in the mathematical formalism constructed so far, since one of the states of the matrix element is degenerate. To accordingly define this frequency, the 4-levels Bloch equations must be deduced and then compared with the 2-levels case.

3.2.2 4-Levels Case

As previously mentioned, in the 4-levels case there is the ground state level $|F = 0, m_F = 0\rangle$, and the three degenerate excited levels $|F = 1, m_F = -1, 0, 1\rangle$. The 4-levels system is represented with the energy diagram of figure 3.2.

The nomenclature for the indices in the populations and in the Rabi frequencies is ρ_{ij}=$\rho_{F'F}^{m'_F m_F}$ and $\mathcal{V}_{ij}$=$\mathcal{V}_{F'F}^{m'_F m_F}$, where the first subscript and superscript correspond to the same level $\left|F' m'_F\right\rangle$, and the second ones correspond to the same level $|F m_F\rangle$.

Since the excited state is degenerate, there are only three relevant populations to compute, ρ_{00}^{00}, $\rho_{01}^{0 m_F}$ and $\rho_{11}^{m'_F m_F}$, with both m_F and m'_F allowed to be any of the sub-states, i.e. $m_F = -1, 0, 1$ and $m'_F = -1, 0, 1$.

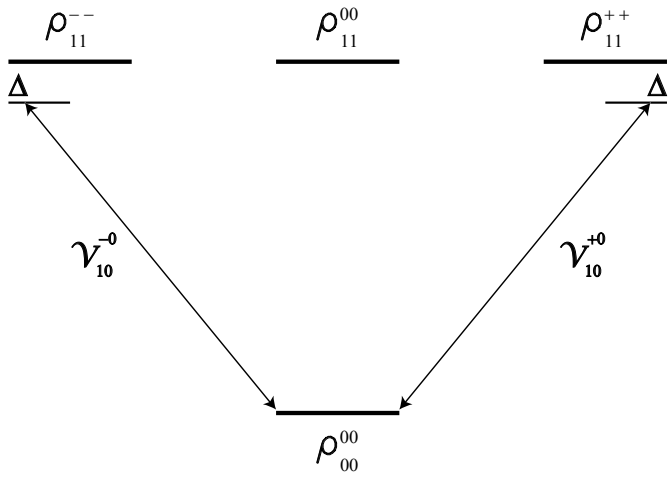

Figure 3.2: 4-levels system energy diagram for μH. ρ_{11}^{--}, ρ_{11}^{00} and ρ_{11}^{++} are the sub-levels of the triplet excited state and ρ_{00}^{00} is the singlet ground state. There are transitions due to the laser, with strength given by the Rabi frequencies $\mathcal{V}_{10}^{+0}$ and $\mathcal{V}_{10}^{-0}$. Note that transition between $m_F = 0$ states is forbidden due to the transverse wave property of the electromagnetic field as mentioned in section 2.2.3.

The populations are again computed according to (3.2) and applying the rotating wave approximation (derivation in detail in appendix B.2), and result in

$$\frac{\partial \rho_{00}^{00}(t)}{\partial t} \approx \sum_{m_F} \frac{\mathrm{i}}{2} \rho_{01}^{0 m_F} \, \mathrm{e}^{\mathrm{i}\Delta t} \, \mathcal{V}_{10}^{m_F 0} + \text{c.c.}\,, \tag{3.5}$$

$$\frac{\partial \rho_{11}^{m'_F m_F}(t)}{\partial t} \approx \frac{\mathrm{i}}{2} \rho_{10}^{m'_F 0} \, \mathrm{e}^{-\mathrm{i}\Delta t} \, \mathcal{V}_{10}^{m_F 0 *} - \frac{\mathrm{i}}{2} \rho_{01}^{0 m_F} \, \mathrm{e}^{\mathrm{i}\Delta t} \, \mathcal{V}_{10}^{m'_F 0} \tag{3.6}$$

and

$$\frac{\partial \rho_{01}^{0m_F}(t)}{\partial t} \approx \frac{\mathrm{i}}{2}\rho_{00}^{00}\,\mathrm{e}^{-\mathrm{i}\Delta t}\,\mathcal{V}_{10}^{m_F 0*} - \sum_{M=-1}^{1}\frac{\mathrm{i}}{2}\rho_{11}^{Mm_F}\,\mathrm{e}^{-\mathrm{i}\Delta t}\,\mathcal{V}_{10}^{M0*}\,, \tag{3.7}$$

Equations (3.5), (3.6) and (3.7) for all possibles m_F and m_F' constitute the set of differential equations necessary to study the populations' dynamics.

3.2.3 Polarization in μH Bloch Equations

By comparing the 2-levels Bloch equations with the 4-levels case, a definition for the Rabi frequency of the degenerate excited state can be obtained.

Before comparing the two cases, some relations between populations must be provided. First, the ground state is the same in both cases, i.e. $\rho_{00} = \rho_{00}^{00}$. This statement is obvious since the level is a single state. Second the population of the excited state in the 2-levels case is the sum of the population of each sub-state,

$$\rho_{11} = \rho_{11}^{--} + \rho_{11}^{00} + \rho_{11}^{++}\,. \tag{3.8}$$

Here we shorten the notation by dropping the number one in the superscripts. With these informations, the 4-levels equations can be reduced to the 2-levels equations (see appendix B.3), with the condition that Rabi frequencies of these two cases are related by

$$|\mathcal{V}_{10}|^2 = \sum_{m_F}\left|\mathcal{V}_{10}^{m_F 0}\right|^2\,. \tag{3.9}$$

If the experiment do not detect the degenerate individual populations, the 2-level system along with equation 3.9 is sufficient to describe the dynamics. Moreover, the Rabi frequencies for the non-degenerate case (deduced in detail in appendix D.1) are given by

$$\begin{aligned}\mathcal{V}_{10}^{\pm 0} &= \mp\sqrt{8\pi\alpha\hbar\mathcal{I}}\left(\frac{g_S}{4cm} - \frac{g_N}{4cM}\right)\frac{\mathrm{i}\,\mathrm{e}^{\mp\mathrm{i}\chi}}{\sqrt{2}}\,\frac{\eta\mp 1}{\sqrt{\eta^2+1}}\,, \qquad \mathcal{V}_{10}^{00} = 0 \\ &\approx \mp 51.23\sqrt{\mathcal{I}}\,\frac{\mathrm{i}\,\mathrm{e}^{\mp\mathrm{i}\chi}}{\sqrt{2}}\,\frac{\eta\mp 1}{\sqrt{\eta^2+1}}\,,\end{aligned} \tag{3.10}$$

here, $\mathcal{I}$ is the laser intensity and the factor $51.23\sqrt{\mathcal{I}}\,\mathrm{rad\,s^{-1}}$ is the same value obtained in [47]. The Rabi frequency for the degenerate case is then

$$|\mathcal{V}_{10}| = \sqrt{8\pi\alpha\hbar\mathcal{I}}\left(\frac{g_S}{4cm} - \frac{g_N}{4cM}\right) \approx 51.23\sqrt{\mathcal{I}}\,, \tag{3.11}$$

and the $|\mathcal{V}_{10}|$ does not have any dependence on the polarization parameters. The Rabi frequency itself, $\mathcal{V}_{10}$, may have a dependence on the polarization vector $\hat{\varepsilon}$, but only on its phase, having the form

$$\mathcal{V}_{10} = |\mathcal{V}_{10}|\mathrm{e}^{\mathrm{i}\theta_\varepsilon}\,.$$

Considering now this form for the Rabi frequency, and inputting it into the 2-levels Bloch equations (3.3) and (3.4) gives

$$\frac{\partial \rho_{00}(t)}{\partial t} = \frac{\mathrm{i}}{2}\rho_{01}|\mathcal{V}_{10}|\mathrm{e}^{\mathrm{i}\theta_\varepsilon}\,\mathrm{e}^{\mathrm{i}\Delta t} + \text{c.c.}\,, \tag{3.12}$$

and

$$\frac{\partial \rho_{01}(t)}{\partial t} = \frac{\mathrm{i}}{2}(\rho_{00} - \rho_{11})|\mathcal{V}_{10}|\mathrm{e}^{-\mathrm{i}\theta_\varepsilon}\,\mathrm{e}^{-\mathrm{i}\Delta t}\ . \tag{3.13}$$

Performing a change of variable $\widetilde{\rho}_{01} = \rho_{01}\,\mathrm{e}^{\mathrm{i}\theta_\varepsilon}\,\mathrm{e}^{\mathrm{i}\Delta t}$, and noticing that $\widetilde{\rho}^{*}_{01} = \widetilde{\rho}_{10}$ still holds, then equations (3.12), and (3.13) become

$$\frac{\partial \rho_{00}(t)}{\partial t} = \frac{\mathrm{i}}{2}\widetilde{\rho}_{01}|\mathcal{V}_{10}| + \text{c.c.}\,, \tag{3.14}$$

and

$$\frac{\partial \widetilde{\rho}_{01}(t)}{\partial t} = \frac{\mathrm{i}}{2}(\rho_{00} - \rho_{11})|\mathcal{V}_{10}| + \mathrm{i}\Delta\widetilde{\rho}_{01}\,. \tag{3.15}$$

Analysing now these differential equations, it becomes obvious that they do not depend on the polarization, i.e. they are the same regardless of the polarization. As such, the population of the ground state ρ_{00}, and consequently of the excited state ρ_{11}, does not depend on the polarization either.

For simplicity, a similar type of substitution, $\widetilde{\rho}^{0M}_{01} = \rho^{0M}_{01}\,\mathrm{e}^{\mathrm{i}\Delta t}$, can be performed for the 4-levels equations (3.5), (3.7) and (3.6).

$$\frac{\partial \rho^{00}_{00}(t)}{\partial t} = \sum_{m_F} \frac{\mathrm{i}}{2}\widetilde{\rho}^{0m_F}_{01}\,\mathcal{V}^{m_F 0}_{10} + \text{c.c.}\,, \tag{3.16}$$

$$\frac{\partial \rho^{m'_F m_F}_{11}(t)}{\partial t} = \frac{\mathrm{i}}{2}\widetilde{\rho}^{m'_F 0}_{10}\mathcal{V}^{m_F 0*}_{10} - \frac{\mathrm{i}}{2}\widetilde{\rho}^{0m_F}_{01}\mathcal{V}^{m'_F 0}_{10} \tag{3.17}$$

and

$$\frac{\partial \widetilde{\rho}^{0m_F}_{01}(t)}{\partial t} = \frac{\mathrm{i}}{2}\rho^{00}_{00}\mathcal{V}^{m_F 0*}_{10} - \sum_{M=-1}^{1}\frac{\mathrm{i}}{2}\rho^{Mm_F}_{11}\mathcal{V}^{M0*}_{10} + \mathrm{i}\Delta\widetilde{\rho}^{0m_F}_{01}\,. \tag{3.18}$$

By Inspection of equation (3.10), when the polarization degree is $\eta = \pm 1$, the Rabi frequencies become

$$\eta = \pm 1 \implies \mathcal{V}^{\pm 0}_{10} = 0 \text{ and } \mathcal{V}^{\mp 0}_{10} = \pm 51.23\sqrt{\mathcal{I}}\,\mathrm{i}\,\mathrm{e}^{\pm \mathrm{i}\chi}\,, \tag{3.19}$$

then, the population $\rho^{\pm\pm}_{11}$ will have a null derivative, which means that it does not change from its initial value (which is null). In other words, right or left circular polarizations induce transitions to the $m_F = \mp 1$ sub-state respectively.

3.3 $\mu^3\mathrm{He}^+$ Bloch Equations

The CREMA-$\mu^3\mathrm{He}^+$ experiment uses the asymmetry method. This method is sensitive to the sub-levels of the ground state, it has the goal of measuring the difference between electrons emitted in two opposite directions, produced after muon decay, which is directly dependent on the populations of the m_F sub-levels (section 1.7 and 1.8). As such, there is no point to retrieve the 2-levels equations for $\mu^3\mathrm{He}^+$, since there is no planned experiment with $\mu^3\mathrm{He}^+$ that is not sensitive to the sub-levels.

Similarly to the μH system, the $\mu^3\mathrm{He}^+$ also has a total of four states, but with the difference that the singlet state $|F=0, m_F=0\rangle$ is the excited state and the triplet state is the ground state. The relative energy between the states is $\hbar\omega_r = E^{F=0} - E^{F=1} = \hbar\omega_{01}$. Once more the Zeeman effect is negligible, the g_F is calculated in the same way, and the energy shift will be ≈ 0.91 GHz, which is six orders of magnitude lower than the transition frequency of 322 THz [29]. This new system can be represented with the energy diagram of figure 3.3.

The nomenclature remains the same, $\rho_{ij}=\rho_{F'F}^{m'_F m_F}$ and $\mathcal{V}_{ij}=\mathcal{V}_{F'F}^{m'_F m_F}$, where the first subscript and superscript correspond to the same level $\left|F'm'_F\right\rangle$, and the second ones correspond to the same level $|Fm_F\rangle$. The necessary populations to compute are also ρ_{00}^{00}, $\rho_{01}^{0m_F}$ and $\rho_{11}^{m'_F m_F}$, with both m_F and m'_F being able to be any of the sub-states, i.e. -1, 0 or 1. The difference in frequency between the transition energy and the laser energy is also $\Delta = \omega_r - \omega$.

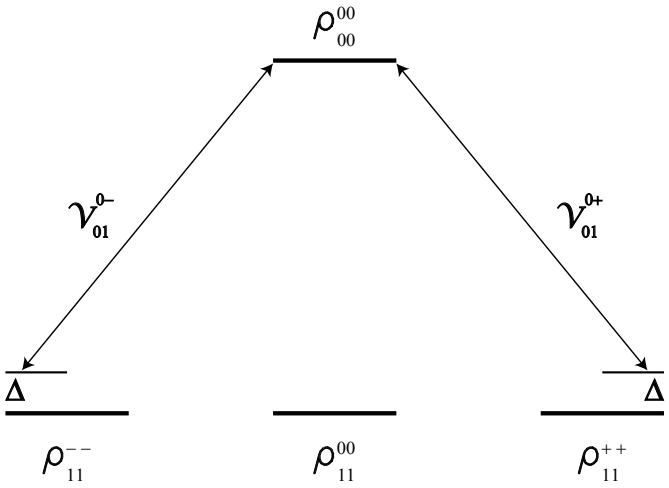

Figure 3.3: 4-levels system energy diagram for $\mu^3\mathrm{He}^+$. ρ_{11}^{--}, ρ_{11}^{00} and ρ_{11}^{++} are the sub-levels of the triplet ground state and ρ_{00}^{00} is the singlet excited state. There are transitions due to the laser, with strength given by the Rabi frequencies $\mathcal{V}_{01}^{0+}$ and $\mathcal{V}_{01}^{0-}$. Note that transition between the $m_F = 0$ states is forbidden due to the transverse wave property of the electromagnetic field as mentioned in section 2.2.3.

The population equations for $\mu^3\mathrm{He}^+$ are derived in detail in appendix B.4, and result in

$$\frac{\partial \rho_{11}^{m'_F m_F}(t)}{\partial t} \approx \frac{\mathrm{i}}{2}\rho_{10}^{m'_F 0}\,\mathrm{e}^{\mathrm{i}\Delta t}\,\mathcal{V}_{01}^{0m_F} - \frac{\mathrm{i}}{2}\rho_{01}^{0m_F}\,\mathrm{e}^{-\mathrm{i}\Delta t}\,\mathcal{V}_{01}^{0m'_F\,*}\,, \tag{3.20}$$

$$\frac{\partial \rho_{00}^{00}(t)}{\partial t} \approx \sum_{m_F} \frac{\mathrm{i}}{2}\rho_{01}^{0m_F}\,\mathrm{e}^{-\mathrm{i}\Delta t}\,\mathcal{V}_{01}^{0m_F\,*} + \text{c.c.}\,, \tag{3.21}$$

and

$$\frac{\partial \rho_{01}^{0m_F}(t)}{\partial t} \approx \frac{\mathrm{i}}{2}\rho_{00}^{00}\,\mathrm{e}^{\mathrm{i}\Delta t}\,\mathcal{V}_{01}^{0m_F} - \sum_{M=-1}^{1} \frac{\mathrm{i}}{2}\rho_{11}^{Mm_F}\,\mathrm{e}^{\mathrm{i}\Delta t}\,\mathcal{V}_{01}^{0M}\,, \tag{3.22}$$

The $\widetilde{\rho}_{01}^{0M} = \rho_{01}^{0M}\,\mathrm{e}^{-\mathrm{i}\,\Delta t}$ substitution can be applied to equations (3.20), (3.21) and (3.22) to give

$$\frac{\partial \rho_{11}^{m_F' m_F}(t)}{\partial t} = \frac{\mathrm{i}}{2}\widetilde{\rho}_{10}^{m_F' 0}\,\mathcal{V}_{01}^{0m_F} - \frac{\mathrm{i}}{2}\widetilde{\rho}_{01}^{0m_F}\mathcal{V}_{01}^{0m_F'\,*}\,, \tag{3.23}$$

$$\frac{\partial \rho_{00}^{00}(t)}{\partial t} = \sum_{m_F}\frac{\mathrm{i}}{2}\widetilde{\rho}_{01}^{0m_F}\mathcal{V}_{01}^{0m_F\,*} + \text{c.c.} \tag{3.24}$$

and

$$\frac{\partial \widetilde{\rho}_{01}^{0m_F}(t)}{\partial t} = \frac{\mathrm{i}}{2}\rho_{00}^{00}\,\mathcal{V}_{01}^{0m_F} - \sum_{M=-1}^{1}\frac{\mathrm{i}}{2}\rho_{11}^{Mm_F}\,\mathcal{V}_{01}^{0M} - \mathrm{i}\,\Delta\widetilde{\rho}_{01}^{0m_F}\,, \tag{3.25}$$

respectively.

The Rabi frequency for $\mu^3\mathrm{He}^+$ is derived in detail in appendix D.2 according to the definition (2.81) and the magnetic dipole moment (2.84), evaluating to

$$\mathcal{V}_{01}^{0\pm} = \mp\sqrt{8\pi\alpha\hbar\mathcal{I}}\left(\frac{g_S}{4mc} - \frac{g_N}{4Mc}\right)\frac{\mathrm{i}\,\mathrm{e}^{\pm\mathrm{i}\chi}}{\sqrt{2}}\,\frac{\eta\pm 1}{\sqrt{\eta^2+1}}\,, \qquad \mathcal{V}_{01}^{00} = 0 \tag{3.26}$$

$$\mathcal{V}_{01}^{0\pm} \approx \mp 35.87\sqrt{\mathcal{I}}\,\frac{\mathrm{i}\,\mathrm{e}^{\pm\mathrm{i}\chi}}{\sqrt{2}}\,\frac{\eta\pm 1}{\sqrt{\eta^2+1}}\,.$$

By Inspection of equation (3.26), when the polarization degree is $\eta = \pm 1$, the Rabi frequencies become

$$\eta = \pm 1 \implies \mathcal{V}_{01}^{0\mp} = 0 \text{ and } \mathcal{V}_{10}^{\pm 0} = \mp 35.87\sqrt{\mathcal{I}}\,\mathrm{e}^{\pm\mathrm{i}\chi}\,, \tag{3.27}$$

then, the population $\rho_{11}^{\mp\mp}$ will have a null derivative, which means that it does not change from its initial value. In other words, right or left circular polarizations induce transitions from the $m_F = \pm 1$ sub-state, respectively, to the $F = 0$ excited state.

The Rabi frequency absolute value is the frequency at which the populations will oscillate [46], since the μH system has a higher Rabi frequency ($|\mathcal{V}_{10}| = 51.23\sqrt{\mathcal{I}}\ \mathrm{rad\,s^{-1}}$) than the $\mu^3\mathrm{He}^+$ system ($|\mathcal{V}_{01}| = 35.87\sqrt{\mathcal{I}}\ \mathrm{rad\,s^{-1}}$), then the population will oscillate faster for μH (provided the laser has the same intensity).

The $\mu^3\mathrm{He}^+$ equations are similar to those of μH, with two differences: first, all the Rabi frequencies are conjugated (in comparison to those of μH equations), second the sign of Δ changes in the systems, however it will be seen in chapter 5 that the solutions are symmetric in Δ for both systems. Both sets of equations can be written in the simplified form [48]

$$\frac{\partial \hat{\rho}}{\partial t} = \frac{\mathrm{i}}{\hbar}[\hat{\rho}, H_{M1}] \tag{3.28}$$

where H_{M1} is the interaction Hamiltonian, which in this context corresponds to the energy of the magnetic dipole of the atomic system, in the magnetic field created by the laser, i.e. the operator in equation (2.79). The $\hat{\rho}$ is density matrix given by

$$\hat{\rho} = \begin{pmatrix} \rho_{00}^{00} & \widetilde{\rho}_{01}^{0-} & \widetilde{\rho}_{01}^{00} & \widetilde{\rho}_{01}^{0+} \\ \widetilde{\rho}_{10}^{-0} & \rho_{11}^{--} & \rho_{11}^{-0} & \rho_{11}^{-+} \\ \widetilde{\rho}_{10}^{00} & \rho_{11}^{0-} & \rho_{11}^{00} & \rho_{11}^{0+} \\ \widetilde{\rho}_{10}^{+0} & \rho_{11}^{+-} & \rho_{11}^{+0} & \rho_{11}^{++} \end{pmatrix}. \tag{3.29}$$

The equations for μH and $\mu^3\mathrm{He}^+$ derived so far, can be written in the form of (3.28), but with the Rabi frequencies instead of the Hamiltonian (since we already know their relation).

$$\frac{\partial\hat{\rho}}{\partial t} = \mathrm{i}[\hat{\rho}, \hat{\mathcal{V}}] \tag{3.30}$$

The matrix of Rabi frequencies in equation (3.30) is where there is the difference in the two atomic systems

$$\mu\mathrm{H} \Longrightarrow \quad \hat{\mathcal{V}} = \frac{1}{2}\begin{pmatrix} 0 & \mathcal{V}_{10}^{-0*} & \mathcal{V}_{10}^{00*} & \mathcal{V}_{10}^{+0*} \\ \mathcal{V}_{10}^{-0} & 2\Delta & 0 & 0 \\ \mathcal{V}_{10}^{00} & 0 & 2\Delta & 0 \\ \mathcal{V}_{10}^{+0} & 0 & 0 & 2\Delta \end{pmatrix} \tag{3.31}$$

$$\mu^3\mathrm{He}^+ \Longrightarrow \quad \hat{\mathcal{V}} = \frac{1}{2}\begin{pmatrix} 0 & \mathcal{V}_{01}^{0-} & \mathcal{V}_{01}^{00} & \mathcal{V}_{01}^{0+} \\ \mathcal{V}_{01}^{0-*} & -2\Delta & 0 & 0 \\ \rho_{01}^{00*} & 0 & -2\Delta & 0 \\ \rho_{01}^{0+*} & 0 & 0 & -2\Delta \end{pmatrix} \tag{3.32}$$

3.4 Decays and Laser Bandwidth

The Bloch equations deduced in sections 3.1 and 3.3 describe the interaction of the laser with the atomic system, however it assumes that the populations do not have any source of decays, such as spontaneous decay or inelastic collisional decays of atoms with the surrounding gas. Both these phenomena have the effect of lowering the populations by a certain rate. Furthermore, elastic collisions and the laser bandwidth do not affect the populations, but gives a decay source to the coherence populations. The extension of the Bloch equations with decay sources is given by the Lindblad equation [48, 49].

3.4.1 Bloch Equations with Decay Sources

The Lindblad master equation can be separated in two parts, the first being the atom-laser interaction deduced so far, and generically represented by equation (3.28). The other is the dissipative part resulting from the interaction with the environment [49], e.g. the collisional decays. The dissipative part of the Lindblad master equation is deduced formally in [48, 49]. Here a more practical approach will be presented, similar to [50].

Considering a wave-function $|\Psi\rangle$ of the type (2.65), with a coefficient a_k for each state $\left|\psi_k\right\rangle$. The rate at which the state $\left|\psi_i\right\rangle$ decreases to the state $\left|\psi_j\right\rangle$ is Γ_{ij}, and the rate equation for the coefficient a_i is changed by

$$\frac{\partial a_i(t)}{\partial t} \longrightarrow \frac{\partial a_i(t)}{\partial t} + \sum_k \frac{\Gamma_{ik}}{2} a_i \,, \tag{3.33}$$

which implies that

$$\frac{\partial \rho_{ij}(t)}{\partial t} \longrightarrow \frac{\partial \rho_{ij}(t)}{\partial t} + \sum_k \frac{\Gamma_{ik} + \Gamma_{jk}}{2} \rho_{ij} \,. \tag{3.34}$$

This means that a rate equation $\frac{\partial \rho_{ij}}{\partial t} = [\text{LASER}]$ changes to

$$\frac{\partial \rho_{ij}(t)}{\partial t} = [\text{LASER}] - \sum_k \frac{\Gamma_{ik} + \Gamma_{jk}}{2} \rho_{ij} \,, \tag{3.35}$$

where the term [LASER] represents the atom-laser interaction part of the equation, i.e. the Bloch equation. The states population ρ_{ii} have a nice interpretation,

$$\frac{\partial \rho_{ii}(t)}{\partial t} = [\text{LASER}] - \sum_k \Gamma_{ik} \rho_{ii} \,, \tag{3.36}$$

the state $|\psi_i\rangle$ is losing population at a rate of Γ_{ik} to the state $|\psi_k\rangle$. This interpretation also allows us to identify that the equation (3.36) is not complete, if all the populations are decressing their value, then the total would not stay constant at 1. This means that in the ρ_{ii} populations, an extra term must be added, so that $\sum_i \frac{\partial \rho_{ii}}{\partial t} = 0$,

$$\frac{\partial \rho_{ii}(t)}{\partial t} = [\text{LASER}] + \sum_k -\Gamma_{ik} \rho_{ii} + \Gamma_{ki} \rho_{kk} \,, \tag{3.37}$$

that extra term is corresponds to the value that the population ρ_{ii} is receiving from ρ_{kk}. It is important to notice that the Γ_{ik} can include not only the decays due to collisions, as well as any other type of decay, and even elastic decays which will only affect the coherent populations.

3.4.2 Laser Bandwidth

The laser bandwidth can be included directly in the Bloch equations just by considering the laser not monochromatic, this is, it has several modes with different intensities, according to the laser profile. This type of approach, although accurate, is quite complex to solve. In [51] the laser bandwidth, Γ_l, is included by identifying the coherence populations correspondent to the states connected by the laser, and making them decay with a rate of $\frac{\Gamma_l}{2}$. E.g., if there are three states $|1\rangle$, $|2\rangle$ and $|3\rangle$, and the laser is inducing transitions between the states $|1\rangle$ and $|3\rangle$, then the coherent population ρ_{13} would be $\frac{\partial \rho_{13}}{\partial t} = [\text{Laser}] - \frac{\Gamma_l}{2} \rho_{13}$, while the other coherent populations (ρ_{12} and ρ_{23}) would stay the same.

3.5 Decays in μH System

In the μH system there are three types of decays due to collisions with the surrounding H_2 gas. These decays, each with a specific rate, are due to the inelastic collisions (Γ_{in}), and the elastic collisions of the triplet excited state ($\Gamma_{\text{el}}^{F=1}$) and of the ground state ($\Gamma_{\text{el}}^{F=0}$).

$$\Gamma_{\text{in}}: \qquad \mu\text{H}^{\text{F=1}} + \text{H}_2 \Longrightarrow \mu\text{H}^{\text{F=0}} + \text{H}_2{}^* \tag{3.38}$$

$$\Gamma_{\text{el}}^{F=1}: \qquad \mu\text{H}^{\text{F=1}} + \text{H}_2 \Longrightarrow \mu\text{H}^{\text{F=1}} + \text{H}_2{}^* \tag{3.39}$$

$$\Gamma_{\text{el}}^{F=0}: \qquad \mu\text{H}^{\text{F=0}} + \text{H}_2 \Longrightarrow \mu\text{H}^{\text{F=0}} + \text{H}_2{}^* \tag{3.40}$$

In these equations, the $*$ represents possible rotational-vibrational excitations after collision.

There is also the laser bandwidth of Γ_l that must be accounted for in the coherent populations. These rates are included differently in the 2-levels case and in the 4-levels case.

3.5.1 Decays in 2-levels Case

The 2-levels system with decays can be represented with the diagram of figure 3.4, where the elastic and inelastic decays were added in relation to the diagram of figure 3.1. With

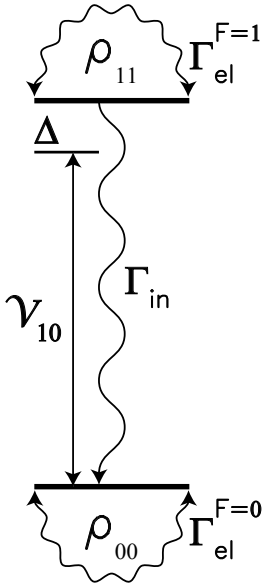

Figure 3.4: 2-levels system energy diagram for μH. ρ_{11} is the triplet excited state and ρ_{00} the singlet ground state. There are transitions due to the laser, with strength given by the Rabi frequency $\mathcal{V}_{10}$, and transitions due to collisions with rate Γ_{in}. There are also elastic collisions of the excited state $\Gamma_{\text{el}}^{F=1}$, and of the ground state $\Gamma_{\text{el}}^{F=0}$.

the equations of sections 3.4.1 and 3.4.2, equations (3.14) and (3.15), are altered to

$$\frac{\partial\rho_{00}(t)}{\partial t} = \frac{\text{i}}{2}\widetilde{\rho}_{01}|\mathcal{V}_{10}| + \text{c.c.} + \Gamma_{\text{in}}\rho_{11}\,, \tag{3.41}$$

$$\frac{\partial\widetilde{\rho}_{01}(t)}{\partial t} = \frac{\text{i}}{2}(\rho_{00}-\rho_{11})|\mathcal{V}_{10}| + \text{i}\,\Delta\widetilde{\rho}_{01} - \frac{1}{2}\Big(\Gamma_{\text{in}} + \Gamma_{\text{el}}^{F=1} + \Gamma_{\text{el}}^{F=0} + \Gamma_l\Big)\widetilde{\rho}_{01}\,, \tag{3.42}$$

and with $\frac{\partial\rho_{11}}{\partial t} = -\frac{\partial\rho_{00}}{\partial t}$,

$$\frac{\partial\rho_{11}(t)}{\partial t} = -\frac{\text{i}}{2}\widetilde{\rho}_{01}|\mathcal{V}_{10}| + \text{c.c.} - \Gamma_{\text{in}}\rho_{11}\,. \tag{3.43}$$

3.5.2 Decays in 4-levels Case

The 4-levels system with decays can be represented with the energy diagram of figure 3.2, where the elastic and inelastic decays were added in relation to the diagram of figure 3.5.

Comparing the decays between the 2-levels case and the 4-levels case, it is evident that each state, in total, must decay by the same rate. For example, the ρ_{11} state in the 2-levels case decays with a rate of Γ_{in} to ρ_{00} and with a rate of $\Gamma_{\text{el}}^{F=1}$ to itself. This means that, in total, the excited state is decaying with a rate of $\Gamma_{\text{in}} + \Gamma_{\text{el}}^{F=1}$, and thus, each of the ρ_{11}^{mm} must decay the same total, Γ_{in} to ρ_{00}^{00} and $\Gamma_{\text{el}}^{F=1}$ to the excited states ρ_{11}^{--}, ρ_{11}^{00} and ρ_{11}^{++}. The elastic rate of the $F=1$ state is calculated with the cross section of the collision (3.39). This cross section is obtained by summing over the cross sections of all sub-levels of the triplet state [52]. The rate at which a state $\left|\psi_1^m\right\rangle$ decays to a $\left|\psi_1^{m'}\right\rangle$ state is then proportional to $\Gamma_{\text{el}}^{F=1}$ by a factor given by the statistical weight $W_{mm'}$, such that the weights for all the m' sum to 1. These weights are calculated in appendix E and are presented in table E.2.

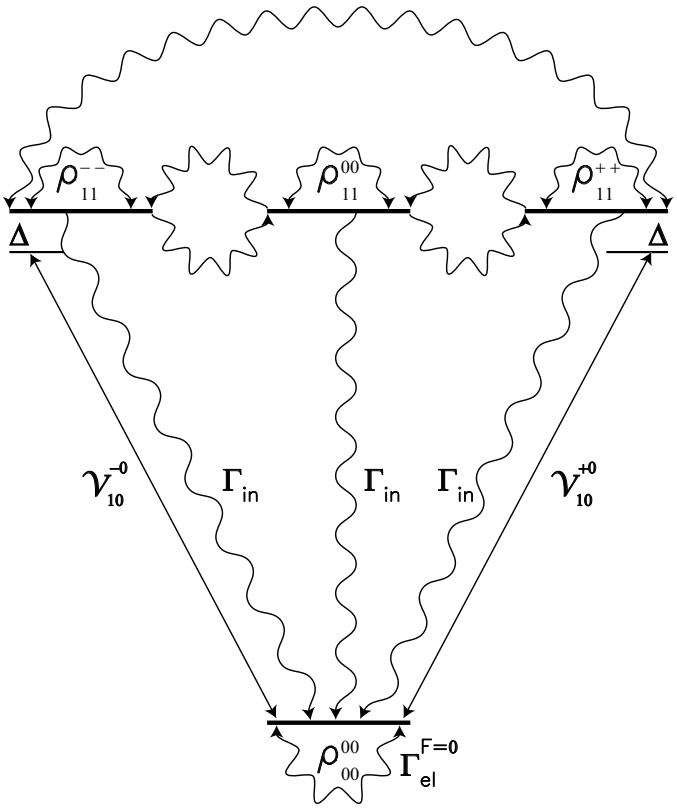

Figure 3.5: 4-levels system energy diagram for μH. ρ_{11}^{--}, ρ_{11}^{00} and ρ_{11}^{++} are the sub-levels of the triplet excited state and ρ_{00}^{00} is the singlet ground state. There are transitions due to the laser, with strength given by the Rabi frequencies $\mathcal{V}_{10}^{+0}$ and $\mathcal{V}_{10}^{-0}$, and transitions due to collisions with rate Γ_{in}. There are also elastic collisions of the excited state with rate $\Gamma_{\text{el}}^{F=1} W_{mm'}$, and of the ground state with rate $\Gamma_{\text{el}}^{F=0}$

The equations (3.16), (3.17) and (3.18) thus become

$$\frac{\partial \rho_{00}^{00}(t)}{\partial t} = \sum_{m_F} \frac{\mathrm{i}}{2} \mathcal{V}_{10}^{m_F 0} \widetilde{\rho}_{01}^{0 m_F} + \text{c.c.} + \Gamma_{\text{in}} \rho_{11}^{m_F m_F} , \tag{3.44}$$

$$\frac{\partial \rho_{11}^{m_F' m_F}(t)}{\partial t} = \frac{\mathrm{i}}{2} \widetilde{\rho}_{10}^{m_F' 0} \mathcal{V}_{10}^{m_F 0 *} - \frac{\mathrm{i}}{2} \widetilde{\rho}_{01}^{0 m_F} \mathcal{V}_{10}^{m_F' 0} - \left(\Gamma_{\text{in}} + \Gamma_{\text{el}}^{F=1}\right) \rho_{11}^{m_F' m_F} + \delta_{m_F' m_F} \sum_{M=-1}^{1} W_{M m_F} \Gamma_{\text{el}}^{F=1} \rho_{11}^{MM} \tag{3.45}$$

and

$$\frac{\partial \widetilde{\rho}_{01}^{0 m_F}(t)}{\partial t} = \frac{\mathrm{i}}{2} \rho_{00}^{00} \mathcal{V}_{10}^{m_F 0 *} - \sum_{M=-1}^{1} \frac{\mathrm{i}}{2} \rho_{11}^{M m_F} \mathcal{V}_{10}^{M 0 *} + \mathrm{i} \Delta \widetilde{\rho}_{01}^{0 m_F} - \frac{1}{2} \left(\Gamma_{\text{in}} + \Gamma_{\text{el}}^{F=1} + \Gamma_{\text{el}}^{F=0} + \Gamma_l\right) \widetilde{\rho}_{01}^{0 m_F} . \tag{3.46}$$

3.6 Decays in μ^3He$^+$ System

In the μ^3He$^+$ there are also three types of decays due to collisions with the surrounding ^{3}He gas. They are the inelastic collision with rate Γ_{in}, the elastic collision of the excited state with rate $\Gamma_{\text{el}}^{F=0}$ and the elastic collision of the ground state with rate $\Gamma_{\text{el}}^{F=1}$.

$$\Gamma_{\text{in}} : \qquad \mu^3\text{He}^{+\text{F=0}} + {}^3\text{He} \Longrightarrow \mu^3\text{He}^{+\text{F=1}} + {}^3\text{He} \tag{3.47}$$

$$\Gamma_{\text{el}}^{F=0} : \qquad \mu^3\text{He}^{+\text{F=0}} + {}^3\text{He} \Longrightarrow \mu^3\text{He}^{+\text{F=0}} + {}^3\text{He} \tag{3.48}$$

$$\Gamma_{\text{el}}^{F=1} : \qquad \mu^3\text{He}^{+\text{F=1}} + {}^3\text{He} \Longrightarrow \mu^3\text{He}^{+\text{F=1}} + {}^3\text{He} \tag{3.49}$$

There is also the possibility of molecular formation, μ^3He≡He, but that is not considered, as explained in section 1.8.

The laser bandwidth, Γ_l, is to be accounted for in the coherent populations.

For μ^3He$^+$, only the 4-levels case matters, and it can be represented in the energy diagram of figure 3.6, where the decays were added in relation to the diagram 3.3. Just as in the μH case, the elastic decay of the triplet state is divided for all the sub-levels according to a weight calculated in appendix E, and presented in table E.4. i.e. the sub-level $\left|\psi_1^m\right\rangle$ is decaying with a rate of $W_{mm'}\Gamma_{\text{el}}^{F=1}$ to the sub-level $\left|\psi_1^{m'}\right\rangle$. Furthermore, the excited state F= 0, decays equally to each of the sub-levels of the ground state (see appendix E).

The Bloch equations (3.23), (3.24) and (3.25) thus become

$$\frac{\partial \rho_{11}^{m_F' m_F}(t)}{\partial t} = \frac{\mathrm{i}}{2} \widetilde{\rho}_{10}^{m_F' 0} \mathcal{V}_{01}^{0 m_F} - \frac{\mathrm{i}}{2} \widetilde{\rho}_{01}^{0 m_F} \mathcal{V}_{01}^{0 m_F' *} - \Gamma_{\text{el}}^{F=1} \rho_{11}^{m_F' m_F} + \delta_{m_F' m_F} \left(\frac{\Gamma_{\text{in}}}{3} \rho_{00}^{00} + \sum_{M} W_{M m_F} \Gamma_{\text{el}}^{F=1} \rho_{11}^{MM} \right), \tag{3.50}$$

$$\frac{\partial \rho_{00}^{00}(t)}{\partial t} = \sum_{m_F} \frac{\mathrm{i}}{2} \widetilde{\rho}_{01}^{0 m_F} \mathcal{V}_{01}^{0 m_F *} + \text{c.c.} - \Gamma_{\text{in}} \rho_{00}^{00} \tag{3.51}$$

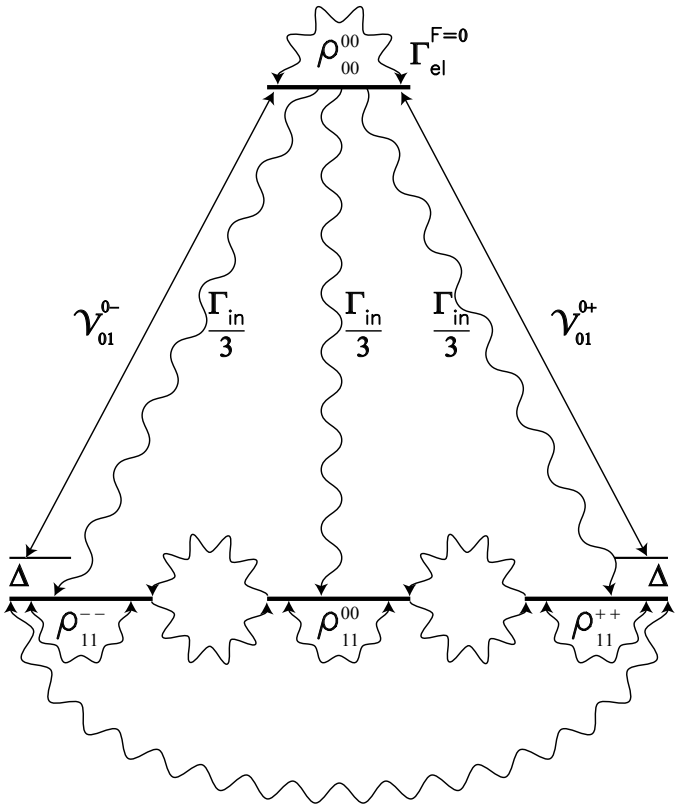

Figure 3.6: 4-levels system energy diagram for $\mu^3\mathrm{He}^+$. ρ_{11}^{--}, ρ_{11}^{00} and ρ_{11}^{++} are the sub-levels of the triplet ground state and ρ_{00}^{00} is the singlet excited state. There are transitions due to the laser, with strength given by the Rabi frequencies $\mathcal{V}_{01}^{0+}$ and $\mathcal{V}_{01}^{0-}$, and transitions due to collisions with rate Γ_{in}. There are also elastic collisions of the excited state with rate $\Gamma_{\mathrm{el}}^{F=0}$, and of the ground state with rate $W_{mm'}\Gamma_{\mathrm{el}}^{F=1}$.

and

$$\frac{\partial\widetilde{\rho}_{01}^{0m_F}(t)}{\partial t} = \frac{\mathrm{i}}{2}\rho_{00}^{00}\mathcal{V}_{01}^{0m_F} - \sum_{M=-1}^{1}\frac{\mathrm{i}}{2}\rho_{11}^{Mm_F}\mathcal{V}_{01}^{0M} - \mathrm{i}\,\Delta\widetilde{\rho}_{01}^{0m_F} - \frac{1}{2}\Big(\Gamma_{\mathrm{in}} + \Gamma_{\mathrm{el}}^{F=1} + \Gamma_{\mathrm{el}}^{F=0} + \Gamma_l\Big)\widetilde{\rho}_{01}^{0m_F}\,. \quad (3.52)$$

Finally, the Bloch equations with decays are deduced for all possible cases (2-levels μH, 4-levels μH and 4-levels $\mu^3\mathrm{He}^+$). In the next chapter further specificities of the experiments are provided and and accounted for in the present equations. After these adjustments, the equations are ready to be implemented.

4

Experimental Applications

In the previous chapter, the Bloch equations with decays were deduced for 3 different systems, 2-levels equations for μH ((3.41), (3.42) and (3.43)), 4-levels equations for μH ((3.44), (3.45) and (3.46)) and 4-levels equations for μ^3He^+ ((3.50), (3.51) and (3.52)). These equations are enough to describe the dynamics of the systems, however, there are still mechanisms in the experiments that have not been taken into account in the Bloch equations and need to be properly modeled.

In chapter 1, three different types of experiments are discussed in detail, μH diffusion experiment, μH asymmetry experiment and μ^3He^+ asymmetry experiment. The detection mechanism for each experiment was also discussed and is summarised here:

- Diffusion experiments: the fast atoms resulting from collisional inelastic decays, i.e. the collisionally quenched atoms, are detected.
- Asymmetry experiments: the electrons resulting from muon decay are detected according to their position.

In this chapter, the populations of the detected particles (collisionally quenched atoms in diffusion and electrons in asymmetry) are incorporated in the already deduced Bloch equations, according to the type of experiment. The initial conditions of each experiment as well as the inclusion of the Doppler effect, due to the thermal motion of the surrounding gas, are also discussed.

By the end of this chapter, all the necessary equations to describe the phenomena in each experiment have been presented, and they can be implemented computationally, which is discussed in chapter 5.

4.1 μH Diffusion Experiments

The CREMA-HyperMu and FAMU experiments both rely on the same method, the μH is excited to the triplet state and after collisional decay, it carries some extra kinetic energy. In the FAMU experiment, the muon transfer rate to the target gas increases with the increase in kinetic energy of the μH, and the muonic gas emits x-rays as it decays to

its ground state. These x-rays are detected, identifying the resonance energy for which the the transfer function was higher [53]. In the HyperMu experiment, the extra kinetic energy allows the μH to reach the walls of the chamber, where it is detected (see section 1.6 for more details). However it can be noticed that these atoms with extra kinetic energy have such velocity boost that induces a big Doppler shift in the HFS transition energy. This means that these atoms are blind to the laser, and their state receives the name "dark state"due to this blindness. The population of these atoms should thus be treated differently.

For the 2-levels case, the dark state population is given by

$$\frac{\partial \rho_{DS}}{\partial t} = \Gamma_{\text{in}} \rho_{11} \,, \tag{4.1}$$

and the ground state no longer has the term $+\Gamma_{\text{in}}\rho_{11}$, since the F= 1 atoms are decaying into the dark state, not the ground state. The ground state is then again given by the Bloch equation (3.14). The remaining populations are still given by equations (3.42) and (3.43), deduced in section 3.5.1.

For the 4-levels case the dark state is equivalent to the 2-levels case,

$$\frac{\partial \rho_{DS}}{\partial t} = \Gamma_{\text{in}} \left(\rho_{11}^{--} + \rho_{11}^{00} + \rho_{11}^{++} \right), \tag{4.2}$$

the ground state is again given by the Bloch equation without decays (3.16) (the excited state no longer decays to ρ_{00}^{00} but to ρ_{DS}), and the remaining equations are still given by equations (3.45) and (3.46) deduced in section 3.5.2.

It is important to notice three aspects: the first one is that the equations of the excited levels and the coherent populations did not change. This is because the states are still decaying with the same rates, just to a different state. The second one is that the dark state is a cumulative of all the atoms that have decayed, which means that at any instant, the dark state population corresponds to all the events so far. The third one is the decay of the muon itself. The muon decay was not included in the equations, as its only contribution is to reduce the populations by an exponential like $\exp\left(-\Gamma_\mu t\right)$, which means that the total population (which should be one) is decaying as well. Although this effect would make the equations more complete, it does not add any extra information on the role of polarization, since it the muon decay would only make all the populations decay exponentially to 0. The muon decay can therefore treated elsewhere.

With the experimental method for detection accounted for, these equations are ready to be implemented. To check if different polarizations produce different solutions, the 4-levels solutions with different values for η, must be compared, and also compared with the 2-levels solutions, verifying which polarization if any, produces a higher peak of the dark state, the population to be detected.

Naturally, to implement this equations, boundary conditions must be taken into account as well. In this case, the boundary conditions are the initial values of the populations, which are easily obtained to be

$$\rho_{00}(0) = 1, \quad \rho_{11}(0) = 0, \quad \rho_{01}(0) = 0 \tag{4.3}$$

for the 2-levels case, and

$$\rho_{00}^{00}(0) = 1, \quad \rho_{11}^{m'm}(0) = 0, \quad \rho_{01}^{0m}(0) = 0 \tag{4.4}$$

for the 4-levels case. These initial values are due to the process formation of the muonic atoms explained in section 1.3. In this process all the atoms formed are in the ground state, and so, the population of the ground state is 1, while the population of the excited state is 0. Furthermore, since $\rho_{11}^{mm}(0) = \left|a_1^m(0)\right|^2$, then $a_1^m(0) = 0$, and thus the coherent populations are all 0 at the initial time. Obviously, the initial condition for the dark state is $\rho_{\mathrm{DS}}(0) = 0$, since no atom has decayed yet.

4.2 μH Asymmetry Experiment

In section 1.7, it is discussed the asymmetry experiment for μH: the laser excites the atom to a sub-level of the triplet excited state, and after muon decay, the resulting electron is ejected to opposite sides depending on the angular momentum F's z component, m_F, allowing to detect the population of $m_F = 1$ and $m_F = -1$ separately. The atoms in the state $m_F = 0$ (this includes both the excited and the ground state), will contribute equally to the detections of each sub-level, i.e. the ejected electrons from these atoms will be ejected to either direction with a fifty percent chance.

The overall population of the muonic atoms will decrease over time, as the population of electrons increases. The population of electrons is composed by three types, the electrons that came from a $m_F = -1$ atom, ρ_e^-, the ones that came from a $m_F = 1$ atom, ρ_e^+, and the ones that came from a $m_F = 0$ atom and are contributing to the background, ρ_e^0.

Including now the decay of the muons, $\Gamma_\mu = {}^{2\pi}/_{\tau_\mu}$ (in rad/s), into equations (3.44), (3.45) and (3.46), and using the Lindblad formalism of section 3.4.1,

$$\frac{\partial \rho_{00}^{00}(t)}{\partial t} = \sum_{m_F} \frac{\mathrm{i}}{2} \mathcal{V}_{10}^{m_F 0} \widetilde{\rho}_{01}^{0 m_F} + \text{c.c.} + \Gamma_{\mathrm{in}} \rho_{11}^{m_F m_F} - \Gamma_\mu \rho_{00}^{00}\,, \tag{4.5}$$

$$\frac{\partial \rho_{11}^{m'_F m_F}(t)}{\partial t} = \frac{\mathrm{i}}{2} \widetilde{\rho}_{10}^{m'_F 0} \mathcal{V}_{10}^{m_F 0 *} - \frac{\mathrm{i}}{2} \widetilde{\rho}_{01}^{0 m_F} \mathcal{V}_{10}^{m'_F 0} - \left(\Gamma_{\mathrm{in}} + \Gamma_{\mathrm{el}}^{F=1} + \Gamma_\mu\right) \rho_{11}^{m'_F m_F} + \delta_{m'_F m_F} \sum_{M=-1}^{1} \frac{\Gamma_{\mathrm{el}}^{F=1}}{3} \rho_{11}^{MM} \tag{4.6}$$

and

$$\frac{\partial \widetilde{\rho}_{01}^{0 m_F}(t)}{\partial t} = \frac{\mathrm{i}}{2} \rho_{00}^{00} \mathcal{V}_{10}^{m_F 0 *} - \sum_{M=-1}^{1} \frac{\mathrm{i}}{2} \rho_{11}^{M m_F} \mathcal{V}_{10}^{M 0 *} + \mathrm{i}\,\Delta \widetilde{\rho}_{01}^{0 m_F} - \frac{1}{2}\left(\Gamma_{\mathrm{in}} + \Gamma_{\mathrm{el}}^{F=1} + \Gamma_{\mathrm{el}}^{F=0} + \Gamma_l + 2\Gamma_\mu\right) \widetilde{\rho}_{01}^{0 m_F}\,. \tag{4.7}$$

with the electron populations

$$\frac{\partial \rho_e^+}{\partial t} = \Gamma_\mu \rho_{11}^{++}, \qquad \frac{\partial \rho_e^-}{\partial t} = \Gamma_\mu \rho_{11}^{--}, \qquad \frac{\partial \rho_e^0}{\partial t} = \Gamma_\mu \left(\rho_{11}^{00} + \rho_{00}^{00}\right). \tag{4.8}$$

Equations (4.5), (4.6), (4.7) and (4.8) can be implemented, using the same initial conditions of the previous section, (4.4), with the extra conditions of $\rho_e^+(0) = \rho_e^-(0) = \rho_e^0(0) = 0$ since no muon has decayed at the initial time.

In the asymmetry experiments, the role of polarization is already well known, left or right circular polarization will produce a maximum asymmetry in the sub-levels populations, with which the transition energy can be obtained. This result is obtained from the equations (4.5), (4.6) and (4.7), since for circular polarization, lets use right circular polarization without lost of generalization, the Rabi frequency $\mathcal{V}_{10}^{+0}$ is zero, $\mathcal{V}_{10}^{-0}$ is at its maximum value and $\mathcal{V}_{10}^{00}$ is always zero. This means that the only pumping mechanism to the upper $F=1$ state is through the $m_F=-1$ state, which will be at its maximum, resulting in a maximum value for the asymmetry. However, it is important to study the intensity of the signal to be detected, as well as small deviations from perfectly circular polarizations, since the real laser could be different from the idealized circularly polarized laser.

Experimentally, the asymmetry measure is the difference in detections of both detectors (in opposite directions). Since these detectors will also detect the background electrons (from the $m_F=0$ levels), this difference should be normalized to all the detections. The asymmetry measure is $\mathcal{A}=\frac{N_F-N_B}{N_F+N_B}$ experimentally (N_F is the number of detections in the front detector, and N_B is the number of detections in the back detector) (see section 1.7), and the computational simulation correspondence is

$$\mathcal{A} = \frac{\rho_e^- - \rho_e^+}{\rho_e^- + \rho_e^+ + \rho_e^0}\,, \tag{4.9}$$

i.e. the difference in detections normalized to all detections, assuming that approximately the same number of background electrons reach each detector. Being more exact, the definition of (4.9), is not exactly the experimental asymmetry. The electrons are not all ejected in opposite direction to the muon spin, in fact they follow an angular distribution of the form of figure 4.1. The higher the electron energy, the higher the probability of the electron being ejected in the opposite direction of the muon spin [54]. The number of muons that are detected in each detector is then going to have a random factor due to this angular distribution, and thus the asymmetry defined in (4.9) does not exactly represent the measured asymmetry.

Since the electron populations are the cumulative of all the emitted electrons, at any instant, those populations correspond to all the detections made so far, and the asymmetry measure is therefore computed with the cumulative of detections, similarly to the actual experiment.

$$\rho_e^{BG} = \rho_e^- + \rho_e^0 + \rho_e^+\,. \tag{4.10}$$

4.3 $\mu^3\mathrm{He}^+$ Asymmetry Experiment

Similarly to the μH asymmetry experiment, the detected particle are the electron emitted after muon decay. The detected electrons give information regarding the asymmetry in

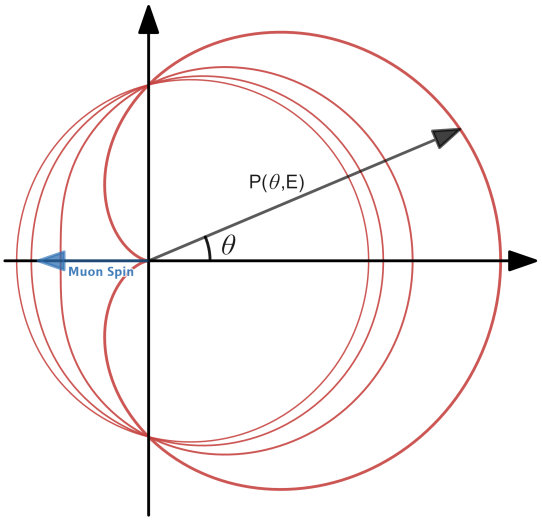

Figure 4.1: Distribution of emission of electrons in muon decay. For higher energies of the electron, the more closely the shape resembles a cardioid, and the probability of the electron being emitted in the muon spin direction decreases.

the populations of the $m_F = -1$ and $m_F = 1$ states (which in this case are part of the ground state). The electrons resulting from a $m_F = 0$ (excited state or ground state) will again contribute to a background in detections.

Using the same nomenclature as in the previous section, the electron populations are ρ_e^- for the electrons that came from $m_F = -1$ atoms, ρ_e^+ for those that came from $m_F = 1$ atoms, and ρ_e^0 for the background electrons that came from $m_F = 0$ atoms. Equations (3.50), (3.51) and (3.52) are now changed to include the muon decay.

$$\frac{\partial \rho_{11}^{m_F' m_F}(t)}{\partial t} = \frac{\mathrm{i}}{2}\widetilde{\rho}_{10}^{m_F' 0}\mathcal{V}_{01}^{0 m_F} - \frac{\mathrm{i}}{2}\widetilde{\rho}_{01}^{0 m_F}\mathcal{V}_{01}^{0 m_F'^*} - \left(\Gamma_{\mathrm{el}}^{F=1} + \Gamma_\mu\right)\rho_{11}^{m_F' m_F} + \delta_{m_F' m_F}\left(\frac{\Gamma_{\mathrm{in}}}{3}\rho_{00}^{00} + \sum_M W_{M m_F}\Gamma_{\mathrm{el}}^{F=1}\rho_{11}^{MM}\right), \tag{4.11}$$

$$\frac{\partial \rho_{00}^{00}(t)}{\partial t} = \sum_{m_F}\frac{\mathrm{i}}{2}\widetilde{\rho}_{01}^{0 m_F}\mathcal{V}_{01}^{0 m_F *} + \mathrm{c.c.} - \left(\Gamma_{\mathrm{in}} + \Gamma_\mu\right)\rho_{00}^{00} \tag{4.12}$$

and

$$\frac{\partial \widetilde{\rho}_{01}^{0 m_F}(t)}{\partial t} = \frac{\mathrm{i}}{2}\rho_{00}^{00}\mathcal{V}_{01}^{0 m_F} - \sum_{M=-1}^{1}\frac{\mathrm{i}}{2}\rho_{11}^{M m_F}\mathcal{V}_{01}^{0M} - \mathrm{i}\Delta\widetilde{\rho}_{01}^{0 m_F} - \frac{1}{2}\left(\Gamma_{\mathrm{in}} + \Gamma_{\mathrm{el}}^{F=1} + \Gamma_{\mathrm{el}}^{F=0} + \Gamma_l + 2\Gamma_\mu\right)\widetilde{\rho}_{01}^{0 m_F}. \tag{4.13}$$

and the electron populations ρ_e^-, ρ_e^0 and ρ_e^+ are given by equation (4.8).

To solve these equations, the initial conditions are needed. For the electron populations it is obvious that $\rho_e^+(0) = \rho_e^-(0) = \rho_e^0(0) = 0$ since no muon has decayed at the initial time. Considering the process of formation of μ^3He$^+$ explained in section 1.3, after formation all the atoms are in the ground state, which in this case is the triplet state. The

sub-levels are equally populated at start, $\rho_{11}^{mm}(0) = \frac{1}{3}$.

$$\rho_{00}^{00}(0) = 0, \quad \rho_{01}^{0m}(0) = 0, \quad \rho_{11}^{m'm}(0) = \frac{1}{3}\mathrm{e}^{\mathrm{i}\varphi_{m'm}} \tag{4.14}$$

where $\varphi_{m'm}$ is the phase difference between $a_1^{m'}(0)$ and $a_1^{m}(0)$. Since $\rho_{11}^{mm}(0) = \left|a_1^m(0)\right|^2$, then $\left|a_1^m(0)\right| = \frac{1}{\sqrt{3}}$, but $a_1^m(0)$ could have a phase, φ_m. As such, $\rho_{11}^{m'm}(0) = a_1^{m'}(0)a_1^{m*}(0) = \frac{1}{3}\mathrm{e}^{\mathrm{i}(\varphi_{m'}-\varphi_m)}$. These phases are fundamentally random. There are several methods to account for these type random phenomena, either with a Monte-Carlo method or with an average over all possible values of the phases. In this thesis, the second method will be employed since it is less computational heavy.

Lastly, the asymmetry measure is again given by the difference in populations of the electrons, normalized to the entire population of electrons, equation (4.9). The asymmetry for this case will again be maximum for circular polarization by the same reasoning of the previous section.

4.4 Doppler Broadening

One key detail that is not included in the equations deduced, for either types of experiments, is that the atoms are moving and thus perceive a frequency for the laser different from the one imposed experimentally. To include this effect, one easy solution is to compute the convolution of the populations with a Maxwellian distribution, which in this case is just a Gaussian (since the laser propagates in one direction, only the movement in that direction is affected) with width Γ_D,

$$\overline{\rho}(\Delta) = \int_{-\infty}^{\infty} \rho(\Delta - w)\frac{1}{\sqrt{2\pi}\Gamma_D}\exp\left(-\frac{w^2}{2\Gamma_D^2}\right)\mathrm{d}w\,, \tag{4.15}$$

and the Doppler width is

$$\Gamma_D = \omega_r\sqrt{\frac{k_B T}{(m+M)c^2}}\,, \tag{4.16}$$

where k_B is the Boltzmann constant, T the temperature of the atoms, m is the mass of the orbiting particle, the muon, and M is the mass of the nucleus, either H or ^{3}He. Although the frequency of the transition ω_r is the unknown constant that is meant to be found out, it can approximated to $\omega_r = 44.2$ THz for μH and $\omega_r \approx 322$ THz for $\mu^3\mathrm{He}^+$ [29, 47].

It is important to notice that in the asymmetry methods, the Doppler must be computed for the ρ populations, and only then the asymmetry, $\mathcal{A}$, can be calculated. What is being affected directly from the Doppler is the actual populations, not $\mathcal{A}$.

5

Computational Simulations

In this chapter, I describe the implementation of the numerical method for solving the equations of the three types of experiments obtained in the previous two chapters. All code was developed in *Wolfram Mathematica 9.0* software.

To solve the equations, it is considered that a laser with intensity $\mathcal{I}$, irradiates the muonic atoms during a time τ. It is assumed that this laser has constant intensity, thus giving a fluence of

$$\mathcal{F} = \int_0^\tau \mathcal{I} \mathrm{d}t \approx \mathcal{I}\tau \,. \tag{5.1}$$

After a time τ has passed, the laser is turned off, but the detections are still being registered. This is equivalent to solve the time dynamics equations until a time τ, then making all Rabi frequencies 0 (since they are proportional to $\sqrt{\mathcal{I}}$), and solving the equations but only with the collisional decay rates, guarantying continuity of the solutions at the time τ.

In reality, when the laser enters the chamber, it is reflected back and forth, amplifying its intensity, and virtually randomizing the laser phase. Furthermore, a more accurate description of the laser is with a Gaussian profile instead of a rectangular profile. These aspects significantly complicate the resolution of the equations, mainly due to the random nature of the laser phase. The simpler rectangular profile will therefore be considered instead. A study on the modulation of the electric field in the chamber, considering these factors can be found in Ferro's thesis [55].

Before implementing the equations, one final observation is important to notice, the symmetry in the m_F sub-states with the degree of polarization. For either μH and $\mu^3\mathrm{He}^+$ the Rabi frequency has the symmetry $\mathcal{V}_{10}^{m_F 0}(-\eta) = \mathcal{V}_{10}^{-m_F 0}(\eta)$ (or $\mathcal{V}_{01}^{0 m_F}(-\eta) = \mathcal{V}_{01}^{0 -m_F}(\eta)$). If we change all the plus indices to minus indices, the set of equations remains the same, even considering the decay rates, since the statistical weight obtained in appendix E obey this symmetry. On the other hand, a way to change the indices in the Rabi frequencies is by just changing the sign of η. This means that the changing the indices in all the populations and the sign of η gives the exact same results and thus $\rho_{11}^{++}(\eta) = \rho_{11}^{--}(-\eta)$. This symmetry allows to just compute the results for positive values of η, and consider the same values for negative polarizations.

5.1 μH Diffusion Experiments

The role of polarization in μH experiments is studied by checking if the non-polarization dependent 2-levels equations ((3.14), (3.42), (3.43) and (4.1), as well as the initial conditions (4.3)) produce the same results as the 4-levels equations ((3.16), (3.45), (3.46) and (4.2), as well as the initial conditions (4.4)) for any possible polarization.

In section 2.2, the polarization was described by two parameters, the χ (angle of the major axis of the ellipse with the x-axis) and η (ratio of the components of the electric field in the minor and major axis of the ellipse). The χ parameter is irrelevant since it can be eliminated by just choosing a reference frame where the major and minor axis of the ellipse (ellipse described by the rotation of the polarization vector) are in the x and y directions (maintaining the same z direction). The η parameter, describes the type of polarization (circular, linear, elliptical, left polarization and right polarization) with just a number, $-1 \leq \eta \leq 1$, the degree of polarization.

A flowchart of the implementation method is represented in figure 5.1. In this method, two comparisons are performed between the 2-levels case and the 4-levels cases: the time evolution of the populations; the final value of the dark-state depending on the laser relative frequency Δ.

Table 5.1: Collision rates of μH–H_2 in MHz for different pressures and temperatures of the H_2 gas. Adapted from [47].

	$T = 22$ K	$T = 30$ K	$T = 50$ K
$P = 0.5$ bar			
$\Gamma_{el}^{F=0}$	20	15	9
$\Gamma_{el}^{F=1}$	52	41	28
Γ_{in}	82	59	34
$P = 1$ bar			
$\Gamma_{el}^{F=0}$	40	30	19
$\Gamma_{el}^{F=1}$	104	83	55
Γ_{in}	164	118	68
$P = 2$ bar			
$\Gamma_{el}^{F=0}$	79	61	38
$\Gamma_{el}^{F=1}$	208	165	110
Γ_{in}	328	235	137

These calculations are performed for the possible values of the decay rates. For μH in an H_2 gas, the decay rates for temperatures and pressures of interest for the measurement by the CREMA collaboration were calculated with the theoretical formalism presented in [52, 56], and presented in [47], table 5.1. Furthermore, the simulations will be performed for fluences of $\mathcal{F} \leq 50$ Jcm^{-2}, for which it was demonstrated in [47] that the exposure time,

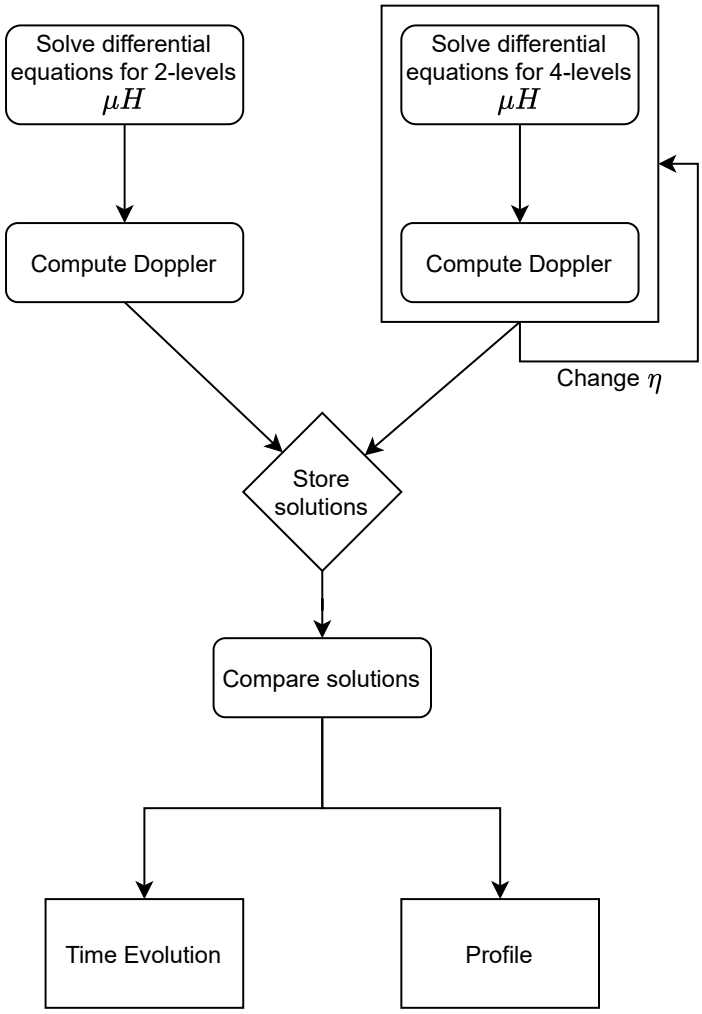

Figure 5.1: Flowchart of the implementation method in μH diffusion experiments. The solutions for the 2-levels equations and for the 4-levels equations with different polarizations, are stored, then compared in two aspects: (1) Time evolution of the populations; (2) Profile of the dark-state versus frequency of the laser. This method is employed for each set of decay rates.

τ, does not play as large of a role, and as such, only $\tau = 100$ ns will be considered.

As an initial check for the implementation method is was considered the case without decays and no Doppler effect. Since it was analytically proven in section 3.2.3 that the equations with no decays do not depend on the polarization, then the numerical implementation should yield the same result, i.e. the 2-levels and 4-levels equations produce the same result for the population of the excited triplet state. Note that if there is no quenching, the dark state will not be populated, and since $\mathcal{V}_{10}^{00} = 0$, the population ρ_{11}^{00} will be null for all times. In figure 5.2, the time evolution of the excited state (and its sub-levels) for the 2-levels and 4-levels with different polarizations can be observed. Here, the laser frequency is at resonance with the transition, and no Doppler effect was included. It can be observed that the excited level population, ρ_{11}, (and therefore the

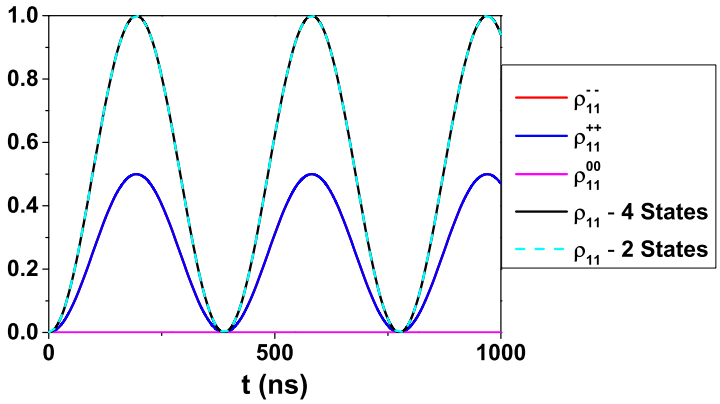

(a) Linear polarization, $\eta = 0$. The ρ_{11}^{++} (blue) and ρ_{11}^{--} (red) populations are equal.

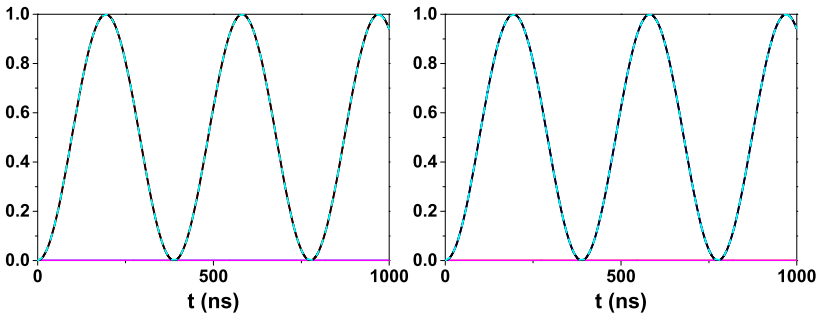

(b) Right circular polarization, $\eta = 1$. (c) Left circular polarization, $\eta = -1$.

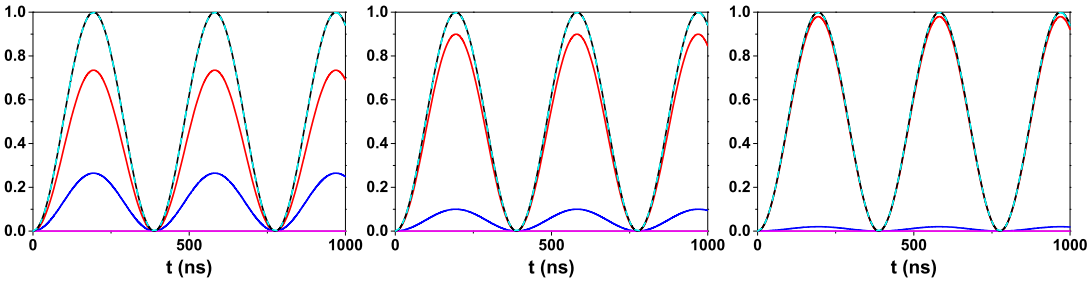

(d) Polarization $\eta = 0.25$. (e) Polarization $\eta = 0.5$. (f) Polarization $\eta = 0.75$.

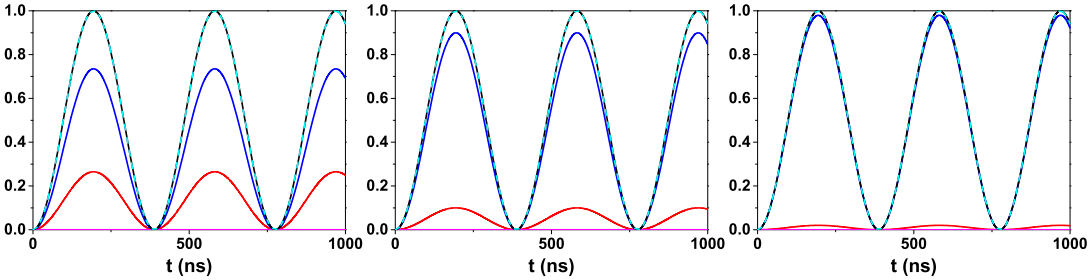

(g) Polarization $\eta = -0.25$. (h) Polarization $\eta = -0.5$. (i) Polarization $\eta = -0.75$.

Figure 5.2: Time evolution of the populations of the excited state of μH without decays. For all types of polarizations, the total excited population ρ_{11} for the 4-levels (black line) is the same as for 2-levels (dashed cyan). The population of the $m_F = 0$ sub-state (magenta line) is always zero. The population of $m_F = -1$ (red line) and $m_F = 1$ (blue line) oscillates with maximum amplitude for $\eta = \pm 1$ respectively, where it is equal to ρ_{11}. Solutions obtained for a laser at resonance and with fluence of $\mathcal{F} = 10$ Jcm^{-2} during $\tau = 1000$ ns.

ground state as well) is always the same, there is only a trade-off between which of the sub-level is populated, either is the $m_F = -1$ for right circular polarization $\eta = 1$, the $m_F = 1$ for left circular polarization $\eta = -1$, or equally populated for linear polarized light $\eta = 0$. This result is in perfect agreement with theory, thus giving confidence that the numerical integration has no observable inaccuracies and the 2-level and 4-level equations are well implemented.

In figure 5.2, the symmetry discussed at the beginning of this chapter is evident. Furthermore, increasing η, from -1 to 1, turns the populated state from $m_F = 1$ to $m_F = -1$, with them being equal for linear polarization.

When considering the decays of table 5.1, the time evolution of the populations becomes more complicated than the simple sine solution of figure 5.2. In this case, the excited state ρ_{11} does decay to the dark state, for which the population will increase over time. This increase extends after the laser is shut off with the remaining excited atoms. In figure 5.3, the plotted solutions where computed for all possible temperatures and pressures of table 5.1, and with laser at resonance with a fluence of $\mathcal{F} = 10$ Jcm^{-2} during $\tau = 100$ ns.

In figure 5.3, there seems to be no difference between the 2-levels case, and the 4-levels case, regardless of the polarization considered. To quantify the difference between the 2-levels case and the 4-levels case, the Least Minimun Squares (LMS) was computed as

$$LMS = \sqrt{\sum_i \left(\rho^{2\text{States}}(q_i) - \rho^{4\text{States}}(q_i)\right)^2}, \tag{5.2}$$

where q is the parameter being studied. In this case q is the time, the LMS is obtained to be a maximum of $\text{LMS}_{DS} = 1.65 \times 10^{-3}$ and $\text{LMS}_{11} = 8.56 \times 10^{-5}$ for $\eta = 0$, $T = 50$ K and $P = 0.5$ bar. These LMS values are smaller then a tenth of the value of the smaller division of the vertical axis, which shows how little these solutions differ over three orders of magnitude in time. For every other possible polarization, temperature or pressure, the LMS will be even smaller, going as small as $\text{LMS}_{DS} = 1.69 \times 10^{-5}$ and $\text{LMS}_{11} = 1.14 \times 10^{-7}$, for $\eta = \pm 1$, $T = 22$ K and $P = 2$ bar. Overall, cases with higher decay rates have lower LMS values, as well cases with a higher degree of polarization (more circular than linear).

An argument can be made that the small errors between the 2-levels and 4-levels are due to the numerical method of the differential equations. In *Wolfram Mathematica 9.0*, the method for the numerical integration of differential equations is chosen automatically from its libraries, such that the solution has the least errors. In numerical simulations, since the solutions are computed in steps, less oscillating equations have smaller deviations between steps, making the cumulative errors lower than in higher oscillating systems. The cases where the decay rates are higher, the populations oscillate less because they tend to decay and stabilize to some value, and thus the LMS error is lower. To understand why the cases with more circular polarization have lower errors, it is easier to look at the extreme case of $\eta = \pm 1$. In this situation, only of the sub-levels of $F = 1$, is oscillating and the others are constant and null, and they will not add any errors.

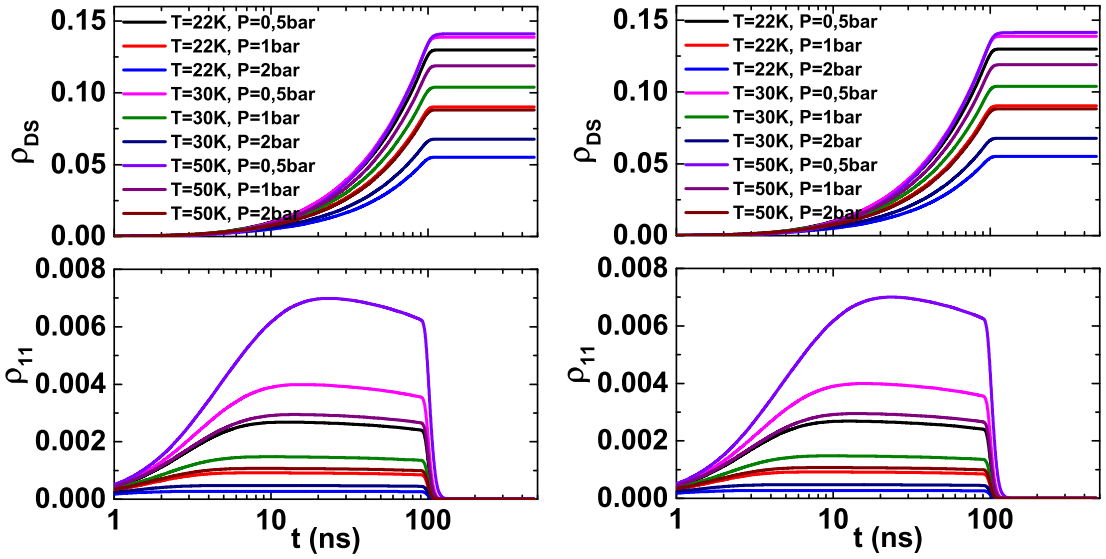

(a) 2-levels

(b) 4-levels, linear polarization, $\eta = 0$.

(c) 4-levels, polarization $\eta = 0.5$.

(d) 4-levels, right circular polarization, $\eta = 1$.

Figure 5.3: Time evolution of the populations of the excited state and dark state of μH for the 2-levels case, and for the three polarizations in the 4-levels case. These solutions were obtained for a laser at resonance, and with fluence of $\mathcal{F} = 10$ Jcm^{-2} during $\tau = 100$ ns.

Regardless of the reason as to why the equations aren't producing exactly the same result (either computational errors, or the equations do actually have different solutions), what is important is that they will describe the system in the same manner, with a great relative accuracy.

By checking the numerical results, it is clear that the time evolution of the dark state and its stabilization point does not depend on the polarization with.

It is important to also check the behaviour of the dark state when the laser is not at resonance. This is studied by plotting the profile of the dark state, i.e. the final (and stable) value of the dark state versus the laser frequency, or more accurately, versus $\Delta = \omega_r - \omega$. e.g. figure 5.4, where fluences of 10 Jcm^{-2} and 20 Jcm^{-2} during $\tau = 100$ ns, with a bandwidth of 100 MHz (and a case with a low bandwidth of 10 MHz) were considered. Here the Doppler effect as described in section 4.4 was included. This was performed for all possible combinations of temperatures (22 K, 30 K and 50 K), pressures (0.5 bar and 1 bar), fluences (10 Jcm^{-2}, 20 Jcm^{-2} and 50 Jcm^{-2}) and laser bandwidth (10 MHz and 100 MHz), and a summary of the peak and Full Width Half Maximum (FWHM) values can be found in appendix F. In those tables, as well as in figure 5.4, it is again clear that the dark state from the 2-levels equations is stabilising to same values as the dark-state of the 4-levels equations. There are some differences in those tables that are mainly due to rounding of the last digit. The fact that the most of the differences (although not much) are between the 2-levels solutions and the 4-levels solutions, and not between the 4-levels solutions with themselves, suggests that these small differences may arise due to the numerical solve. Since the 4-levels equations are quite more complex, they have more numerical errors, deviating more from the real solution. This happens to all the 4-levels solutions equally, but not as much for the 2-levels solutions (which have a simpler set of equations to solve), justifying the small differences found in the tables of appendix F.

In figure 5.4, it is impossible to visually identify any difference in the solutions. Computing the LMS values of the profile of the dark state in 4-levels, relative to the 2-levels, gives a maximum of $\mathrm{LMS}_\Delta = 1.91\times10^{-2}$ for linear polarization ($\eta = 0$), $T = 50$ K, $P = 0.5$ bar, $\Gamma_l = 10$ MHz and a fluence of $\mathcal{F} = 50$ Jcm^{-2}, which is the case with lower decay rates. As in the time evolution graphs, the cases with lower decay rates, as well as polarizations closer to linear, produced a higher LMS values relative to the 2-levels case. For higher fluences, the Rabi frequency will be greater ($|\mathcal{V}_{10}| \propto \sqrt{\mathcal{F}}$), and the system will oscillate faster thus providing more room for numerical errors. For a fluence of $\mathcal{F} = 10$ Jcm^{-2} the maximum LMS is $\mathrm{LMS}_\Delta = 2.64\times10^{-3}$, and for $\mathcal{F} = 20$ Jcm^{-2} is $\mathrm{LMS}_\Delta = 7.58\times10^{-3}$, both are for linear polarization, $T = 50$ K, $P = 0.5$ bar and $\Gamma_l = 10$ MHz (the black line in the graphs of 5.4). Just like in the time evolution graphs, here the LMS is about a tenth of the value of the smaller division of the vertical axis. The tables in appendix F also include the values of LMS_Δ.

The simulations on the 2-levels case and on the 4-levels case, had almost identical results, regardless of the polarization. The LMS error relative to the 2-levels case is minimal, and can be easily explained with computational errors of the numerical implementation.

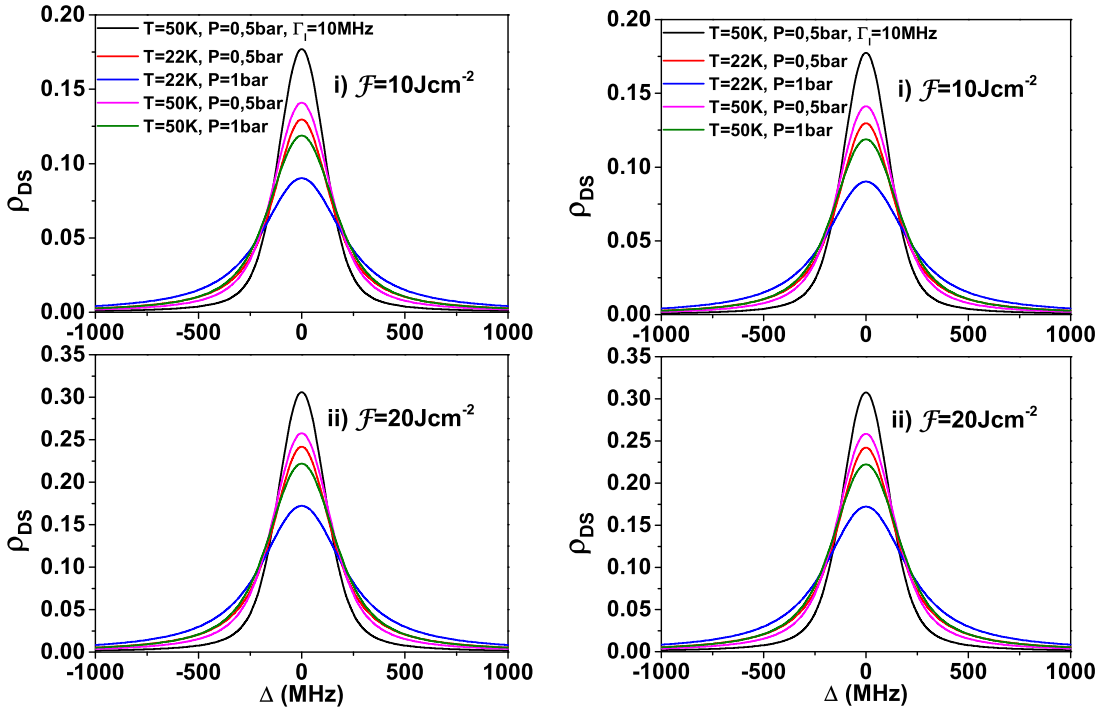

(a) 2-levels

(b) 4-levels, linear polarization, $\eta = 0$.

(c) 4-levels, polarization $\eta = 0.5$.

(d) 4-levels, right circular polarization, $\eta = 1$.

Figure 5.4: Profile of the populations of the dark state of μH for the 2-levels case, and for the three polarizations in the 4-levels case, $\eta = 0, 0.5, 1$. These solutions were obtained for a laser with $\tau = 100$ ns and for two fluences: i) $\mathcal{F} = 10$ Jcm^{-2} and ii) $\mathcal{F} = 20$ Jcm^{-2}. The laser bandwith was considered to be 100 MHz for all case except for the black lines where $\Gamma_l = 10$ MHz.

The populations of the dark state stabilize after the laser is shut off (and the F= 1 states decay), and this stability value does not have any dependence on the polarization as well, only on the experimental parameters: temperature, pressure, laser bandwidth and fluence. As such it can be concluded that the polarization does not play any role (at least numerically) in diffusion experiments of μH.

5.2 Asymmetry Experiments

For asymmetry experiments, it is explained in section (4.2) that circular polarization outputs the highest value for the asymmetry measure defined in equation (4.9). The study on the role of polarization in this thesis has the goal of investigating how the polarization will affect the asymmetry measure, in order to check how accurate the laser polarization must be, i.e. how far from a circular polarization the a laser polarization can be, without the asymmetry measure dropping significantly.

To perform the analysis on the polarization for an asymmetry system, the population

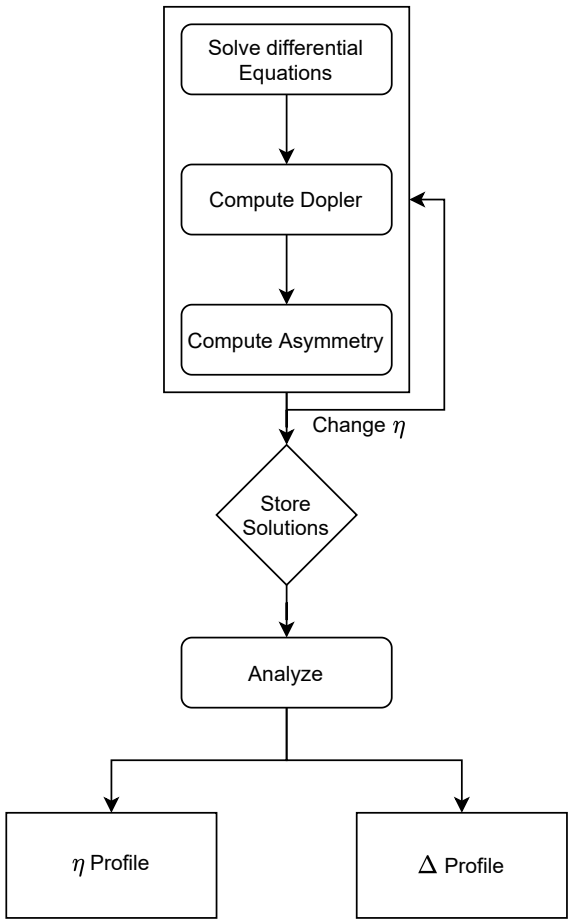

Figure 5.5: Flowchart of the implementation method in asymmetry experiments. The Δ profile solutions for different polarizations are stored and compared. The η profile solutions at resonance are stored and compared for different decay rates.

equations for μH ((4.5), (4.6) and (4.7), as well as the electron populations (4.8) and the boundary conditions (4.4)) and for μ^3He^+ ((4.11), (4.12) and (4.13), as well as the electron populations also given by (4.8) and the boundary conditions (4.14)) where implemented with the method described in figure 5.5. Two aspects of the solutions were studied: The relative frequency, Δ, dependency, and the polarization dependency at resonance. These profiles are computed not for the final time (after the laser is off), but for the final time with the laser on, τ.The implementation method is repeated for different decay rates.

5.2.1 Asymmetry in μH

If only the muon decay rate is considered, the expected solutions have a oscillating behaviour similar to those of figure 5.2, but bounded by an exponential decay with rate Γ_μ. This is observed in figure 5.6(a), where the time evolution of the muon populations is shown. This decay is compensated by the growth of electron populations, which follows a growth with rate Γ_μ, maxing out at 1, figure 5.6(b). In figure 5.6, it was considered a laser

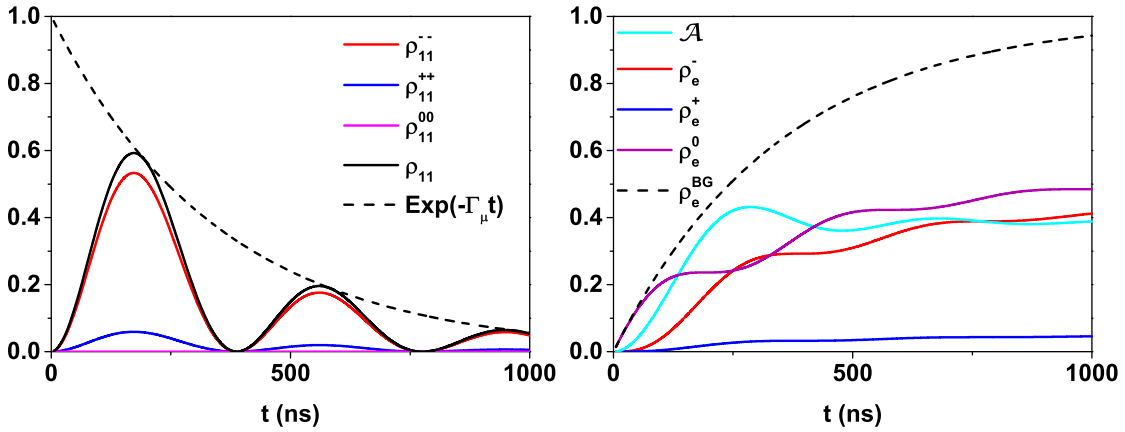

(a) Atomic populations.

(b) Electron populations.

Figure 5.6: Time evolution of the $F=1$ states (a) and electron populations (b) of μH for polarization $\eta=0.5$. The atomic populations in (a) are the $m_F=-1$, 0, 1 (red, magenta and blue lines respectively) and the total $F=1$ population (black line). The exponential decay of the atomic populations is included in (a) (black dashed line). The electron populations in (b) are the ρ_e^- (red), ρ_e^+ (blue) and ρ_e^0 (purple). The asymmetry measure $\mathcal{A}$ is included (cyan line), and the total electron population, ρ_e^{BG} is a negative exponential decay complementing the exponential decay of (a). These results were obtained for $\mathcal{F}=10$ Jcm^{-2}, during $\tau=1000$ ns.

with fluence $\mathcal{F}=10$ Jcm^{-2}, during $\tau=1000$ ns, and with polarization degree of $\eta=0.5$ so that the difference in the $m_F=\pm1$ populations is observable. The time evolution for polarizations between $\eta=0$ and $\eta=1$ (except $\eta=0.5$) can be found in appendix G. Once more, increasing the η from -1 to 1 turns the populated state from $m_F=1$ to $m_F=-1$, being equal for linear polarization $\eta=0$. Here, the same happens for the electron populations.

Considering now the decay rates, these are again given by table 5.1, as the atomic system and the surrounding gas are the same. Just as in section 5.1, the decay rates have the effect of stabilising the populations, which in turn stabilise the electron populations and the asymmetry. This can be observed in figure 5.7, where the time evolution of the electron ρ_e^- and ρ_e^+ populations and the asymmetry (given by equation (4.9)) are plotted for different polarizations, always at resonance.

Specific values for the fluence ($\mathcal{F}$= 10 Jcm^{-2}), laser bandwidth (100MHz) and decay rates are presented in this section. The chosen values correspond to high decay rates (T= 50 K and P= 0.5 bar), low decay rates (T= 22 K and P= 1 bar) and intermediate decay rates (T= 50 K, P= 1 bar). Other combinations are included in appendix G. Naturally, for higher decay rates, there electron populations ρ_e^- and ρ_e^+ will be lower, as the ρ_{11}^{--} and ρ_{11}^{++} populations are also lower.

The results of figure 5.7 show that regardless of the decay rates, the asymmetry achieves its highest value for circular polarization, and lowest for linear polarization, evaluating always to zero. This result is what is predicted and described in section 4.2. Furthermore, the increase in the ρ_e^- population when deviating from linear polarization is in its entirely complemented by the decrease in the ρ_e^+, i.e. $\rho_e^- + \rho_e^+$ being constant for all polarizations, meaning that the ρ_e^0 stays the same for all polarizations.

It is important to notice that after the laser is turned of, the asymmetry drops significantly. This happens because the ρ_{11}^{--} and ρ_{11}^{++} are quite small relative to the ground state ρ_{00}^{00} (which is the main responsible for the background electrons), and so there will not be much more decays to the ρ_e^- and ρ_e^+ populations (the asymmetry, not normalized to the background population, stays basically the same). However, there still be much more decays (comparatively) to the ρ_e^0, increasing the background detections, and lowering the asymmetry $\mathcal{A}$. For this reason, the profile plots (for both Δ and η) are computed for the asymmetry value at time τ (at which the laser is shut off).

The Δ profile of the asymmetry at time τ can then be computed for different polarization values. Here, only the plots for the low, medium and high decay rates are shown. The results of figure 5.8 are all for a laser with fluence $\mathcal{F}$= 10 Jcm^{-2}, on for τ= 100 ns. In appendix H, tables of the FWHM and peak value of the asymmetry for the different polarizations are presented. In it, the results for linear polarization are not presented, as the asymmetry is always zero.

As predicted from the time evolution plots of figure 5.7, it is observed in figure 5.8 that the closer the polarization is to circular polarization, the higher is the asymmetry, and moreover, this happens for every laser frequency.

The curve in figure 5.8(b) has slightly different shape from the other curves because for small decay rates (decoherence rate, Γ_c) comparative to the Rabi frequency, the solutions approach the Rabi-oscillating regime ($\Gamma_c = \Gamma_{\text{in}} + \Gamma_{\text{el}}^{F=1} + \Gamma_{\text{el}}^{F=0} + \Gamma_l \leq |\mathcal{V}|$). In this regime, the solutions oscillate similarly to figure 5.6(a) (when at resonance), and their profile at time

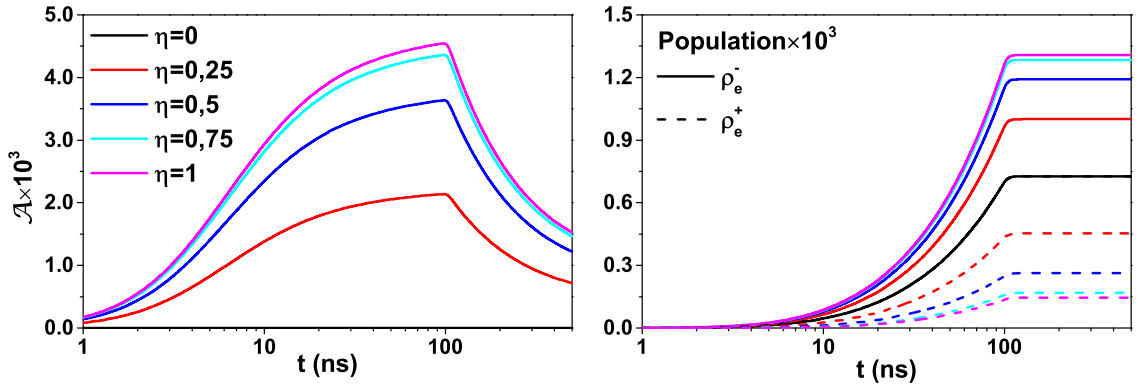

(a) Low decay rates: $T = 50$ K and $P = 0.5$ bar.

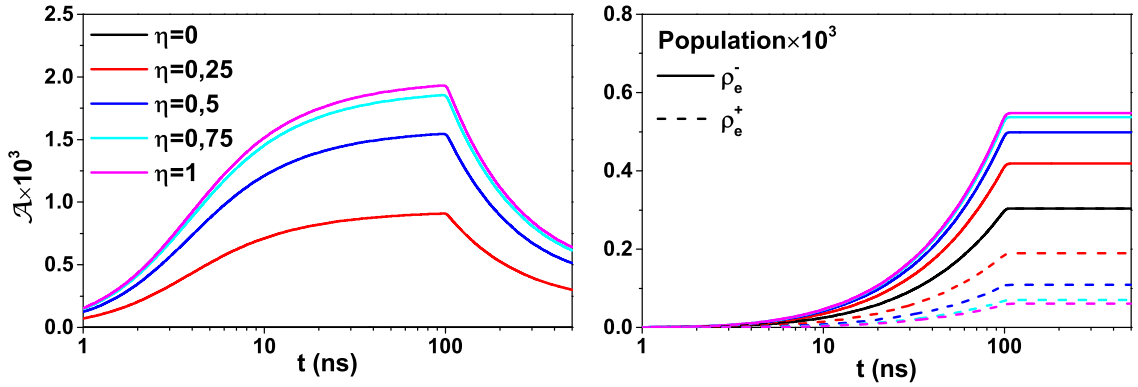

(b) Intermediate decay rates: $T = 50$ K and $P = 1$ bar.

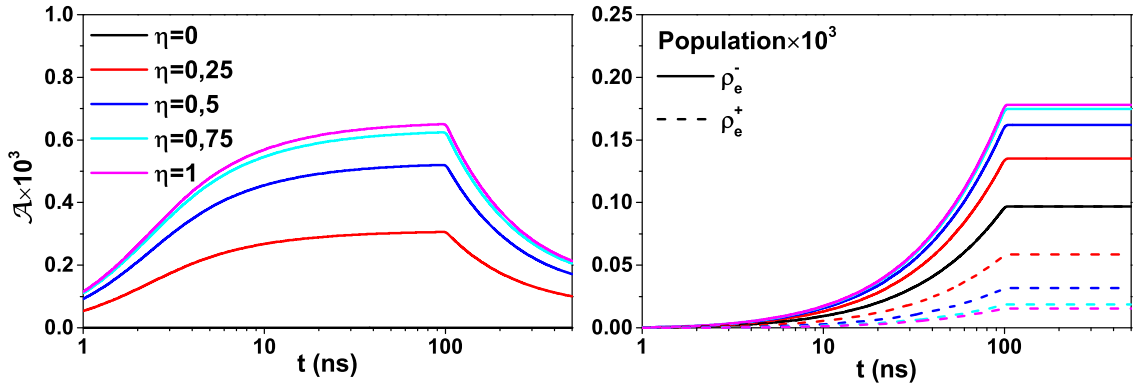

(c) High decay rates: $T = 22$ K and $P = 1$ bar.

Figure 5.7: Time evolution of the asymmetry $\mathcal{A}$ (left) and electron populations (right) of μH for low (a), intermediate (b), and high (c) decay rates, multiplied by a factor of 10^3. Solutions for polarizations $\eta = 0$, 0.25, 0.5, 0.75, 1 are represented with black, red, blue, cyan and magenta lines, respectively. Electron population in the figures on the right are represented with solid lines for ρ_e^- and dashed lines for ρ_e^+. These results were obtained for $\mathcal{F} = 10$ Jcm^{-2}, during $\tau = 100$ ns.

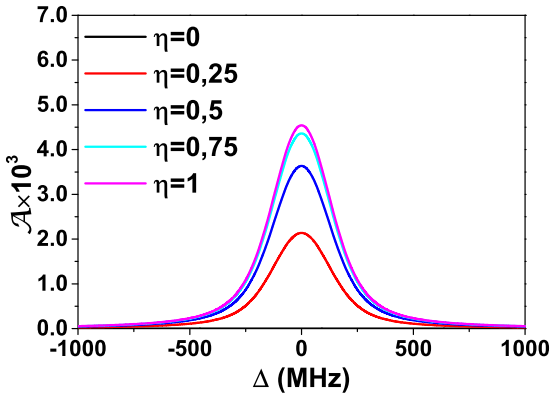

(a) Low decay rates: T= 50 K and P= 0.5 bar with Γ_l= 100 MHz.

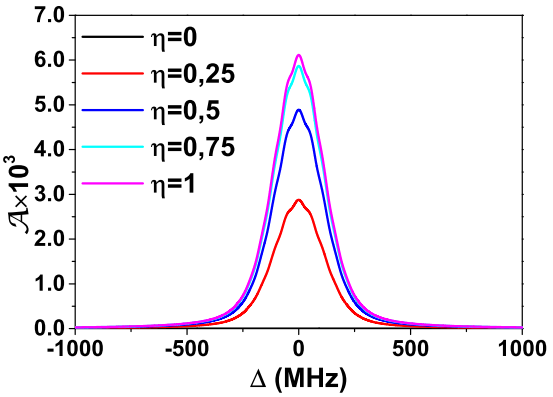

(b) Low decay rates: T= 50 K and P= 0.5 bar with Γ_l= 10 MHz.

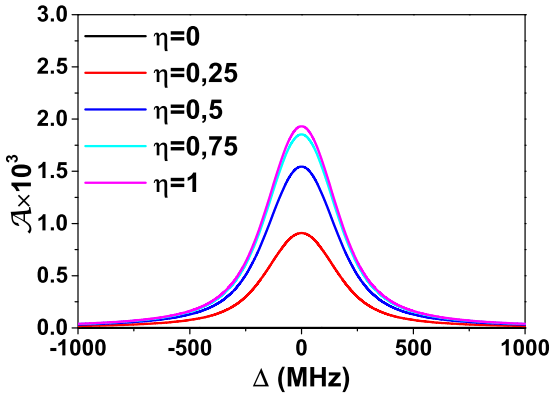

(c) Intermediate decay rates: T= 50 K and P= 1 bar with Γ_l= 100 MHz.

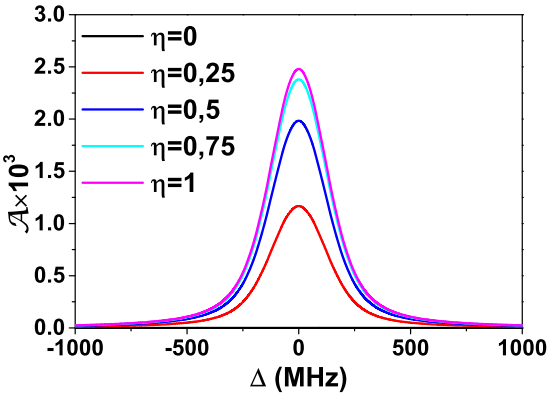

(d) Intermediate decay rates: T= 50 K and P= 1 bar with Γ_l= 10 MHz.

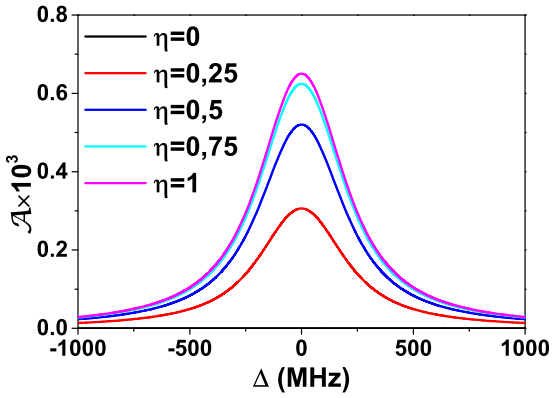

(e) High decay rates: T= 22 K and P= 1 bar with Γ_l= 100 MHz.

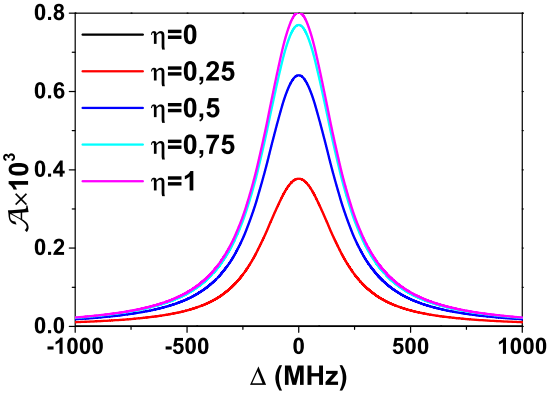

(f) High decay rates: T= 22 K and P= 1 bar with Γ_l= 10 MHz.

Figure 5.8: Δ profile of the asymmetry, $\mathcal{A}$. For three combinations of temperatures and pressures (corresponding to low, intermediate and high decay rates). A laser with fluence $\mathcal{F}$= 10 Jcm^{-2}, on during a time of τ= 100 ns was considered. Two bandwidths were considered for this laser 10 MHZ and 100 MHz. In the figures, the color represent the polarization degree, which assume the values η= 0 , 0.25 , 0.5, 0.75, and 1, corresponding to the colors black, red, blue, cyan and magenta respectively. For linear polarization $\mathcal{A}$= 0 for all times (there is no asymmetry).

τ are of the form

$$\rho_{11}^{mm}(\tau,\Delta) = \frac{\left|\mathcal{V}_{10}^{m0}\right|^2}{|\mathcal{V}_{10}|^2+\Delta^2}\sin^2\left(\frac{\tau}{2}\sqrt{|\mathcal{V}_{10}|^2+\Delta^2}\right), \tag{5.3}$$

which has oscillations along Δ, bounded by a Lorentzian profile [46]. This regime is never actually reached experimentally, and so it will not be discussed in this thesis, more information on it can be found in [47].

It is important to notice that, with the same set of parameters, the peak value of the asymmetry for a polarization of η= 0.75 has barely any difference from the maximum possible peak of η= 1. More precisely, if the laser has a polarization error of 25% (relative to circular polarization), the loss in asymmetry $\Delta\mathcal{A}$, given by

$$\Delta\mathcal{A}(\eta) = \frac{\mathcal{A}^{\text{Peak}}(\eta=1)-\mathcal{A}^{\text{Peak}}(\eta)}{\mathcal{A}^{\text{Peak}}(\eta=1)}, \tag{5.4}$$

is only 4%. The calculated losses in asymmetry were found not to have any dependence on the experimental parameters, such as temperature, pressure, fluence and laser bandwidth, only the polarization degree itself. The losses in asymmetry are summarized in table 5.2. Naturally, if the laser has right circular polarization, η= 1, the loss in asymmetry relative

Table 5.2: Loss in asymmetry relative to right circular polarization for different values of polarization degrees.

	$\eta=0$	$\eta=0.25$	$\eta=0.5$	$\eta=0.75$	$\eta=1$
$\Delta\mathcal{A}$ [%]	100	53	20	4	0

to the circular polarization will be zero, and if it has linear polarization, the asymmetry is completely lost.

A more detailed study on the asymmetry dependence on the polarization can be done with η profile plots. Plotting this profile in the same conditions as before ($\mathcal{F}$= 10 Jcm^{-2}, Γ_l= 100 MHz and at resonance, Δ= 0 MHz), but with more possibilities for the decay rates, gives the results of figure 5.9(a). All these curves appear to have the follow the same type of shape. This becomes obvious if they are normalized to their maximum value (corresponding to $\mathcal{A}^{\text{Peak}}(\eta=1)$, where the "Peak"means that it is at resonance), as seen in figure 5.9(b).

The shape of this curve can be identified to be the degree of circular polarization (or Stokes parameter V_S) in equation (2.41)

$$\frac{\mathcal{A}^{\text{Peak}}(\eta)}{\mathcal{A}^{\text{Peak}}(\eta=1)} = \frac{2\eta}{1+\eta^2}, \tag{5.5}$$

which is explained by the relation of the populations and their respective Rabi frequency. Each population of the excited state is proportional to its Rabi frequency squared (equation (5.3)), which in turn is proportional to the one of the components of the polarization

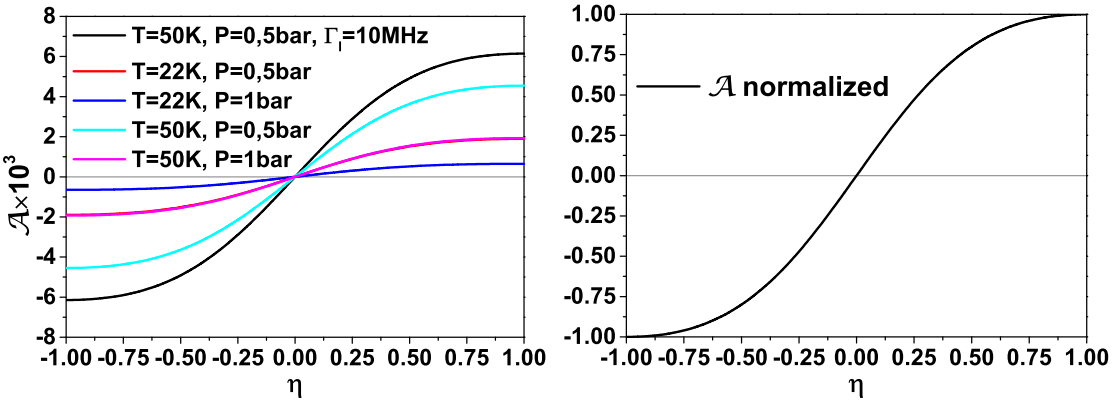

(a) η profile of $\mathcal{A}^{\text{Peak}}$.

(b) η profile of $\mathcal{A}^{\text{Peak}}$ normalized to $\mathcal{A}^{\text{Peak}}(\eta = 1)$.

Figure 5.9: Profile of the asymmetry taken for resonance at time τ. Results in (a) were taken for $\mathcal{F}$= 10 Jcm^{-2} and Γ_l= 100 MHz, except the black line which was with Γ_l= 10 MHz. All curves normalized to their maximum value $\mathcal{A}^{\text{Peak}}(\eta = 1)$ result in the same curve of figure (b).

vector of the magnetic field, $\hat{\mathbf{k}} \times \hat{\varepsilon}$,

$$\rho_{11}^{\pm\pm} \propto \left|\mathcal{V}_{10}^{\pm 0}\right|^2 \propto \left|\left(\hat{\mathbf{k}} \times \hat{\varepsilon}\right)_{\pm}\right|^2 = \frac{1}{2}\frac{(\eta \mp 1)^2}{\eta^2 + 1} \tag{5.6}$$

If we compute the asymmetry between the ρ_{11}^{--} and ρ_{11}^{++} sub-states, we notice that it must be proportional to the quantity of equation (5.5),

$$\rho_{11}^{--} - \rho_{11}^{++} \propto \frac{1}{2}\frac{(\eta + 1)^2}{\eta^2 + 1} - \frac{1}{2}\frac{(\eta - 1)^2}{\eta^2 + 1} = \frac{2\eta}{1 + \eta^2} = P_c\,. \tag{5.7}$$

This quantity is the degree of circular polarization mentioned in section 2.2.3 [43, 44]. We can note that the asymmetry in the ρ_{11}^{mm} populations is proportional to the asymmetry in the electron populations (defined in equation (4.9)), since the muons decay to electrons with the same rate regardless of its state. The proportionality factor is given by the ratio of the muon to electron total populations, up to a factor dependent only on the experimental parameters (except the polarization). Gathering all the proportionalities together, we obtain

$$\mathcal{A}^{\text{Peak}}(\eta) \propto \rho_{11}^{--} - \rho_{11}^{++} \propto \frac{2\eta}{1 + \eta^2}\,, \tag{5.8}$$

and the proportionality factor must the normalization of the curve, which we have established to be $\mathcal{A}^{\text{Peak}}(\eta = 1)$ at the start of the argument.

This curve can now be plotted with the normalized curve of figure 5.9(b), and the LMS between them is in the order of 10^{-7}, depending on the experimental parameters of the normalized $\mathcal{A}^{\text{Peak}}(\eta)$ curve.

Rearranging equation (5.5), the asymmetry at resonance is given by

$$\mathcal{A}^{\text{Peak}}(\eta) = \frac{2\eta}{1 + \eta^2}\mathcal{A}^{\text{Peak}}(\eta = 1)\,, \tag{5.9}$$

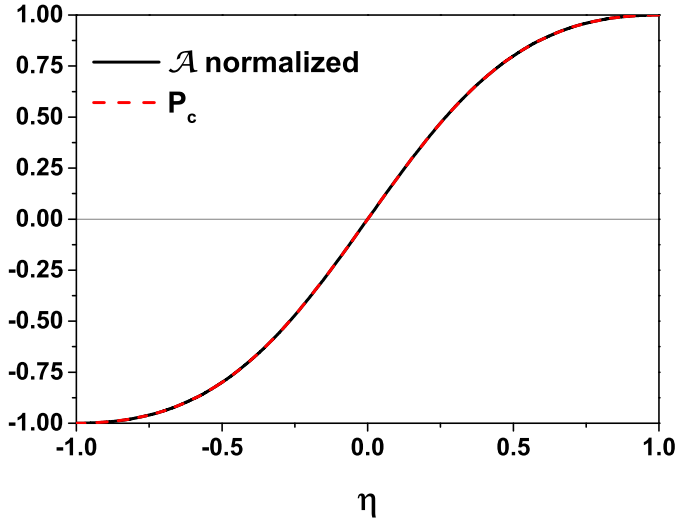

Figure 5.10: asymmetry normalized to $\mathcal{A}^{\text{Peak}}\eta = 1$) (black) with its mathematical curve given by P_c (red).

where the $\mathcal{A}^{\text{Peak}}(\eta = 1)$ are given in appendix H table H.4, and they encapsulate all the experimental parameters (fluence, decay rates and laser bandwidth) dependencies.

The loss in asymmetry can now be computed for every polarization degree as

$$\Delta\mathcal{A} = 1 - \frac{2\eta}{1+\eta^2}. \tag{5.10}$$

Naturally, this expression is in complete agreement with table 5.2. With equation (5.10), the polarization necessary for a certain decrease in asymmetry can be calculated (by inverting the function). The loss in polarization, $\Delta\eta$, corresponding to the loss in asymmetry, $\Delta\mathcal{A}$, would be

$$\Delta\eta = 1 - \frac{1-\sqrt{\Delta\mathcal{A}(2-\Delta\mathcal{A})}}{1-\Delta\mathcal{A}}\,. \tag{5.11}$$

A summary of the polarization loss, $\Delta\eta$, necessary for an asymmetry loss of $\Delta\mathcal{A}$ is shown in table 5.3. In this table, it can be observed that for a defective circular polarized laser,

Table 5.3: Loss in polarization, $\Delta\eta$, relative to right circular polarization, (η= 1), necessary to provoke a loss in asymmetry, $\Delta\mathcal{A}$, also relative to right circular polarization. e.g.: It is necessary a decrease in polarization of 13.2% in order for the asymmetry to lose 1% of its peak value.

$\Delta\mathcal{A}$	1%	2%	5%	10%	25%
$\Delta\eta$	13.2%	18.3%	27.6%	37.3%	54.9%

with actual polarization 30% lower than the supposed η= 1 (i.e. the laser would actually have a polarization of η= 0.7), not even 10% of the maximum asymmetry would be lost (from equation (5.10), it would be only 6%).

The simulations on the asymmetry generated due to the polarization of the laser after a time $\tau = 100$ ns, have shown, as expected, that there is a polarization dependency: if the laser is circularly polarized, the asymmetry will be at its maximum (for that set of experimental parameters), and if it is linear polarized it will be null. Naturally, the asymmetry will be maximum at resonance (again, for that set of parameters). This peak value of the asymmetry was obtain to have its parameters dependencies separated, equation (5.9), i.e. it can be decomposed into a product of two functions: one carries the information of polarization degree ($2\eta/(1+\eta^2)$), and the other carries the information of all the other experimental parameters ($\mathcal{A}^{\text{Peak}}(\eta = 1)$). As such, a shift in polarization will always have the same percentage effect on the asymmetry resonance value, regardless of the others experimental parameters.

5.3 Asymmetry in μ^3He$^+$

In section 4.3, it was explained that a simulation on the μ^3He$^+$ system must account for the possible initial phases of the ground state (which is the $F = 1$ triplet state). To include this, an average over 441 combinations for the initial phases (21 possibilities for φ_{-0} times 21 possibilities for φ_{-+}, and the last phase was calculated like $\varphi_{0+} = \varphi_{-+} - \varphi_{-0}$) was implemented. Due to this average, the computation of a simple solution without Doppler, becomes 441 times slower. If the Doppler effect is included, the computation time for the profile plots would require almost a day worth of runtime for a single set of experimental parameters. The computational time necessary is therefore not feasible for a standard computer, and thus the Doppler was not considered. As such the initial part of the flowchart of figure 5.5 (all the calculations) changes to figure 5.11.

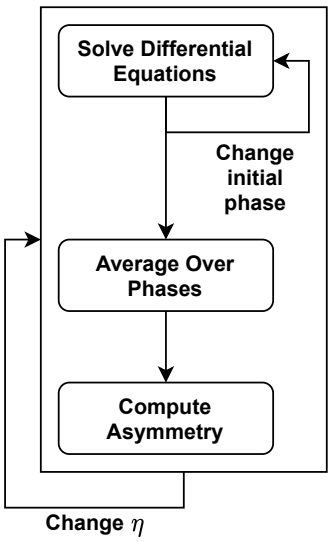

Figure 5.11: Flowchart of the initial steps of the implementation method for the μ^3He$^+$ experiment.

Unlike μH, there are no theoretical calculations for the decay rates of the μ^3He^++He system, moreover there is the possibility of molecule formation which adds another difficulty to the calculation of these rates. In this thesis we are not considering this possibility in the calculation of the statistical weights. Furthermore, the actual values used for the collisional decays are all hypothetical and do not necessarily represent the system. However, they allow to establish the ground work for this upcoming experiment.

In the situation without any decay rates, the population of the atomic states and the electron populations behaves similarly to μH (figure 5.6), with the total muon population following an exponential decay, figure 5.12(a), but starting with the total $F=1$ population at 1 instead of 0. In figure 5.12, only the $\eta=0.5$ case was plotted in order to observe the

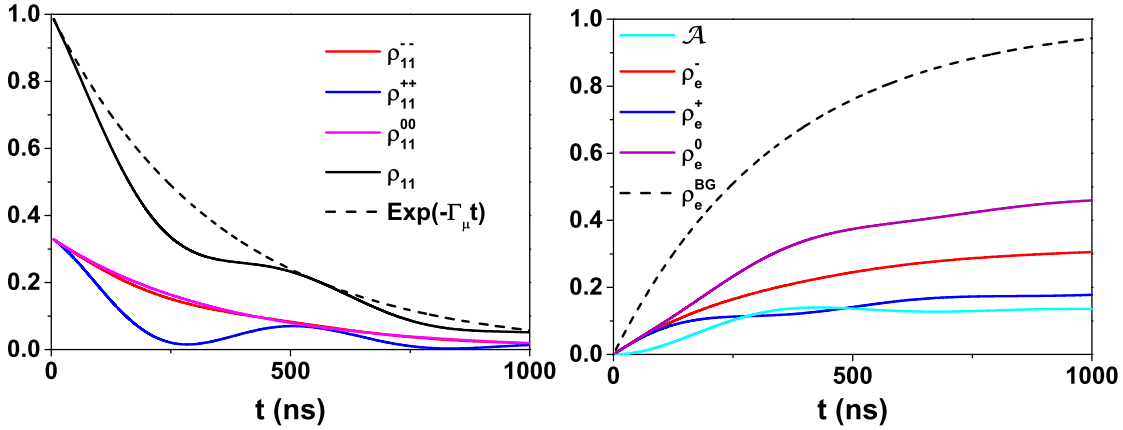

(a) Atomic populations.

(b) Electron populations.

Figure 5.12: Time evolution of the $F=1$ states (a), and electron populations (b), of μ^3He^+ for polarization $\eta=0.5$. The atomic populations in (a) are the $m_F=-1$, 0, 1 (red, magenta and blue lines respectively) and the total $F=1$ population (black line). The exponential decay of the atomic populations is included in (a) (black dashed line). The electron populations in (b) are the ρ_e^- (red), ρ_e^+ (blue) and ρ_e^0 (purple). The asymmetry measure $\mathcal{A}$ is included (cyan line), and the total electron population, ρ_e^{BG} is a negative exponential decay complementing the exponential decay of (a). These results were obtained for $\mathcal{F}=10$ Jcm^{-2}, during $\tau=1000$ ns.

difference in the $m_F=\pm1$ sub-states is observable. The time evolution for other polarizations can be found in appendix I. As in the μH case, the asymmetry is maximum for circular polarization. In μ^3He^+ however, the asymmetry is generated in a two-step process, as explained in section 1.8. The atoms are excited via laser to the $F=0$ upper state, and then they decay via collisional decays and stimulated emission to the triplet ground state. The stimulated emission part is eliminated from the equations due to the rotating wave approximation, remaining only the inelastic collisional decays as a re-populating mechanism for the ground states. The $F=0$ state decays with equal rate for all three ground state sub-levels, meaning that, for example, for right circular polarization, the atoms that exit from the $m_F=1$ sub-level to the $F=0$, are then equally distributed over

the three ground state sub-levels, creating an asymmetry in the sub-levels with $m_F = 1$ and $m_F = -1$.

To evaluate the equations accounting for collisional decays and laser bandwidth, it was considered a laser bandwidth of 100 MHz for the laser, $\Gamma_{\text{in}} = \Gamma_{\text{el}}^{F=0} + \Gamma_{\text{el}}^{F=1}$ and $\Gamma_{\text{el}}^{F=1} = 3\Gamma_{\text{el}}^{F=0}$. These considerations are based on the gross estimate of the relations between the rates for μH given in table 5.1. The following results are then given in terms of the decoherence rate $\Gamma_c = \Gamma_{\text{in}} + \Gamma_{\text{el}}^{F=0} + \Gamma_{\text{el}}^{F=1} + \Gamma_l$.

Plotting now the asymmetry for four different values of Γ_c, and following the conditions described earlier, and considering a laser with fluence of $\mathcal{F} = 10$ Jcm^{-2} during a time $\tau = 100$ ns, we find curves similar to those of figure 5.7 (left figures). From figure 5.13, it

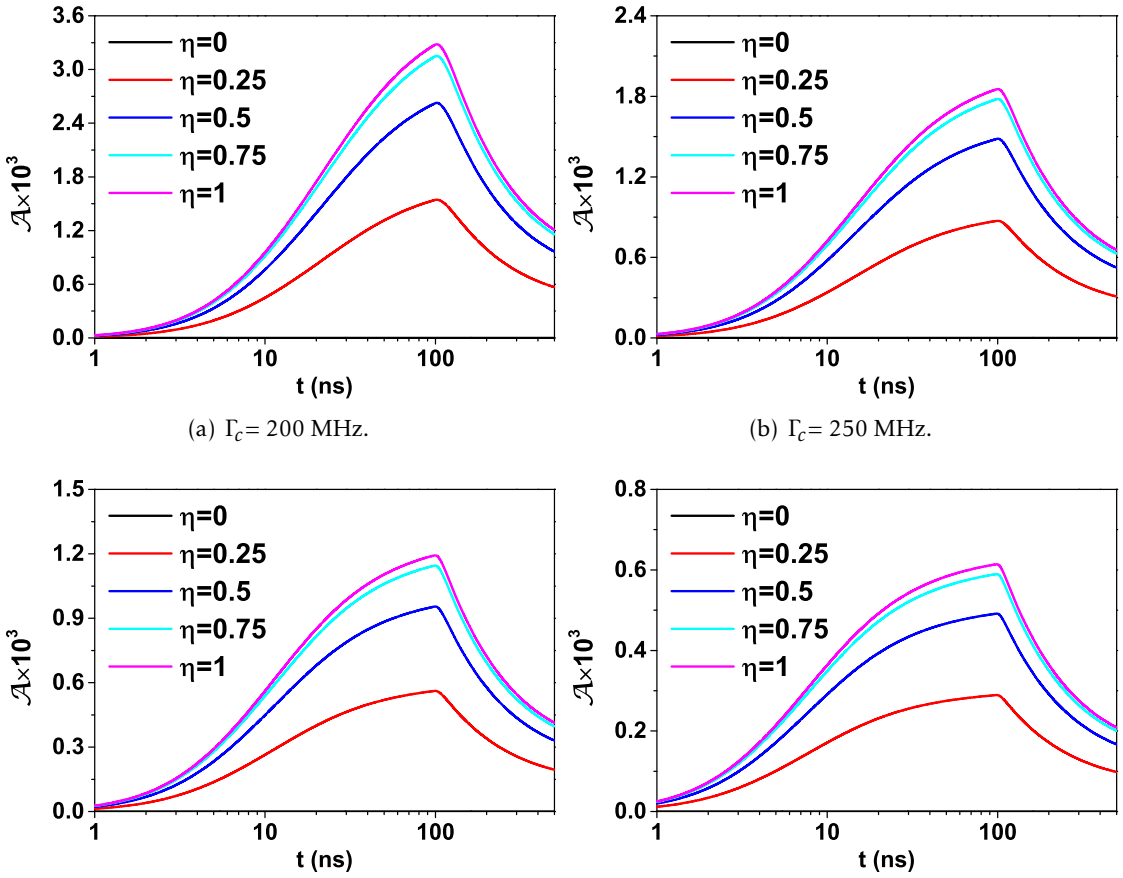

(a) $\Gamma_c = 200$ MHz.

(b) $\Gamma_c = 250$ MHz.

(c) $\Gamma_c = 300$ MHz.

(d) $\Gamma_c = 400$ MHz.

Figure 5.13: Time evolution of the asymmetry in μ^3He$^+$ for different decoherent rates, and various polarization degrees. For every decoherence rate, circular polarization results in the highest value for the polarization. The asymmetry is scaled by a factor of 10^3.

is observed the same result as in μH: circular polarization is obtaining the highest values for the asymmetry. Moreover, it is again observed a high decrease in the asymmetry after the laser is shut off, due the same reasons described in section 5.2.1. As a consequence we will again consider the asymmetry at time τ for the profiles in Δ and η.

For the Δ profile, we obtain a peak at the resonance, as expected and seen in figure 5.14. The shape of the curve in this figure is the same for all decoherence rates, only the case with Γ_c= 200 MHz is shown. The peak values is maximum for a right circular polarization. Contrary to the μH case, the exact value of the peak is not actually relevant, since the values considered for the decay rates only represent an estimate on the proportionality between the rates. On other words, there is no use to compute a database of the peak $\mathcal{A}^{\text{Peak}}$ and FWHM values if we don't actually know the involved decays. We can however

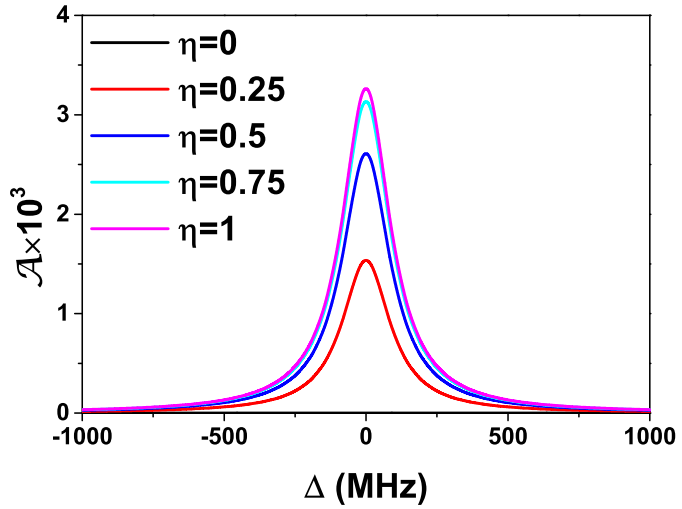

Figure 5.14: Delta profile of the asymmetry of $\mu^3\text{He}^+$, for a decoherence rate of 200 MHz. The asymmetry is scaled by a factor of 10^3.

relate the resonance peak value for right polarization, $\mathcal{A}^{\text{Peak}}(\eta = 1)$, which is the case for maximum asymmetry, with that peak value for other polarizations. This is obtained by studying the η profile plot of the asymmetry at resonance, $\mathcal{A}^{\text{Peak}}(\eta)$.

This curve was obtained for different decoherent rates, resulting in figure 5.15(a), and these curves can be normalized to their maximum value, resulting in the curve of figure 5.15(b) which is the same curve of figure of 5.9(b), and thus is also represented by equation (5.5). The argument to justify that the curve in figure 5.15(b) is given by the degree of circular polarization, P_c, is the very similar to that of section 5.2.1. The difference in the argument is that, since the populations of the F= 1 have an initial population a third each, the solutions (without decays) are of the form

$$\rho_{11}^{mm}(t) = \frac{1}{3} - \frac{1}{3}\frac{\left|\mathcal{V}_{01}^{0m}\right|^2}{|\mathcal{V}_{01}|^2 + \Delta^2}\sin^2\left(\frac{t}{2}\sqrt{|\mathcal{V}_{01}|^2 + \Delta^2}\right), \tag{5.12}$$

and computing the difference gives between ρ_{11}^{--} and ρ_{11}^{++} is proportional the difference in Rabi frequencies squared, which in turn is proportional to the components of the polarization vector of the magnetic field, $\hat{\mathbf{k}} \times \hat{\varepsilon}$ (see appendix D for more details)

$$\mathcal{A}^{\text{Peak}}(\eta) \propto \rho_{11}^{--} - \rho_{11}^{++} \propto -\left|\mathcal{V}_{01}^{0-}\right|^2 + \left|\mathcal{V}_{01}^{0+}\right|^2 \propto -\left|\left(\hat{\mathbf{k}} \times \hat{\varepsilon}\right)_+\right|^2 + \left|\left(\hat{\mathbf{k}} \times \hat{\varepsilon}\right)_-\right|^2$$

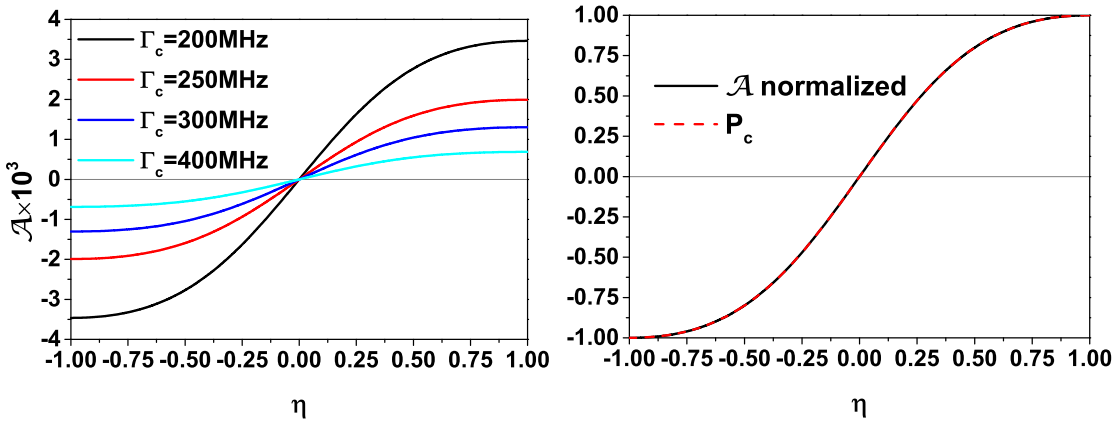

(a) Asymmetry for different decoherence rates.

(b) Asymmetry normalized to $\mathcal{A}^{\text{Peak}}(\eta = 1)$.

Figure 5.15: Eta profile of the asymmetry for different decoherence rates (a), and asymmetry normalized to $\mathcal{A}^{\text{Peak}}(\eta = 1)$ for $\mu^3\text{He}^+$ (b). The degree of circular polarization is also included in figure (b) in dashed red.

$$\mathcal{A}^{\text{Peak}}(\eta) \propto -\frac{1}{2}\frac{(\eta-1)^2}{\eta^2+1} + \frac{1}{2}\frac{(\eta+1)^2}{\eta^2+1} = \frac{2\eta}{\eta^2+1} = P_c\,, \tag{5.13}$$

and here the asymmetry of the electron populations is proportional to the asymmetry of the m_F sub-states by the exponential decay that governs the total population of muons and electrons. Finally, identifying that the curves were normalized with $\mathcal{A}^{\text{Peak}}(\eta = 1)$, equation (5.13) becomes equivalent to (5.9). With this result it is immediate the conclusion that despite the μH and μ^3He$^+$ systems having slightly different sets of equations, the physical treatment to explain them is the same: Both have a maximum asymmetry at resonance and for circular polarization. Furthermore, the loss in asymmetry due to a defective laser, will be the same for both cases, e.g. a laser 30% defective has a polarization degree of η= 0.7 and the loss in asymmetry is 6,04%, given by equation (5.11). In table 5.3 is shown some values for polarization losses, $\Delta\eta$, and their correspondent loss in asymmetry.

6

Conclusion

In the context of the upcoming experiments whose goal is to measure the HFS transition energy of μH (CREMA's-HyperMu and Riken's experiments) and of μ^3He^+ (CREMA's collaboration proposed experiment), there is an extreme importance to optimize all possible parameters due to the low transition probability. Among others, the role of the polarization of the laser must be explored to ensure the highest possible yield of detected events.

To perform this study, the theoretical formalism that describes the interaction of the laser with the atomic system was described accurately with quantum theory, developing the optical Bloch equations. These equations are specific for each experiment and as such three sets of equations had to be developed: 2-levels equations for μH (for the HyperMu experiment); 4-levels equations for μH (for the HyperMu and Riken experiments); 4-levels equations for μ^3He^+ (for the CREMA's proposed experiment). The equations had to be altered to include the various decays of the system (elastic and inelastic collisional decays), and to include the laser bandwidth and the Doppler effect due to the movement of the atoms. Furthermore, populations of particles that do not actually interact with the Bloch populations (dark state, and electron populations) were included with phenomenological arguments.

The developed equations were implemented and solved numerically in *Wolfram Mathematica 9.0*. The simulations for the HyperMu experiment shown no dependence on the polarization. For this experiment, only the 4-levels equations can include the laser polarization explicitly. In the 2-levels equations the dependence on the polarization disappears while calculating the Rabi frequency (due to a summation over the components of the polarization vector). The conclusion here is that if the polarization does not play a role for this experiment, then all the simulations for different polarizations with the 4-levels equations must yield the same results. Moreover, they must yield the same result as the 2-levels equations (which do not separate degenerate states). Simulations on the time evolution the excited $F=1$ state were presented in section 5.1, where it was observed that this population (the total excited state), stays the same (for a fixed set of parameters) regardless of the polarization, which is also equal the 2-levels solution. The polarization

parameter, η, controls which of the sub-states is more populated, but maintaining the same total excited $F=1$ state. Simulations on the dark state and ρ_{11} for different sets of decay rates, always resulted in essentially identical solutions within the 4-levels case and with the 2-levels case. For the time evolution of these populations, the maximum LMS error relative to the 2-levels case was in the order of 10^{-3} for ρ_{DS} and 10^{-5} to the ρ_{11} state. For the profile curve of the dark state, the highest LMS error was in the order of 10^{-2}. Not only are these LMS errors quite small, they can also be explained by the numerical solve of the differential equations, due to the pattern in which they are highest: low decay rates and higher fluences, the situations where the solutions change more.

Due to these minor numerical errors, it can be concluded that the polarization does not play any role in the diffusion experiment, or at least not numerically. This conclusion can be explained by the fact that the dark state does not distinguish wish population is decaying to it, and since they all decay with the same rate, the dark state just sees the sum of the sub-levels has only one level (i.e. the degenerate $F=1$ level).

The asymmetry experiments was also treated here, and their simulations follows similar results. Both asymmetry experiments' first and second results comes directly from theory: The muon populations decreases exponentially, and the electron population compensates increasing its total population, such that the total population of all levels (and particles) in the system stays at unitary. The second result is that for circular polarization the asymmetry measure will always be greater. This is because for circular polarization the laser only induces transitions to one of the sub-levels of the $F=1$ state.

When at resonance, it was found that the asymmetry polarization dependence is independent of the rest of the experimental parameters. This means that the asymmetry can be written as a product of the polarization part, which will be the degree of circular polarization P_c, with another part that encapsulates all the other experimental parameters. This other part can be identified to be the asymmetry at resonance and for right circular polarization. The dependency on P_c can be explained by the proportionality between the populations, their respective Rabi frequencies, and the component of the polarization vector associated with the Rabi frequencies. With this simple relation, the asymmetry for any polarization can be found by consulting the table H.4 of peak values for circular polarization, and multiplying by the appropriate P_c.

Commenting now on the role of polarization for the asymmetry experiments, it can be calculated with the degree of circular polarization that, for the asymmetry to lose 1% of its value (relative to the circular polarization), the laser must have at least a polarization mixture of 13.2% linear and 86.8% circular ($\eta=0.868$). On a reverse argument, a 13.2% mixed-polarization laser (relative to circular polarization) only causes a 1% loss in the asymmetry. Even going as far as a 30% mixed-polarization laser, only 6% of the asymmetry will be lost due to this.

From a practical point of view, even if the laser being used has some mixed-polarization, it most likely will not reach degree of linear polarization values enough for the experiment to be compromised.

Some extra theoretical caveats of the calculation regarding the $\mu^3\mathrm{He}^+$ experiment were observed:

- The possibility of formation of molecules may alter the symmetry of the equations. Regarding the plus and minus indices, it was stated in chapter 5 that one can change all the indices and the set of equations would be the same. In reality, this is only true if the statistical weights are symmetric, $W_{mm'} = W_{-m-m'}$. Adding other types of interactions may disrupt this symmetry;

- Constructing tables of $\mathcal{A}^{\mathrm{Peak}}(\eta = 1)$, at this moment, is not practical, since currently there are no calculated collisional rates for this system.

- The computation time for $\mu^3\mathrm{He}^+$ is currently long. The implemented code was not originally devised with the goal of solving computationally heavy systems, it was only adapted to solve the $\mu^3\mathrm{He}^+$ Bloch equations. The main issue is not solving the equations themselves but the iterative process associated with the convolution and the average over the initial phases.

Nevertheless, the implementation allowed to understand that the $\mu^3\mathrm{He}^+$ asymmetry system may behave like the μH asymmetry system, and to establish some groundwork on the simulation for this experiment.

Some continuation for this work involves optimization of the simulation time for the $\mu^3\mathrm{He}^+$ experiment, which can be resolved by using *python* numerical libraries instead of *Wolfram Mathematica* to run the simulations.

Bibliography

[1] E. Hecht. *Optics, Global Edition*. fifth ed. Pearson Education Limited, 2017. ISBN: 9781292096933. URL: https://search.ebscohost.com/login.aspx?direct=true%7B%5C&%7Ddb=edsebk%7B%5C&%7DAN=1419863%7B%5C&%7Dsite=eds-live (cit. on pp. 1, 17, 18, 20).

[2] W. Demtröder. "Laser Spectroscopy". In: (Dec. 1996). ISSN: 1098-6596. URL: http://link.springer.com/10.1007/978-3-662-08260-7 (cit. on p. 1).

[3] P. Campbell, I. D. Moore, and M. R. Pearson. *Laser spectroscopy for nuclear structure physics*. Vol. 86. Elsevier, Jan. 2016, pp. 127–180. DOI: 10.1016/j.ppnp.2015.09.003 (cit. on p. 1).

[4] J. Biesheuvel et al. "Probing QED and fundamental constants through laser spectroscopy of vibrational transitions in HD+". In: *Nature Communications* 7.1 (Apr. 2016), p. 10385. ISSN: 2041-1723. DOI: 10.1038/ncomms10385. URL: http://www.nature.com/articles/ncomms10385 (cit. on p. 1).

[5] S. Alighanbari et al. "Precise test of quantum electrodynamics and determination of fundamental constants with HD+ ions". In: *Nature* 581.7807 (May 2020), pp. 152–158. ISSN: 0028-0836. DOI: 10.1038/s41586-020-2261-5. URL: http://www.nature.com/articles/s41586-020-2261-5 (cit. on pp. 1, 31).

[6] C. J. Bordé. "Base units of the SI, fundamental constants and modern quantum physics". In: *Philosophical Transactions of the Royal Society A: Mathematical, Physical and Engineering Sciences* 363.1834 (Sept. 2005), pp. 2177–2201. ISSN: 1364-503X. DOI: 10.1098/rsta.2005.1635. URL: https://royalsocietypublishing.org/doi/10.1098/rsta.2005.1635 (cit. on p. 1).

[7] W. Demtröder. *Atoms, Molecules and Photons*. Berlin/Heidelberg: Springer-Verlag, 2006, pp. 1–571. ISBN: 3-540-20631-0. DOI: 10.1007/3-540-32346-5. URL: http://link.springer.com/10.1007/3-540-32346-5 (cit. on p. 1).

[8] D. F. Winters et al. "Laser spectroscopy of hyperfine structure in highly charged ions: a test of QED at high fields". In: *Canadian Journal of Physics* 85.5 (May 2007), pp. 403–408. ISSN: 0008-4204. DOI: 10.1139/p07-023. URL: https://cdnsciencepub.com/doi/abs/10.1139/p07-023 (cit. on p. 1).

[9] A. Antognini. "The Lamb Shift Experiment in Muonic Hydrogen". Dec. 2005. URL: http://nbn-resolving.de/urn:nbn:de:bvb:19-50441 (cit. on pp. 1, 3, 4, 7).

[10] A. Antognini. "Muonic Atoms and the Nuclear Structure". In: *Laser Spectroscopy*. WORLD SCIENTIFIC, Dec. 2016, pp. 17–29. ISBN: 978-981-320-060-9. DOI: 10.1142/9789813200616_0002. arXiv: 1512.01765. URL: http://www.worldscientific.com/doi/abs/10.1142/9789813200616%7B%5C_%7D0002 (cit. on pp. 1–3, 5, 7).

[11] R. Pohl et al. "The size of the proton". In: *Nature* 466.7303 (June 2010), pp. 213–216. ISSN: 0028-0836. DOI: 10.1038/nature09250. URL: http://www.nature.com/articles/nature09250 (cit. on pp. 1–4).

[12] A. Antognini et al. "Proton Structure from the Measurement of 2S-2P Transition Frequencies of Muonic Hydrogen". In: *Science* 339.6118 (Jan. 2013), pp. 417–420. ISSN: 0036-8075. DOI: 10.1126/science.1230016. URL: https://www.science.org/doi/10.1126/science.1230016 (cit. on pp. 1–4, 7, 8).

[13] A. Antognini et al. "Theory of the 2S–2P Lamb shift and 2S hyperfine splitting in muonic hydrogen". In: *Annals of Physics* 331 (Apr. 2013), pp. 127–145. ISSN: 00034916. DOI: 10.1016/j.aop.2012.12.003. arXiv: 1208.2637. URL: http://dx.doi.org/10.1016/j.aop.2012.12.003 (cit. on pp. 1, 2, 7).

[14] J. J. Krauth et al. "Measuring the α-particle charge radius with muonic helium-4 ions". In: *Nature* 589.7843 (Jan. 2021), pp. 527–531. ISSN: 0028-0836. DOI: 10.1038/s41586-021-03183-1. URL: https://www.nature.com/articles/s41586-021-03183-1 (cit. on p. 1).

[15] P. J. Mohr, B. N. Taylor, and D. B. Newell. "CODATA Recommended Values of the Fundamental Physical Constants: 2010". In: *Journal of Physical and Chemical Reference Data* 41.4 (Dec. 2012), p. 043109. ISSN: 0047-2689. DOI: 10.1063/1.4724320. URL: http://aip.scitation.org/doi/10.1063/1.4724320 (cit. on p. 1).

[16] J. C. Bernauer. "The proton radius puzzle – 9 years later". In: *EPJ Web of Conferences* 234 (Apr. 2020). Ed. by G. D'Ambrosio et al., p. 01001. ISSN: 2100-014X. DOI: 10.1051/epjconf/202023401001. URL: https://www.epj-conferences.org/10.1051/epjconf/202023401001 (cit. on p. 1).

[17] H. Gao and M. Vanderhaeghen. "The proton charge radius". In: (May 2021). ISSN: 0042-1294. arXiv: 2105.00571. URL: http://arxiv.org/abs/2105.00571 (cit. on p. 2).

[18] P. J. Mohr, D. B. Newell, and B. N. Taylor. "CODATA Recommended Values of the Fundamental Physical Constants: 2014". In: *Reviews of Modern Physics* 88.3 (July 2015), p. 035009. ISSN: 0034-6861. DOI: 10.1103/RevModPhys.88.035009. arXiv: 1507.07956. URL: https://link.aps.org/doi/10.1103/RevModPhys.88.035009 (cit. on p. 2).

[19] E. Tiesinga et al. "CODATA Recommended Values of the Fundamental Physical Constants: 2018". In: *Journal of Physical and Chemical Reference Data* 50.3 (Sept. 2021), p. 033105. ISSN: 0047-2689. DOI: 10.1063/5.0064853. URL: https://aip.scitation.org/doi/10.1063/5.0064853 (cit. on p. 2).

[20] A. V. Volotka et al. "Zemach and magnetic radius of the proton from the hyperfine splitting in hydrogen". In: *The European Physical Journal D* 33.1 (Apr. 2005), pp. 23–27. ISSN: 1434-6060. DOI: 10.1140/epjd/e2005-00025-9. URL: https://link.springer.com/article/10.1140/epjd/e2005-00025-9 (cit. on pp. 2, 7).

[21] A. Dupays et al. "Proton Zemach radius from measurements of the hyperfine splitting of hydrogen and muonic hydrogen". In: *Physical Review A* 68.5 (Nov. 2003), p. 052503. ISSN: 1050-2947. DOI: 10.1103/PhysRevA.68.052503. URL: https://journals.aps.org/pra/abstract/10.1103/PhysRevA.68.052503 (cit. on pp. 2, 7).

[22] J. Friar and I. Sick. "Zemach moments for hydrogen and deuterium". In: *Physics Letters B* 579.3-4 (Jan. 2004), pp. 285–289. ISSN: 03702693. DOI: 10.1016/j.physletb.2003.11.018. URL: https://linkinghub.elsevier.com/retrieve/pii/S0370269303017416 (cit. on p. 2).

[23] M. O. Distler, J. C. Bernauer, and T. Walcher. "The RMS charge radius of the proton and Zemach moments". In: *Physics Letters B* 696.4 (Feb. 2011), pp. 343–347. ISSN: 03702693. DOI: 10.1016/j.physletb.2010.12.067. URL: https://linkinghub.elsevier.com/retrieve/pii/S0370269311000050 (cit. on p. 2).

[24] T. Albahri et al. "Measurement of the anomalous precession frequency of the muon in the Fermilab Muon g-2 experiment". In: *Physical Review D* 103.7 (Apr. 2021), p. 072002. ISSN: 2470-0010. DOI: 10.1103/PhysRevD.103.072002. arXiv: 2104.03247. URL: https://journals.aps.org/prd/abstract/10.1103/PhysRevD.103.072002 (cit. on p. 2).

[25] A. Antognini. *Measurement of the hyperfine splitting in muonic hydrogen and laser technologies*. URL: https://www.psi.ch/en/ltp/hypermu (visited on 11/30/2021) (cit. on pp. 2, 8).

[26] M. Bonesini. "The FAMU experiment at RIKEN RAL for a precise measure of the proton radius". In: *Proceedings of European Physical Society Conference on High Energy Physics — PoS(EPS-HEP2019)* 364 (Oct. 2020), p. 132. ISSN: 18248039. DOI: 10.22323/1.364.0132. arXiv: 2010.01398. URL: https://pos.sissa.it/364/132 (cit. on pp. 2, 3).

[27] Y. Ma et al. "New Precision Measurement for Proton Zemach Radius with Laser Spectroscopy". In: *International Journal of Modern Physics: Conference Series* 40 (Jan. 2016), p. 1660046. ISSN: 2010-1945. DOI: 10.1142/S2010194516600466. URL: https://www.worldscientific.com/doi/abs/10.1142/S2010194516600466 (cit. on pp. 2–4, 11).

[28] S. Kanda et al. "Measurement of the proton Zemach radius from the hyperfine splitting in muonic hydrogen atom". In: *Journal of Physics: Conference Series* 1138.1 (Nov. 2018), p. 012009. ISSN: 1742-6588. DOI: 10.1088/1742-6596/1138/1/012009. URL: https://iopscience.iop.org/article/10.1088/1742-6596/1138/1/012009 (cit. on pp. 2, 3, 9–11, 34).

[29] S. Schmidt et al. "The next generation of laser spectroscopy experiments using light muonic atoms". In: *Journal of Physics: Conference Series* 1138.1 (Nov. 2018), p. 012010. ISSN: 1742-6588. DOI: 10.1088/1742-6596/1138/1/012010. arXiv: 1808.07240. URL: https://iopscience.iop.org/article/10.1088/1742-6596/1138/1/012010 (cit. on pp. 3, 4, 7–9, 11, 12, 39, 52).

[30] R. Pohl et al. "Muonic Hydrogen and the Proton Radius Puzzle". In: *Annual Review of Nuclear and Particle Science* 63.1 (Oct. 2013), pp. 175–204. ISSN: 0163-8998. DOI: 10.1146/annurev-nucl-102212-170627. arXiv: 1301.0905. URL: https://www.annualreviews.org/doi/10.1146/annurev-nucl-102212-170627 (cit. on p. 3).

[31] K. Jungmann. "Laser spectroscopy of muonic atoms". In: *Zeitschrift für Physik C Particles and Fields* 56.S1 (Mar. 1992), S59–S69. ISSN: 0170-9739. DOI: 10.1007/BF02426776. URL: http://link.springer.com/10.1007/BF02426776 (cit. on p. 3).

[32] R. Pohl et al. "Observation of Long-Lived Muonic Hydrogen in the <math display="inline"> <mn>2</mn> <mi>S</mi> </math> State". In: *Physical Review Letters* 97.19 (Nov. 2006), p. 193402. ISSN: 0031-9007. DOI: 10.1103/PhysRevLett.97.193402. URL: https://link.aps.org/doi/10.1103/PhysRevLett.97.193402 (cit. on p. 3).

[33] A. Antognini. "The 2S Lamb shift in muonic hydrogen and the proton rms charge radius". In: *AIP Conference Proceedings*. Vol. 796. 2005. AIP, 2005, pp. 253–259. ISBN: 0735402841. DOI: 10.1063/1.2130175. URL: http://aip.scitation.org/doi/abs/10.1063/1.2130175 (cit. on p. 4).

[34] A. Antognini et al. "Experiments towards resolving the proton charge radius puzzle". In: *EPJ Web of Conferences* 113 (Sept. 2015). Ed. by C. Elster, D. Phillips, and C. Roberts, p. 01006. ISSN: 2100-014X. DOI: 10.1051/epjconf/20161131006. arXiv: 1509.03235. URL: http://www.epj-conferences.org/10.1051/epjconf/201611301006 (cit. on pp. 7, 8).

[35] R. G. Sachs. "High-Energy Behavior of Nucleon Electromagnetic Form Factors". In: *Physical Review* 126.6 (June 1962), pp. 2256–2260. ISSN: 0031-899X. DOI: 10.1103/PhysRev.126.2256. URL: https://link.aps.org/doi/10.1103/PhysRev.126.2256 (cit. on p. 7).

[36] F. Hagelstein, R. Miskimen, and V. Pascalutsa. "Nucleon Polarizabilities: from Compton Scattering to Hydrogen Atom". In: *Progress in Particle and Nuclear Physics* 88 (Dec. 2015), pp. 29–97. ISSN: 01466410. DOI: 10.1016/j.ppnp.2015.12.001. arXiv: 1512.03765. URL: https://linkinghub.elsevier.com/retrieve/pii/S0146641015001118 (cit. on p. 7).

[37] J. S. Cohen. "Improved adiabatic calculation of muonic-hydrogen-atom cross sections. II. Hyperfine transitions and elastic scattering in symmetric collisions". In: *Physical Review A* 43.9 (May 1991), pp. 4668–4683. ISSN: 1050-2947. DOI: 10.1103/PhysRevA.43.4668. URL: https://link.aps.org/doi/10.1103/PhysRevA.43.4668 (cit. on p. 8).

[38] D. J. Abbott et al. "Diffusion of muonic deuterium and hydrogen atoms". In: *Physical Review A* 55.1 (Jan. 1997), pp. 214–229. ISSN: 1050-2947. DOI: 10.1103/PhysRevA.55.214. URL: https://link.aps.org/doi/10.1103/PhysRevA.55.214 (cit. on p. 8).

[39] D. J. Griffiths. *Introduction to Electrodynamics*. forth ed. Pearson Education, Dec. 2015. ISBN: 978-0-321-85656-2 (cit. on pp. 13, 15, 16, 25, 30).

[40] M. E. Rose. *Elementary theory of angular momentum*. Reprint. Courier Corporation, 1995. ISBN: 0-486-68480-6 (cit. on pp. 15, 87).

[41] W. R. Johnson. *Atomic Structure Theory*. Berlin, Heidelberg: Springer Berlin Heidelberg, 2007, pp. 1–312. ISBN: 978-3-540-68010-9. DOI: 10.1007/978-3-540-68013-0. URL: http://link.springer.com/10.1007/978-3-540-68013-0 (cit. on pp. 15, 24, 25, 28, 31).

[42] W. Greiner. *Quantum Mechanics*. forth ed. Berlin, Heidelberg: Springer Berlin Heidelberg, Feb. 2011. ISBN: 978-3-540-67458-0. DOI: 10.1007/978-3-642-56826-8. URL: http://link.springer.com/10.1007/978-3-642-56826-8 (cit. on pp. 16, 30).

[43] P. Amaro et al. "Quantum interference shifts in laser spectroscopy with elliptical polarization". In: *Physical Review A* 92.6 (Dec. 2015), p. 062506. ISSN: 1050-2947. DOI: 10.1103/PhysRevA.92.062506. URL: https://link.aps.org/doi/10.1103/PhysRevA.92.062506 (cit. on pp. 21, 67).

[44] A. Y. Istomin et al. "Elliptic and Circular Dichroism Effects in Two-Photon Double Ionization of Atoms". In: *Physical Review Letters* 97.12 (Sept. 2006), p. 123002. ISSN: 0031-9007. DOI: 10.1103/PhysRevLett.97.123002. URL: https://link.aps.org/doi/10.1103/PhysRevLett.97.123002 (cit. on pp. 21, 67).

[45] Y. Ralchenko. *Atomic Spectroscopy - Spectral Lines*. 2018. URL: https://www.nist.gov/pml/atomic-spectroscopy-compendium-basic-ideas-notation-data-and-formulas/atomic-spectroscopy (visited on 11/17/2021) (cit. on p. 29).

[46] R. Loudon. "Quantum mechanics of the atom-radiation interaction". In: *The Quantum Theory of Light*. Third ed. Oxford, United Kingdom: Oxford University Press, Dec. 2000, pp. 46–81. ISBN: 0198501765 (cit. on pp. 30, 33, 40, 66, 89, 93).

[47] P. Amaro et al. "Laser excitation of the 1s-hyperfine transition in muonic hydrogen". In: *in preparation* (Nov. 2021), pp. 1–13. arXiv: 2112.00138. URL: http://arxiv.org/abs/2112.00138 (cit. on pp. 34, 37, 52, 54, 66, 96).

[48] D. Manzano. "A short introduction to the Lindblad master equation". In: *AIP Advances* 10.2 (Feb. 2020), p. 025106. ISSN: 2158-3226. DOI: 10.1063/1.5115323. arXiv: 1906.04478. URL: http://aip.scitation.org/doi/10.1063/1.5115323 (cit. on pp. 40, 41).

[49] J. Dubois, U. Saalmann, and J. M. Rost. "Semi-classical Lindblad master equation for spin dynamics". In: *Journal of Physics A: Mathematical and Theoretical* 54.23 (June 2021), p. 235201. ISSN: 1751-8113. DOI: 10.1088/1751-8121/abf79b. URL: https://iopscience.iop.org/article/10.1088/1751-8121/abf79b (cit. on p. 41).

[50] P. W. Courteille. *Atom-Light Interaction and Basic Applications*. 2019. URL: https://www.ifsc.usp.br/%7B~%7Dstrontium/Publication/Scripts/LightAtomsLecture.pdf (cit. on pp. 41, 93).

[51] M. J. McDonnell, D. N. Stacey, and A. M. Steane. "Laser linewidth effects in quantum state discrimination by electromagnetically induced transparency". In: *Physical Review A* 70.5 (Nov. 2004), p. 053802. ISSN: 1050-2947. DOI: 10.1103/PhysRevA.70.053802. URL: https://link.aps.org/doi/10.1103/PhysRevA.70.053802 (cit. on p. 42).

[52] A. Adamczak. "Differential cross sections for muonic atom scattering from hydrogenic molecules". In: *Physical Review A* 74.4 (Oct. 2006), p. 042718. ISSN: 1050-2947. DOI: 10.1103/PhysRevA.74.042718. URL: https://link.aps.org/doi/10.1103/PhysRevA.74.042718 (cit. on pp. 44, 54, 99).

[53] C. Pizzolotto et al. "The FAMU experiment: muonic hydrogen high precision spectroscopy studies". In: *European Physical Journal A* 56.7 (July 2020), pp. 1–15. ISSN: 1434601X. DOI: 10.1140/epja/s10050-020-00195-9. URL: https://link.springer.com/article/10.1140/epja/s10050-020-00195-9 (cit. on p. 48).

[54] F. Bert. "Local probes of magnetism, NMR and μ SR: A short introduction". In: *École thématique de la Société Française de la Neutronique* 13 (Apr. 2014). Ed. by V. Simonet et al., p. 03001. ISSN: 2107-7223. DOI: 10.1051/sfn/20141303001. URL: http://www.neutron-sciences.org/10.1051/sfn/20141303001 (cit. on p. 50).

[55] M. Ferro. "Modeling and Optimization of Laser Spectroscopy of Hyperfine Ground State in Muonic Hydrogen". 2021 (cit. on p. 53).

[56] A. Adamczak et al. "Atlas of Cross Sections for Scattering of Muonic Hydrogen Atoms on Hydrogen Isotope Molecules". In: *Atomic Data and Nuclear Data Tables* 62.2 (Mar. 1996), pp. 255–344. ISSN: 0092640X. DOI: 10.1006/adnd.1996.0006. URL: https://linkinghub.elsevier.com/retrieve/pii/S0092640X96900066 (cit. on p. 54).

[57] V. Devanathan. *Angular Momentum Techniques in Quantum Mechanics*. New York, 2002. URL: https://search.ebscohost.com/login.aspx?direct=true%7B%5C&%7Ddb=edsebk%7B%5C&%7DAN=68263%7B%5C&%7Dsite=eds-live (cit. on p. 87).

[58] W. J. Thompson. *Angular Momentum : An Illustrated Guide to Rotational Symmetries for Physical Systems*. English. Weinheim: Wiley-VCH, 2004. ISBN: 9780471552642 (cit. on p. 87).

A

Spherical Basis and Matrix Elements

A.1 Spherical Basis

In atomic physics, the use of the spherical basis instead of the more usual cartesian or spherical coordinates is quite common, as it is very powerful in computing matrix elements. The contents of this appendix can be found in [40, 57, 58].

The spherical basis is defined with the following set of unit vectors:

$$\hat{\mathbf{e}}_- = \frac{1}{\sqrt{2}}\left(\hat{\mathbf{e}}_x - \mathrm{i}\,\hat{\mathbf{e}}_y\right), \qquad \hat{\mathbf{e}}_0 = \hat{\mathbf{e}}_z\,, \qquad \hat{\mathbf{e}}_+ = \frac{-1}{\sqrt{2}}\left(\hat{\mathbf{e}}_x + \mathrm{i}\,\hat{\mathbf{e}}_y\right) \tag{A.1}$$

their dot product is $\hat{\mathbf{e}}_\mu \cdot \hat{\mathbf{e}}_\nu = \delta_{\mu\nu}$, and the cross product $\hat{\mathbf{e}}_0 \times \hat{\mathbf{e}}_\pm = \mp \mathrm{i}\,\hat{\mathbf{e}}_\pm$ and $\hat{\mathbf{e}}_\pm \times \hat{\mathbf{e}}_\mp = \pm \mathrm{i}\,\hat{\mathbf{e}}_0$

A vector, $\vec{\mathbf{A}}$, can be written in this basis like

$$\vec{\mathbf{A}} = A_-\hat{\mathbf{e}}_- + A_0\hat{\mathbf{e}}_0 + A_+\hat{\mathbf{e}}_+ = \sum_\lambda A_\lambda \hat{\mathbf{e}}_\lambda\,, \tag{A.2}$$

and if $\vec{\mathbf{A}}$ is Hermitian, then $A_\lambda^\dagger = (-1)^\lambda A_{-\lambda}$ (or $A_\lambda^* = (-1)^\lambda A_{-\lambda}$ if $\vec{\mathbf{A}}$ is not a matrix).

The dot product between two vectors $\vec{\mathbf{A}}$ and $\vec{\mathbf{B}}$ can be defined as

$$\vec{\mathbf{A}} \cdot \vec{\mathbf{B}} = \sum_{\lambda=-1}^{1} A_\lambda^\dagger B_\lambda\,. \tag{A.3}$$

A.2 Wigner-Eckart Theorem

Using the spherical basis, the Wigner-Eckart theorem (A.4) states that a matrix element of the q component of the rank k tensor operator $\vec{\mathbf{T}}^k$ in the basis of angular momentum eigenstates $|jm\rangle$ is always proportional to a quantity, the reduced matrix element $\left\langle j' \middle\| T^k \middle\| j \right\rangle$ which is independent of the orientation of the angular momentum. The proportionality coefficient is the Wigner 3J-symbol.

$$\left\langle j'm' \middle| T_q^k \middle| jm \right\rangle = (-1)^{j'-m'} \begin{pmatrix} j' & k & j \\ -m' & q & m \end{pmatrix} \left\langle j' \middle\| T^k \middle\| j \right\rangle \tag{A.4}$$

With the definition of the dot product (A.3) and the Wigner-Eckart theorem (A.4), the matrix element for an tensor operator $\vec{\mathbf{T}}^k \cdot \vec{\epsilon}$ is

$$\begin{aligned}
\left\langle j'm' \middle| \vec{\mathbf{T}}^k \cdot \vec{\epsilon} \middle| jm \right\rangle &= \sum_\lambda \left\langle j'm' \middle| T_\lambda^{k\dagger} \middle| jm \right\rangle \epsilon_\lambda \\
&= \sum_\lambda (-1)^\lambda \left\langle j'm' \middle| T_{-\lambda}^k \middle| jm \right\rangle \epsilon_\lambda \\
&= (-1)^{j'-m'} \left\langle j' \middle\| T^k \middle\| j \right\rangle \sum_\lambda (-1)^\lambda \begin{pmatrix} j' & k & j \\ -m' & -\lambda & m \end{pmatrix} \epsilon_\lambda
\end{aligned} \tag{A.5}$$

where $\vec{\epsilon}$ does not act on the $|jm\rangle$ states and $\vec{\mathbf{T}}^k$ is Hermitic.

A.3 Matrix Elements

Applying the Wigner-Eckart theorem to the tensor J_0 of rank 1, the $q = 0$ component of the rank 1 tensor $\vec{\mathbf{J}}$, with eigenstates $|jm\rangle$, allows to obtain the reduced matrix element $\langle j' \| J \| j \rangle$. The matrix element $\langle j'm' | J_0 | jm \rangle = m\hbar\delta_{m'm}\delta_{j'j}$ forces $m' = m$ and $j' = j$, considering this in the Wigner-Eckart theorem gives a simplified expression for the 3J-symbol.

$$\begin{aligned}
\left\langle j'm' \middle| J_0 \middle| jm \right\rangle = m\hbar\delta_{m'm}\delta_{j'j} &= (-1)^{j-m} \begin{pmatrix} j & 1 & j \\ -m & 0 & m \end{pmatrix} \langle j' \| J \| j \rangle \\
m\hbar\delta_{m'm}\delta_{j'j} &= (-1)^{j-m} \frac{(-1)^{m-j} m}{\sqrt{j(j+1)(2j+1)}} \langle j' \| J \| j \rangle \\
\langle j' \| J \| j \rangle &\implies \hbar\sqrt{j(j+1)(2j+1)}\delta_{j'j}
\end{aligned} \tag{A.6}$$

If the states in the matrix element are eigenstates of two coupled angular momenta, $\vec{\mathbf{J}} = \vec{\mathbf{J}}_1 + \vec{\mathbf{J}}_2$ (with states $|j_1 j_2 jm\rangle$) then the reduced matrix elements of J_1 and J_2 are calculated with equations

$$\langle j' \| J_1 \| j \rangle = \sqrt{2j'+1}\sqrt{2j+1}(-1)^{j_1'+j_2+j+1} \begin{Bmatrix} j' & 1 & j \\ j_1 & j_2 & j_1' \end{Bmatrix} \langle j_1' \| J_1 \| j_1 \rangle \tag{A.7}$$

$$\langle j' \| J_2 \| j \rangle = \sqrt{2j'+1}\sqrt{2j+1}(-1)^{2j+j'-j_1-j_2+1} \begin{Bmatrix} j' & 1 & j \\ j_2 & j_1 & j_2' \end{Bmatrix} \langle j_2' \| J_2 \| j_2 \rangle \tag{A.8}$$

B

Derivation of the Bloch Equations

In this appendix, the Bloch equations are derived for the 2-levels μH, 4-levels μH and 4-levels $\mu^3\mathrm{He}^+$ systems, according to equation (3.2). Along this appendix the rotating wave approximation will be used several times, see appendix C.

B.1 2-levels μH

Computing the ρ_{00} case (population of the degenerate level) gives

$$\begin{aligned}
\frac{\partial\rho_{00}(t)}{\partial t} &= \sum_k \frac{\mathrm{i}}{2}\rho_{0k}(t)\,\mathrm{e}^{-\mathrm{i}\omega_{0k}t}\left(\mathcal{V}^*_{0k}\,\mathrm{e}^{\mathrm{i}\omega t}+\mathcal{V}_{k0}\,\mathrm{e}^{-\mathrm{i}\omega t}\right)+\text{c.c.}\\
&= \frac{\mathrm{i}}{2}\rho_{00}\left(\mathcal{V}^*_{00}\,\mathrm{e}^{\mathrm{i}\omega t}+\mathcal{V}_{00}\,\mathrm{e}^{-\mathrm{i}\omega t}\right)-\frac{\mathrm{i}}{2}\rho_{00}\left(\mathcal{V}_{00}\,\mathrm{e}^{-\mathrm{i}\omega t}+\mathcal{V}^*_{00}\,\mathrm{e}^{\mathrm{i}\omega t}\right)\\
&\quad+\left(\frac{\mathrm{i}}{2}\rho_{01}\,\mathrm{e}^{\mathrm{i}\omega_r t}\left(\mathcal{V}^*_{01}\,\mathrm{e}^{\mathrm{i}\omega t}+\mathcal{V}_{10}\,\mathrm{e}^{-\mathrm{i}\omega t}\right)+\text{c.c.}\right)\\
\frac{\partial\rho_{00}(t)}{\partial t} &\approx \frac{\mathrm{i}}{2}\rho_{01}\,\mathcal{V}_{10}\,\mathrm{e}^{\mathrm{i}\Delta t}+\text{c.c.}\,,
\end{aligned}\tag{B.1}$$

where the rotating-wave approximation was considered in order to neglect the fast oscillating terms [46].

The ground state population can be easily computed by remembering the normalization $\rho_{00}+\rho_{11}=1$, or in the differential form $\frac{\partial\rho_{00}(t)}{\partial t}=-\frac{\partial\rho_{11}(t)}{\partial t}$.

The off-diagonal term ρ_{01} is also computed with equation (3.2), and simplified with the rotating-wave approximation.

$$\begin{aligned}
\frac{\partial\rho_{01}(t)}{\partial t} &= \sum_k \frac{\mathrm{i}}{2}\rho_{0k}\,\mathrm{e}^{-\mathrm{i}\omega_{1k}t}\left(\mathcal{V}^*_{1k}\,\mathrm{e}^{\mathrm{i}\omega t}+\mathcal{V}_{k1}\,\mathrm{e}^{-\mathrm{i}\omega t}\right)-\frac{\mathrm{i}}{2}\rho_{k1}\,\mathrm{e}^{\mathrm{i}\omega_{0k}t}\left(\mathcal{V}_{0k}\,\mathrm{e}^{-\mathrm{i}\omega t}+\mathcal{V}^*_{k0}\,\mathrm{e}^{\mathrm{i}\omega t}\right)\\
&= \frac{\mathrm{i}}{2}\rho_{00}\,\mathrm{e}^{-\mathrm{i}\omega_r t}\left(\mathcal{V}^*_{10}\,\mathrm{e}^{\mathrm{i}\omega t}+\mathcal{V}_{01}\,\mathrm{e}^{-\mathrm{i}\omega t}\right)+\frac{\mathrm{i}}{2}\rho_{01}\left(\mathcal{V}^*_{11}\,\mathrm{e}^{\mathrm{i}\omega t}+\mathcal{V}_{11}\,\mathrm{e}^{-\mathrm{i}\omega t}\right)\\
&\quad-\frac{\mathrm{i}}{2}\rho_{01}\left(\mathcal{V}_{00}\,\mathrm{e}^{-\mathrm{i}\omega t}+\mathcal{V}^*_{00}\,\mathrm{e}^{\mathrm{i}\omega t}\right)-\frac{\mathrm{i}}{2}\rho_{11}\,\mathrm{e}^{-\mathrm{i}\omega_r t}\left(\mathcal{V}_{01}\,\mathrm{e}^{-\mathrm{i}\omega t}+\mathcal{V}^*_{10}\,\mathrm{e}^{\mathrm{i}\omega t}\right)\\
\frac{\partial\rho_{01}(t)}{\partial t} &\approx \frac{\mathrm{i}}{2}(\rho_{00}-\rho_{11})\,\mathcal{V}^*_{10}\,\mathrm{e}^{-\mathrm{i}\Delta t}
\end{aligned}\tag{B.2}$$

Again, the ρ_{10} can be easily found with the symmetry $\rho_{10}=\rho^*_{01}$.

B.2 4-levels μH

Computing the ρ_{00}^{00} case (population of the ground state level) gives

$$\begin{aligned}
\frac{\partial \rho_{00}^{00}(t)}{\partial t} &= \sum_k \frac{\mathrm{i}}{2}\rho_{0k}^{0}\,\mathrm{e}^{-\mathrm{i}\omega_{0k}t}\left(\mathcal{V}_{0k}^{0\ *}\,\mathrm{e}^{\mathrm{i}\omega t}+\mathcal{V}_{k0}^{\ 0}\,\mathrm{e}^{-\mathrm{i}\omega t}\right)+\text{c.c.}\\
&= \frac{\mathrm{i}}{2}\rho_{00}^{00}\left(\mathcal{V}_{00}^{00*}\,\mathrm{e}^{\mathrm{i}\omega t}+\mathcal{V}_{00}^{00}\,\mathrm{e}^{-\mathrm{i}\omega t}\right)-\frac{\mathrm{i}}{2}\rho_{00}^{00}\left(\mathcal{V}_{00}^{00}\,\mathrm{e}^{-\mathrm{i}\omega t}+\mathcal{V}_{00}^{00*}\,\mathrm{e}^{\mathrm{i}\omega t}\right)\\
&\quad+\sum_{m_F}\frac{\mathrm{i}}{2}\rho_{01}^{0m_F}\,\mathrm{e}^{\mathrm{i}\omega_r t}\left(\mathcal{V}_{01}^{0m_F\,*}\,\mathrm{e}^{\mathrm{i}\omega t}+\mathcal{V}_{10}^{m_F0}\,\mathrm{e}^{-\mathrm{i}\omega t}\right)+\text{c.c.}\\
\frac{\partial \rho_{00}^{00}(t)}{\partial t} &\approx \sum_{m_F}\frac{\mathrm{i}}{2}\rho_{01}^{0m_F}\,\mathrm{e}^{\mathrm{i}\Delta t}\,\mathcal{V}_{10}^{m_F0}+\text{c.c.}\,,
\end{aligned}\tag{B.3}$$

where the rotation wave approximation allowed the fast oscillating terms to be neglected.

In the 4-levels case the normalization is not enough to immediately obtain the population of the excited level because it is degenerate. As such each of the $\rho_{11}^{m_F' m_F}$ must be computed.

$$\begin{aligned}
\frac{\partial \rho_{11}^{m_F' m_F}(t)}{\partial t} &= \sum_k \frac{\mathrm{i}}{2}\rho_{1k}^{m_F'}\,\mathrm{e}^{-\mathrm{i}\omega_{1k}t}\left(\mathcal{V}_{1k}^{m_F*}\,\mathrm{e}^{\mathrm{i}\omega t}+\mathcal{V}_{k1}^{\ m_F}\,\mathrm{e}^{-\mathrm{i}\omega t}\right)-\frac{\mathrm{i}}{2}\rho_{k1}^{\ m_F}\,\mathrm{e}^{\mathrm{i}\omega_{1k}t}\left(\mathcal{V}_{1k}^{m_F'}\,\mathrm{e}^{-\mathrm{i}\omega t}+\mathcal{V}_{k1}^{\ m_F'\,*}\,\mathrm{e}^{\mathrm{i}\omega t}\right)\\
&= \frac{\mathrm{i}}{2}\rho_{10}^{m_F'0}\,\mathrm{e}^{-\mathrm{i}\omega_r t}\left(\mathcal{V}_{10}^{m_F0*}\,\mathrm{e}^{\mathrm{i}\omega t}+\mathcal{V}_{01}^{0m_F}\,\mathrm{e}^{-\mathrm{i}\omega t}\right)-\frac{\mathrm{i}}{2}\rho_{01}^{0m_F}\,\mathrm{e}^{\mathrm{i}\omega_r t}\left(\mathcal{V}_{10}^{m_F'0}\,\mathrm{e}^{-\mathrm{i}\omega t}+\mathcal{V}_{01}^{0m_F'\,*}\,\mathrm{e}^{\mathrm{i}\omega t}\right)\\
&\quad+\sum_{M=-1}^{1}\frac{\mathrm{i}}{2}\rho_{11}^{m_F'M}\left(\mathcal{V}_{11}^{m_FM*}\,\mathrm{e}^{\mathrm{i}\omega t}+\mathcal{V}_{11}^{Mm_F}\,\mathrm{e}^{-\mathrm{i}\omega t}\right)-\frac{\mathrm{i}}{2}\rho_{11}^{Mm_F}\left(\mathcal{V}_{11}^{m_F'M}\,\mathrm{e}^{-\mathrm{i}\omega t}+\mathcal{V}_{11}^{Mm_F'\,*}\,\mathrm{e}^{\mathrm{i}\omega t}\right)\\
\frac{\partial \rho_{11}^{m_F' m_F}(t)}{\partial t} &\approx \frac{\mathrm{i}}{2}\rho_{10}^{m_F'0}\,\mathrm{e}^{-\mathrm{i}\Delta t}\,\mathcal{V}_{10}^{m_F0*}-\frac{\mathrm{i}}{2}\rho_{01}^{0m_F}\,\mathrm{e}^{\mathrm{i}\Delta t}\,\mathcal{V}_{10}^{m_F'0}
\end{aligned}\tag{B.4}$$

Once more, the rotation wave approximation was considered to eliminate fast oscillating terms.

Finally, the $\rho_{01}^{0m_F}$ case can be computed as

$$\begin{aligned}
\frac{\partial \rho_{01}^{0m_F}(t)}{\partial t} &= \sum_k \frac{\mathrm{i}}{2}\rho_{0k}^{0}\,\mathrm{e}^{-\mathrm{i}\omega_{1k}t}\left(\mathcal{V}_{1k}^{m_F\ *}\,\mathrm{e}^{\mathrm{i}\omega t}+\mathcal{V}_{k1}^{\ m_F}\,\mathrm{e}^{-\mathrm{i}\omega t}\right)-\frac{\mathrm{i}}{2}\rho_{k1}^{\ m_F}\,\mathrm{e}^{\mathrm{i}\omega_{0k}t}\left(\mathcal{V}_{0k}^{0}\,\mathrm{e}^{-\mathrm{i}\omega t}+\mathcal{V}_{k0}^{\ 0\,*}\,\mathrm{e}^{\mathrm{i}\omega t}\right)\\
&= \sum_{M=-1}^{1}\frac{\mathrm{i}}{2}\rho_{01}^{0M}\left(\mathcal{V}_{11}^{m_FM*}\,\mathrm{e}^{\mathrm{i}\omega t}+\mathcal{V}_{11}^{Mm_F}\,\mathrm{e}^{-\mathrm{i}\omega t}\right)-\frac{\mathrm{i}}{2}\rho_{11}^{Mm_F}\,\mathrm{e}^{-\mathrm{i}\omega_r t}\left(\mathcal{V}_{01}^{0M}\,\mathrm{e}^{-\mathrm{i}\omega t}+\mathcal{V}_{10}^{M0*}\,\mathrm{e}^{\mathrm{i}\omega t}\right)\\
&\quad+\frac{\mathrm{i}}{2}\rho_{00}^{00}\,\mathrm{e}^{-\mathrm{i}\omega_r t}\left(\mathcal{V}_{10}^{m_F0*}\,\mathrm{e}^{\mathrm{i}\omega t}+\mathcal{V}_{01}^{0m_F}\,\mathrm{e}^{-\mathrm{i}\omega t}\right)-\frac{\mathrm{i}}{2}\rho_{01}^{0m_F}\left(\mathcal{V}_{00}^{00}\,\mathrm{e}^{-\mathrm{i}\omega t}+\mathcal{V}_{00}^{00*}\,\mathrm{e}^{\mathrm{i}\omega t}\right)\\
\frac{\partial \rho_{01}^{0m_F}(t)}{\partial t} &\approx \frac{\mathrm{i}}{2}\rho_{00}^{00}\,\mathrm{e}^{-\mathrm{i}\Delta t}\,\mathcal{V}_{10}^{m_F0*}-\sum_{M=-1}^{1}\frac{\mathrm{i}}{2}\rho_{11}^{Mm_F}\,\mathrm{e}^{-\mathrm{i}\Delta t}\,\mathcal{V}_{10}^{M0*}\,,
\end{aligned}\tag{B.5}$$

again with by applying the rotation wave approximation.

B.3 Reducing 4-levels to 2-levels of μH

Considering relations between the 4-levels populations and the 2-levels populations, the 4-levels equations can be reduced to the 2-levels equations. With those relations, equations (3.3) and (3.5) are necessarily equal, and for such to happen, the following equation is verified:

$$\rho_{01}\,\mathcal{V}_{10} = \sum_{m_F} \rho_{01}^{0m_F}\,\mathcal{V}_{10}^{m_F 0} \tag{B.6}$$

Differentiating (B.6) in respect to time, will later allow for a comparison with (3.4). The differentiation is simplified with (3.7),

$$\begin{aligned}
\frac{\partial \rho_{01}\,\mathcal{V}_{10}}{\partial t} &= \sum_{m_F} \frac{\partial \rho_{01}^{0m_F}}{\partial t}\,\mathcal{V}_{10}^{m_F 0} \\
&= \sum_{m_F}\left(\frac{\mathrm{i}}{2}\rho_{00}^{00}\,\mathrm{e}^{-\mathrm{i}\Delta t}\left|\mathcal{V}_{10}^{m_F 0}\right|^2 - \sum_{M=-1}^{1}\frac{\mathrm{i}}{2}\rho_{11}^{M m_F}\,\mathrm{e}^{-\mathrm{i}\Delta t}\,\mathcal{V}_{10}^{M0*}\,\mathcal{V}_{10}^{m_F 0}\right) \\
&= \frac{\mathrm{i}}{2}\,\mathrm{e}^{-\mathrm{i}\Delta t}\left(\sum_{m_F}\rho_{00}^{00}\left|\mathcal{V}_{10}^{m_F 0}\right|^2 - \sum_{m_F M}\rho_{11}^{M m_F}\,\mathcal{V}_{10}^{M0*}\,\mathcal{V}_{10}^{m_F 0}\right).
\end{aligned} \tag{B.7}$$

By differentiating the last term of (B.7) with respect to time, and with the help of equation (3.6), one obtains

$$\begin{aligned}
\frac{\partial}{\partial t}\sum_{m_F M}\rho_{11}^{M m_F}\,\mathcal{V}_{10}^{M0*}\,\mathcal{V}_{10}^{m_F 0} &= \sum_{m_F M}\mathcal{V}_{10}^{M0*}\,\mathcal{V}_{10}^{m_F 0}\,\frac{\partial \rho_{11}^{M m_F}}{\partial t} \\
&= \sum_{m_F M}\mathcal{V}_{10}^{M0*}\,\mathcal{V}_{10}^{m_F 0}\left(\frac{\mathrm{i}}{2}\rho_{10}^{M0}\,\mathrm{e}^{-\mathrm{i}\Delta t}\,\mathcal{V}_{10}^{m_F 0*} - \frac{\mathrm{i}}{2}\rho_{01}^{0m_F}\,\mathrm{e}^{\mathrm{i}\Delta t}\,\mathcal{V}_{10}^{M0}\right) \\
&= \sum_{m_F M}\left|\mathcal{V}_{10}^{m_F 0}\right|^2\frac{\mathrm{i}}{2}\mathcal{V}_{10}^{M0*}\,\rho_{10}^{M0}\,\mathrm{e}^{-\mathrm{i}\Delta t} - \sum_{m_F M}\left|\mathcal{V}_{10}^{M0}\right|^2\frac{\mathrm{i}}{2}\,\mathcal{V}_{10}^{m_F 0}\,\rho_{01}^{0m_F}\,\mathrm{e}^{\mathrm{i}\Delta t} \\
&= \sum_{m_F M}\left|\mathcal{V}_{10}^{m_F 0}\right|^2\left(\frac{\partial \rho_{11}^{MM}}{\partial t} + \frac{\mathrm{i}}{2}\rho_{01}^{0M}\,\mathcal{V}_{10}^{M0}\,\mathrm{e}^{\mathrm{i}\Delta t}\right) - \sum_{m_F M}\left|\mathcal{V}_{10}^{m_F 0}\right|^2\frac{\mathrm{i}}{2}\,\mathcal{V}_{10}^{M0}\,\rho_{01}^{0M}\,\mathrm{e}^{\mathrm{i}\Delta t} \\
\frac{\partial}{\partial t}\sum_{m_F M}\rho_{11}^{M m_F}\,\mathcal{V}_{10}^{M0*}\,\mathcal{V}_{10}^{m_F 0} &= \sum_{m_F M}\left|\mathcal{V}_{10}^{m_F 0}\right|^2\frac{\partial \rho_{11}^{MM}}{\partial t} \\
\Longrightarrow \sum_{m_F M}\rho_{11}^{M m_F}\,\mathcal{V}_{10}^{M0*}\,\mathcal{V}_{10}^{m_F 0} &= \sum_{m_F M}\left|\mathcal{V}_{10}^{m_F 0}\right|^2\rho_{11}^{MM},
\end{aligned} \tag{B.8}$$

if taken into account that in the initial time $a_1^{m_F}(0) = 0$ for all sub-states m_F. This consideration means that at the beginning, the probability of having the atom in an excited state is zero, which is according to the process of formation of muonic atoms (section 1.3).

Using equation (3.8) and replacing (B.8) in (B.7) gives

$$\frac{\partial \rho_{01}\,\mathcal{V}_{10}}{\partial t} = \frac{\mathrm{i}}{2}\,\mathrm{e}^{-\mathrm{i}\Delta t}\,(\rho_{00} - \rho_{11})\sum_{m_F}\left|\mathcal{V}_{10}^{m_F 0}\right|^2, \tag{B.9}$$

and comparing (B.9) with (3.4) (multiplied by $\mathcal{V}_{10}$), implies that the $\mathcal{V}_{10}$ Rabi frequency is given by

$$|\mathcal{V}_{10}|^2 = \sum_{m_F} \left| \mathcal{V}_{10}^{m_F 0} \right|^2 . \tag{B.10}$$

B.4 4-levels $\mu^3\mathrm{He}^+$

Computing the ground states $\rho_{11}^{m_F' m_F}$ gives

$$\begin{aligned}
\frac{\partial \rho_{11}^{m_F' m_F}(t)}{\partial t} &= \sum_k \frac{\mathrm{i}}{2} \rho_{1k}^{m_F'} \mathrm{e}^{-\mathrm{i}\omega_{1k}t} \left(\mathcal{V}_{1k}^{m_F *} \mathrm{e}^{\mathrm{i}\omega t} + \mathcal{V}_{k1}^{\ m_F} \mathrm{e}^{-\mathrm{i}\omega t} \right) - \frac{\mathrm{i}}{2} \rho_{k1}^{\ m_F} \mathrm{e}^{\mathrm{i}\omega_{1k}t} \left(\mathcal{V}_{1k}^{m_F'} \mathrm{e}^{-\mathrm{i}\omega t} + \mathcal{V}_{k1}^{\ m_F' *} \mathrm{e}^{\mathrm{i}\omega t} \right) \\
&= \frac{\mathrm{i}}{2} \rho_{10}^{m_F' 0} \mathrm{e}^{\mathrm{i}\omega_r t} \left(\mathcal{V}_{10}^{m_F 0 *} \mathrm{e}^{\mathrm{i}\omega t} + \mathcal{V}_{01}^{0 m_F} \mathrm{e}^{-\mathrm{i}\omega t} \right) - \frac{\mathrm{i}}{2} \rho_{01}^{0 m_F} \mathrm{e}^{-\mathrm{i}\omega_r t} \left(\mathcal{V}_{10}^{m_F' 0} \mathrm{e}^{-\mathrm{i}\omega t} + \mathcal{V}_{01}^{0 m_F' *} \mathrm{e}^{\mathrm{i}\omega t} \right) \\
&\quad + \sum_{M=-1}^{1} \frac{\mathrm{i}}{2} \rho_{11}^{m_F' M} \left(\mathcal{V}_{11}^{m_F M *} \mathrm{e}^{\mathrm{i}\omega t} + \mathcal{V}_{11}^{M m_F} \mathrm{e}^{-\mathrm{i}\omega t} \right) - \frac{\mathrm{i}}{2} \rho_{11}^{M m_F} \left(\mathcal{V}_{11}^{m_F' M} \mathrm{e}^{-\mathrm{i}\omega t} + \mathcal{V}_{11}^{M m_F' *} \mathrm{e}^{\mathrm{i}\omega t} \right) \\
\frac{\partial \rho_{11}^{m_F' m_F}(t)}{\partial t} &\approx \frac{\mathrm{i}}{2} \rho_{10}^{m_F' 0} \mathrm{e}^{\mathrm{i}\Delta t} \mathcal{V}_{01}^{0 m_F} - \frac{\mathrm{i}}{2} \rho_{01}^{0 m_F} \mathrm{e}^{-\mathrm{i}\Delta t} \mathcal{V}_{01}^{0 m_F' *} ,
\end{aligned} \tag{B.11}$$

the excited state population, ρ_{00}^{00}, equation is

$$\begin{aligned}
\frac{\partial \rho_{00}^{00}(t)}{\partial t} &= \sum_k \frac{\mathrm{i}}{2} \rho_{0k}^{0} \mathrm{e}^{-\mathrm{i}\omega_{0k}t} \left(\mathcal{V}_{0k}^{0\ *} \mathrm{e}^{\mathrm{i}\omega t} + \mathcal{V}_{k0}^{\ 0} \mathrm{e}^{-\mathrm{i}\omega t} \right) + \text{c.c.} \\
&= \frac{\mathrm{i}}{2} \rho_{00}^{00} \left(\mathcal{V}_{00}^{00 *} \mathrm{e}^{\mathrm{i}\omega t} + \mathcal{V}_{00}^{00} \mathrm{e}^{-\mathrm{i}\omega t} \right) - \frac{\mathrm{i}}{2} \rho_{00}^{00} \left(\mathcal{V}_{00}^{00} \mathrm{e}^{-\mathrm{i}\omega t} + \mathcal{V}_{00}^{00 *} \mathrm{e}^{\mathrm{i}\omega t} \right) \\
&\quad + \sum_{m_F} \frac{\mathrm{i}}{2} \rho_{01}^{0 m_F} \mathrm{e}^{-\mathrm{i}\omega_r t} \left(\mathcal{V}_{01}^{0 m_F *} \mathrm{e}^{\mathrm{i}\omega t} + \mathcal{V}_{10}^{m_F 0} \mathrm{e}^{-\mathrm{i}\omega t} \right) + \text{c.c.} \\
\frac{\partial \rho_{00}^{00}(t)}{\partial t} &\approx \sum_{m_F} \frac{\mathrm{i}}{2} \rho_{01}^{0 m_F} \mathrm{e}^{-\mathrm{i}\Delta t} \mathcal{V}_{01}^{0 m_F *} + \text{c.c.} ,
\end{aligned} \tag{B.12}$$

and the $\rho_{01}^{0 m_F}$ coherence populations are

$$\begin{aligned}
\frac{\partial \rho_{01}^{0 m_F}(t)}{\partial t} &= \sum_k \frac{\mathrm{i}}{2} \rho_{0k}^{0} \mathrm{e}^{-\mathrm{i}\omega_{1k}t} \left(\mathcal{V}_{1k}^{m_F\ *} \mathrm{e}^{\mathrm{i}\omega t} + \mathcal{V}_{k1}^{\ m_F} \mathrm{e}^{-\mathrm{i}\omega t} \right) - \frac{\mathrm{i}}{2} \rho_{k1}^{\ m_F} \mathrm{e}^{\mathrm{i}\omega_{0k}t} \left(\mathcal{V}_{0k}^{0} \mathrm{e}^{-\mathrm{i}\omega t} + \mathcal{V}_{k0}^{\ 0 *} \mathrm{e}^{\mathrm{i}\omega t} \right) \\
&= \sum_{M=-1}^{1} \frac{\mathrm{i}}{2} \rho_{01}^{0M} \left(\mathcal{V}_{11}^{m_F M *} \mathrm{e}^{\mathrm{i}\omega t} + \mathcal{V}_{11}^{M m_F} \mathrm{e}^{-\mathrm{i}\omega t} \right) - \frac{\mathrm{i}}{2} \rho_{11}^{M m_F} \mathrm{e}^{\mathrm{i}\omega_r t} \left(\mathcal{V}_{01}^{0M} \mathrm{e}^{-\mathrm{i}\omega t} + \mathcal{V}_{10}^{M 0 *} \mathrm{e}^{\mathrm{i}\omega t} \right) \\
&\quad + \frac{\mathrm{i}}{2} \rho_{00}^{00} \mathrm{e}^{\mathrm{i}\omega_r t} \left(\mathcal{V}_{10}^{m_F 0 *} \mathrm{e}^{\mathrm{i}\omega t} + \mathcal{V}_{01}^{0 m_F} \mathrm{e}^{-\mathrm{i}\omega t} \right) - \frac{\mathrm{i}}{2} \rho_{01}^{0 m_F} \left(\mathcal{V}_{00}^{00} \mathrm{e}^{-\mathrm{i}\omega t} + \mathcal{V}_{00}^{00 *} \mathrm{e}^{\mathrm{i}\omega t} \right) \\
\frac{\partial \rho_{01}^{0 m_F}(t)}{\partial t} &\approx \frac{\mathrm{i}}{2} \rho_{00}^{00} \mathrm{e}^{\mathrm{i}\Delta t} \mathcal{V}_{01}^{0 m_F} - \sum_{M=-1}^{1} \frac{\mathrm{i}}{2} \rho_{11}^{M m_F} \mathrm{e}^{\mathrm{i}\Delta t} \mathcal{V}_{01}^{0M} ,
\end{aligned} \tag{B.13}$$

with the rotating wave approximation being used in equations (B.11), (B.12) and (B.13) to neglect the fast-oscillating terms.

C

Rotating Wave Approximation

In the derivation of the time dynamics of laser atoms interactions, the rotating wave approximation is often considered, allowing to simplify the Bloch equations by dropping the fast oscillating terms [46, 50]. In simple systems (without decays and with only 2 levels, for example) this approximation even allows for analytical solutions for the time evolution of the populations.

If we consider a differential equation with two oscillating terms with frequencies f_1 and f_2, each scaled by a (complex) constant C_1 and C_2 respectively, (C.1a), this equation can be solved by simple integration which results in equation (C.1b).

$$\frac{\mathrm{d}f(t)}{\mathrm{d}t} = C_1\,\mathrm{e}^{\mathrm{i}f_1 t} + C_2\,\mathrm{e}^{\mathrm{i}f_2 t} \tag{C.1a}$$

$$f(t) = -\frac{\mathrm{i}C_1}{f_1}\,\mathrm{e}^{\mathrm{i}f_1 t} - \frac{\mathrm{i}C_2}{f_2}\,\mathrm{e}^{\mathrm{i}f_2 t} \tag{C.1b}$$

By inspection of the solution (C.1b), if the C_1 and C_2 magnitudes are in the same order, and one of the frequencies is much larger then the other, the term corresponding to that frequency can be ignored. Let's consider without lost of generality that $f_2 \gg f_1$. Comparing the magnitude of both terms we get

$$\left|-\frac{\mathrm{i}C_1}{f_1}\,\mathrm{e}^{\mathrm{i}f_1 t}\right| = \frac{|C_1|}{f_1} \gg \frac{|C_2|}{f_2} = \left|-\frac{\mathrm{i}C_1}{f_1}\,\mathrm{e}^{\mathrm{i}f_1 t}\right|, \tag{C.2}$$

where $|C_1| \approx |C_2|$ is considered. Since the term with frequency f_1 will have a much greater magnitude, the term with frequency f_2 can be dropped.

When applying this approximation in the Bloch equations, two conditions must be met: One of the frequencies of oscillation must be much lower than the others, and C coefficients must have about the same magnitude.

It should be noticed that in the Bloch equations deduced in appendix B, the C coefficients are actually functions, more precisely, the populations (of the specific system) multiplied by a Rabi frequency. Since this coefficient has a time dependency, the integration would not be so direct as in (C.1), however, using integration by parts, each term would still be proportional to the inverse of its oscillating frequency. Furthermore, the

Rabi frequencies, within the same system, are all in the same order of magnitude. The populations are between 0 and 1 due to the normalization and the magnitude of the coherent populations are between 0 and 0.5 ($\left|\rho_{01}\right|^2 = \rho_{00}\rho_{11} = \rho_{11} - \rho_{11}^2$ which is maximum for $\rho_{11} = 0.5$, corresponding to $\left|\rho_{01}\right| = 0.5$). With this it can be concluded that the "coefficients"multiplying by the oscillating parts are all in the same orders of magnitude, and as such, if there is a much lower frequency (which is the case when relatively close to resonance, $\Delta \approx 0$), the rotating wave approximation can be employed.

D

Calculation of the Rabi Frequency

In this appendix, the Rabi frequency is computed according to its definition (for the M1 transition), equation (2.81), and considering the magnetic moment (2.84). The Rabi frequency is computed for the μH system and for the μ^3He^+ system.

D.1 μH System - $\mathcal{V}_{10}^{m_F 0}$

By noting the dot product definition, the Wigner-Eckart theorem, and that $\vec{\mu}$ is a rank 1 Hermitian tensor (see appendix A for more details), the following simplification for the Rabi frequencies is obtained

$$\begin{aligned}
\mathcal{V}_{10}^{m_F 0} &= -\frac{E}{c\hbar}\langle F=1,\, m_F|\vec{\mu}|F=0,\, m_F=0\rangle \cdot \left(\hat{\mathbf{k}}\times\hat{\varepsilon}\right) \\
&= -\frac{E}{c\hbar}\sum_{\lambda}\left(\langle F=1,\, m_F|\vec{\mu}_\lambda|F=0,\, m_F=0\rangle\right)^{\dagger}\left(\hat{\mathbf{k}}\times\hat{\varepsilon}\right)_\lambda \\
&= -\frac{E}{c\hbar}\sum_{\lambda}(-1)^{\lambda}\langle F=0,\, m_F=0|\vec{\mu}_{-\lambda}|F=1,\, m_F\rangle\left(\hat{\mathbf{k}}\times\hat{\varepsilon}\right)_\lambda \\
&= -\frac{E}{c\hbar}\left\langle F=0\middle\|\vec{\mu}\middle\|F=1\right\rangle(-1)^{0-0}\sum_{\lambda}(-1)^{\lambda}\begin{pmatrix}0 & 1 & 1\\ 0 & -\lambda & m_F\end{pmatrix}\left(\hat{\mathbf{k}}\times\hat{\varepsilon}\right)_\lambda \\
&= -\frac{E}{c\hbar}\left\langle F=0\middle\|\vec{\mu}\middle\|F=1\right\rangle\sum_{\lambda}(-1)^{\lambda}\frac{(-1)^{\lambda+1}}{\sqrt{3}}\delta_{\lambda m_F}\left(\hat{\mathbf{k}}\times\hat{\varepsilon}\right)_\lambda \\
&= \frac{E}{c\hbar}\left\langle F=0\middle\|\vec{\mu}\middle\|F=1\right\rangle\frac{1}{\sqrt{3}}\left(\hat{\mathbf{k}}\times\hat{\varepsilon}\right)_{m_F}.
\end{aligned} \tag{D.1}$$

The $|F=0\rangle$ and $|F=1\rangle$ states both have $L=0$, and as such $\vec{\mathbf{J}}$=$\vec{\mathbf{S}}$ and $\vec{\mathbf{F}}$ can be seen as just the coupling between $\vec{\mathbf{S}}$ and $\vec{\mathbf{I}}$. As a consequence, the $\vec{\mathbf{L}}$ term in magnetic moment evaluates to 0, and thus the magnetic moment is just $\vec{\mu}=-\frac{e}{2m}\left(g_S\vec{\mathbf{S}}+\frac{m}{M}g_N\vec{\mathbf{I}}\right)$. Furthermore, these states both have $S=I=1/2$. The reduced matrix element $\left\langle F=0\middle\|\vec{\mu}\middle\|F=1\right\rangle$ can then be computed (generic case in appendix A)

$$\left\langle F=0\middle\|\vec{\mu}\middle\|F=1\right\rangle=-\frac{eg_S}{2m}\left\langle F=0\middle\|\vec{\mathbf{S}}\middle\|F=1\right\rangle-\frac{eg_N}{2M}\left\langle F=0\middle\|\vec{\mathbf{I}}\middle\|F=1\right\rangle$$

$$
\begin{aligned}
&= -\frac{eg_S\hbar}{2m}\sqrt{3}(-1)^{\frac{1}{2}+\frac{1}{2}+1+1}\begin{Bmatrix} 0 & 1 & 1 \\ \frac{1}{2} & \frac{1}{2} & \frac{1}{2} \end{Bmatrix}\sqrt{\frac{1}{2}\left(\frac{1}{2}+1\right)\left(2\times\frac{1}{2}+1\right)} \\
&\quad -\frac{eg_N\hbar}{2M}\sqrt{3}(-1)^{2\times 1+0-\frac{1}{2}-\frac{1}{2}+1}\begin{Bmatrix} 0 & 1 & 1 \\ \frac{1}{2} & \frac{1}{2} & \frac{1}{2} \end{Bmatrix}\sqrt{\frac{1}{2}\left(\frac{1}{2}+1\right)\left(2\times\frac{1}{2}+1\right)} \\
&= \frac{eg_S\hbar}{2m}\sqrt{3}\frac{1}{\sqrt{6}}\sqrt{\frac{3}{2}} - \frac{eg_N\hbar}{2M}\sqrt{3}\frac{1}{\sqrt{6}}\sqrt{\frac{3}{2}} \\
&= \frac{e\hbar}{4}\sqrt{3}\left(\frac{g_S}{m}-\frac{g_N}{M}\right)
\end{aligned}
\tag{D.2}
$$

The components of the polarization vector $\hat{\mathbf{k}}\times\hat{\varepsilon}$ can be obtained with equation (2.40) and are given by

$$
\left(\hat{\mathbf{k}}\times\hat{\varepsilon}\right)_{\pm} = \mp\frac{\mathrm{i}\,\mathrm{e}^{\mp\mathrm{i}\chi}}{\sqrt{2}}\frac{\eta\mp 1}{\sqrt{\eta^2+1}}\,, \qquad \left(\hat{\mathbf{k}}\times\hat{\varepsilon}\right)_0 = 0\,. \tag{D.3}
$$

Introducing equations (D.2) and (D.3) into (D.1), and using the relation $eE=\sqrt{8\pi\alpha\hbar\mathcal{I}}$ between the electric field amplitude E and the its intensity $\mathcal{I}$,

$$
\begin{aligned}
\mathcal{V}_{10}^{\pm 0} &= \mp\sqrt{8\pi\alpha\hbar\mathcal{I}}\left(\frac{g_S}{4cm}-\frac{g_N}{4cM}\right)\frac{\mathrm{i}\,\mathrm{e}^{\mp\mathrm{i}\chi}}{\sqrt{2}}\frac{\eta\mp 1}{\sqrt{\eta^2+1}}\,, \qquad \mathcal{V}_{10}^{00}=0 \\
&\approx \mp 51.23\sqrt{\mathcal{I}}\frac{\mathrm{i}\,\mathrm{e}^{\mp\mathrm{i}\chi}}{\sqrt{2}}\frac{\eta\mp 1}{\sqrt{\eta^2+1}}\,,
\end{aligned}
\tag{D.4}
$$

here, the $51.23\sqrt{\mathcal{I}}\,\mathrm{rad\,s^{-1}}$ is the same value obtained in [47].

D.2 $\mu^3\mathrm{He}^+$ System - $\mathcal{V}_{01}^{0m_F}$

The Bloch equations deduced in section 3.3 are dependent on the Rabi frequencies, $\mathcal{V}_{01}^{0m_F}$. These frequencies can be deduced in the same manner as the ones in section D.1, making use of the definition of Rabi frequency (2.81) and magnetic moment (2.84).

$$
\begin{aligned}
\mathcal{V}_{01}^{0m_F} &= -\frac{E}{c\hbar}\langle F=0,\, m_F=0|\vec{\mu}|F=1,\, m_F\rangle\cdot\left(\hat{\mathbf{k}}\times\hat{\varepsilon}\right) \\
&= -\frac{E}{c\hbar}\sum_{\lambda}\left(\langle F=0,\, m_F=0|\vec{\mu}_\lambda|F=1,\, m_F\rangle\right)^{\dagger}\left(\hat{\mathbf{k}}\times\hat{\varepsilon}\right)_\lambda \\
&= -\frac{E}{c\hbar}\sum_{\lambda}(-1)^{\lambda}\langle F=1,\, m_F|\vec{\mu}_{-\lambda}|F=0,\, m_F=0\rangle\left(\hat{\mathbf{k}}\times\hat{\varepsilon}\right)_\lambda \\
&= -\frac{E}{c\hbar}\left\langle F=1\middle\|\vec{\mu}\middle\|F=0\right\rangle(-1)^{1-m_F}\sum_{\lambda}(-1)^{\lambda}\begin{pmatrix} 1 & 1 & 0 \\ -m_F & -\lambda & 0 \end{pmatrix}\left(\hat{\mathbf{k}}\times\hat{\varepsilon}\right)_\lambda \\
&= \frac{E}{c\hbar}\left\langle F=1\middle\|\vec{\mu}\middle\|F=0\right\rangle(-1)^{-m_F}\sum_{\lambda}(-1)^{\lambda}\frac{(-1)^{\lambda+1}}{\sqrt{3}}\delta_{-\lambda m_F}\left(\hat{\mathbf{k}}\times\hat{\varepsilon}\right)_\lambda \\
&= \frac{E}{c\hbar}\left\langle F=1\middle\|\vec{\mu}\middle\|F=0\right\rangle\frac{(-1)^{1-m_F}}{\sqrt{3}}\left(\hat{\mathbf{k}}\times\hat{\varepsilon}\right)_{-m_F}\,.
\end{aligned}
\tag{D.5}
$$

As in the μH case, the magnetic moment can be considered to be $\vec{\mu} = -\frac{e}{2m}\left(g_S\vec{\mathbf{S}} + \frac{m}{M}g_N\vec{\mathbf{I}}\right)$, and the angular momentum $\vec{\mathbf{F}}$ can be considered to be just the coupling between the $\vec{\mathbf{S}}$ and $\vec{\mathbf{I}}$ angular momenta. The reduced matrix element is then

$$\begin{aligned}
\left\langle F=1\left\|\vec{\mu}\right\|F=0\right\rangle &= -\frac{eg_S}{2m}\left\langle F=1\left\|\vec{\mathbf{S}}\right\|F=0\right\rangle - \frac{eg_N}{2M}\left\langle F=1\left\|\vec{\mathbf{I}}\right\|F=0\right\rangle \\
&= -\frac{eg_S\hbar}{2m}\sqrt{3}(-1)^{\frac{1}{2}+\frac{1}{2}+0+1}\begin{Bmatrix}1 & 1 & 0\\ \frac{1}{2} & \frac{1}{2} & \frac{1}{2}\end{Bmatrix}\sqrt{\frac{1}{2}\left(\frac{1}{2}+1\right)\left(2\times\frac{1}{2}+1\right)} \\
&\quad -\frac{eg_N\hbar}{2M}\sqrt{3}(-1)^{2\times0+1-\frac{1}{2}-\frac{1}{2}+1}\begin{Bmatrix}1 & 1 & 0\\ \frac{1}{2} & \frac{1}{2} & \frac{1}{2}\end{Bmatrix}\sqrt{\frac{1}{2}\left(\frac{1}{2}+1\right)\left(2\times\frac{1}{2}+1\right)} \\
&= -\frac{eg_S\hbar}{2m}\sqrt{3}\frac{1}{\sqrt{6}}\sqrt{\frac{3}{2}} + \frac{eg_N\hbar}{2M}\sqrt{3}\frac{1}{\sqrt{6}}\sqrt{\frac{3}{2}} \\
&= -\frac{e\hbar}{4}\sqrt{3}\left(\frac{g_S}{m} - \frac{g_N}{M}\right). \qquad \text{(D.6)}
\end{aligned}$$

Finally introducing equations (D.6) and (D.3) into (D.5), and using the relation $eE = \sqrt{8\pi\alpha\hbar\mathcal{I}}$, the Rabi frequencies for the μ^3He$^+$ system are obtained,

$$\begin{aligned}
\mathcal{V}_{01}^{0\pm} &= \mp\sqrt{8\pi\alpha\hbar\mathcal{I}}\left(\frac{g_S}{4mc} - \frac{g_N}{4Mc}\right)\frac{\mathrm{i}\,\mathrm{e}^{\pm\mathrm{i}\chi}}{\sqrt{2}}\frac{\eta\pm1}{\sqrt{\eta^2+1}}, \qquad \mathcal{V}_{01}^{00} = 0 \qquad \text{(D.7)} \\
\mathcal{V}_{01}^{0\pm} &\approx \mp 35.87\sqrt{\mathcal{I}}\frac{\mathrm{i}\,\mathrm{e}^{\pm\mathrm{i}\chi}}{\sqrt{2}}\frac{\eta\pm1}{\sqrt{\eta^2+1}}.
\end{aligned}$$

E

Statistical Weights

In this appendix, the statistical weights in collisional decays to degenerate states are calculated. This calculation main support is on the conservation of angular momentum of the system in question [52], and in standard coupling rules.

E.1 Elastic Decays of $F = 1$ Sub-States of μH

In the elastic interaction (3.39) , the μH atom interacts with one of the H atoms of the H_2 molecule. The other molecule acts only as a spectator in this three body nuclear scattering. Since this is nuclear scattering, only the nuclear spin of the bc molecule matters.

If we call the interacting H atom b, with spin $\vec{\mathbf{s}}_b$, and the spectator H atom c, with spin $\vec{\mathbf{s}}_c$, the total angular momentum, $\vec{\mathbf{J}}_T = \vec{\mathbf{F}} + \vec{\mathbf{s}}_b + \vec{\mathbf{s}}_c$, of the $\mu\mathrm{H} + bc$ system must be conserved (and its projection m_{J_T}), as well as the angular momentum of the interacting bodies, b and μH, $\vec{\mathbf{S}}_b = \vec{\mathbf{F}} + \vec{\mathbf{s}}_b$ (and its projection m_{S_b}). The angular momentum of the interacting bodies, $\vec{\mathbf{S}}_b = \vec{\mathbf{F}} + \vec{\mathbf{s}}_b$, is given by coupling rules, considering that the nuclear spin of b is $s_b = 1/2$, and $F = 1$ (since the statistical weights being calculated are between the $F = 1$ states):

$$\left|1 - \frac{1}{2}\right| \leq S_b \leq 1 + \frac{1}{2} \implies S_b = \frac{1}{2},\ \frac{3}{2} \tag{E.1}$$

Considering an angular momentum $\vec{\mathbf{j}} = \vec{\mathbf{j}}_1 + \vec{\mathbf{j}}_2$, the coupled basis can be written in terms of linear combinations of the decoupled basis:

$$\begin{aligned}\left|jm_j\right\rangle = \left|j_1 j_2; jm_j\right\rangle &= \sum_{m_{j_1}, m_{j_2}} \left\langle j_1 m_{j_1}, j_2 m_{j_2} \middle| j_1 j_2; jm_j \right\rangle \left|j_1 m_{j_1}, j_2 m_{j_2}\right\rangle \\ &= \sum_{m_{j_1}, m_{j_2}} (-1)^{j_2 - j_1 - m_j} \sqrt{2j+1} \begin{pmatrix} j_1 & j_2 & j \\ m_{j_1} & m_{j_2} & -m_j \end{pmatrix} \left|j_1 m_{j_1}, j_2 m_{j_2}\right\rangle \end{aligned} \tag{E.2}$$

The $S_b = 1/2$ level has two sub-states ($m_{S_b} = -1/2, 1/2$) while the $J_M = 3/2$ has four sub-states ($m_{S_b} = -3/2, -1/2, 1/2, 3/2$). Writing these states in a decoupled basis (where the decoupled basis $\left|Fm_F, s_b m_{s_b}\right\rangle$ is written as $\left|m_F, m_{s_b}\right\rangle$ for simplicity), according to (E.2), gives (E.3) and (E.4)

- $S_b = 1/2$:

$$\left|F=1\, s_b=\frac{1}{2}; S_b=\frac{1}{2}\, m_{S_b}=-\frac{1}{2}\right\rangle = -\sqrt{\frac{2}{3}}\left|-1,\frac{1}{2}\right\rangle + \frac{1}{\sqrt{3}}\left|0,-\frac{1}{2}\right\rangle \tag{E.3a}$$

$$\left|F=1\, s_b=\frac{1}{2}; S_b=\frac{1}{2}\, m_{S_b}=\frac{1}{2}\right\rangle = -\frac{1}{\sqrt{3}}\left|0,\frac{1}{2}\right\rangle + \sqrt{\frac{2}{3}}\left|1,-\frac{1}{2}\right\rangle \tag{E.3b}$$

- $S_b = 3/2$:

$$\left|F=1\, s_b=\frac{1}{2}; S_b=\frac{3}{2}\, m_{S_b}=-\frac{3}{2}\right\rangle = \left|-1,-\frac{1}{2}\right\rangle \tag{E.4a}$$

$$\left|F=1\, s_b=\frac{1}{2}; S_b=\frac{3}{2}\, m_{S_b}=-\frac{1}{2}\right\rangle = \frac{1}{\sqrt{3}}\left|-1,\frac{1}{2}\right\rangle + \sqrt{\frac{2}{3}}\left|0,-\frac{1}{2}\right\rangle \tag{E.4b}$$

$$\left|F=1\, s_b=\frac{1}{2}; S_b=\frac{3}{2}\, m_{S_b}=\frac{1}{2}\right\rangle = \sqrt{\frac{2}{3}}\left|0,\frac{1}{2}\right\rangle + \frac{1}{\sqrt{3}}\left|1,-\frac{1}{2}\right\rangle \tag{E.4c}$$

$$\left|F=1\, s_b=\frac{1}{2}; S_b=\frac{3}{2}\, m_{S_b}=\frac{3}{2}\right\rangle = \left|1,\frac{1}{2}\right\rangle \tag{E.4d}$$

The total angular momentum of the system, $\vec{\mathbf{J}}_T = \vec{\mathbf{S}}_b + \vec{\mathbf{s}}_c$ is given by coupling of the angular momentum $\vec{\mathbf{S}}_b$ of the interacting bodies with the angular momentum of the spectator body, $\vec{\mathbf{s}}_c = 1/2$.

$$S_b = 1/2: \quad \left|\frac{1}{2}-\frac{1}{2}\right| \le J_T \le \frac{1}{2}+\frac{1}{2} \implies J_T = 0, 1 \tag{E.5a}$$

$$S_b = 3/2: \quad \left|\frac{3}{2}-\frac{1}{2}\right| \le J_T \le \frac{1}{2}+\frac{3}{2} \implies J_T = 1,\ 2 \tag{E.5b}$$

Now, each of the states in the coupled basis, $\left|J_T m_{J_T}\right\rangle$, can be decomposed in linear combinations of states of the decoupled basis, $\left|S_b m_{S_b}, s_c m_{s_c}\right\rangle$, according to (E.2), and these can be decomposed in linear combinations of states of the decoupled basis $\left|F m_F, s_b m_{s_b}, s_c m_{s_c}\right\rangle$. This last basis is written as $\left|m_F, m_{s_b}, m_{s_c}\right\rangle$ for simplicity.

- $S_b = 1/2$, $J_T = 0$:

$$\begin{aligned}\left|S_b=\frac{1}{2}\, s_c=\frac{1}{2}; J_T=0\, m_{J_T}=0\right\rangle = {} & \frac{1}{\sqrt{3}}\left|-1,\frac{1}{2},\frac{1}{2}\right\rangle - \frac{1}{\sqrt{6}}\left|0,-\frac{1}{2},\frac{1}{2}\right\rangle \\ & - \frac{1}{\sqrt{6}}\left|0,\frac{1}{2},-\frac{1}{2}\right\rangle + \frac{1}{\sqrt{3}}\left|1,-\frac{1}{2},-\frac{1}{2}\right\rangle\end{aligned} \tag{E.6}$$

- $S_b = 1/2$, $J_T = 1$:

$$\left|S_b=\frac{1}{2}\, s_c=\frac{1}{2}; J_T=1\, m_{J_T}=-1\right\rangle = -\sqrt{\frac{2}{3}}\left|-1,\frac{1}{2},-\frac{1}{2}\right\rangle + \frac{1}{\sqrt{3}}\left|0,-\frac{1}{2},-\frac{1}{2}\right\rangle \tag{E.7a}$$

$$\begin{aligned}\left|S_b=\frac{1}{2}\, s_c=\frac{1}{2}; J_T=1\, m_{J_T}=0\right\rangle = {} & -\frac{1}{\sqrt{3}}\left|-1,\frac{1}{2},\frac{1}{2}\right\rangle + \frac{1}{\sqrt{6}}\left|0,-\frac{1}{2},\frac{1}{2}\right\rangle \\ & - \frac{1}{\sqrt{6}}\left|0,\frac{1}{2},-\frac{1}{2}\right\rangle + \frac{1}{\sqrt{3}}\left|1,-\frac{1}{2},-\frac{1}{2}\right\rangle\end{aligned} \tag{E.7b}$$

$$\left|S_b=\frac{1}{2}\, s_c=\frac{1}{2}; J_T=1, m_{J_T}=1\right\rangle = -\frac{1}{\sqrt{3}}\left|0,\frac{1}{2},\frac{1}{2}\right\rangle + \sqrt{\frac{2}{3}}\left|1,-\frac{1}{2},\frac{1}{2}\right\rangle \tag{E.7c}$$

- $S_b = 3/2$, $J_T = 1$:

$$\left|S_b = \frac{3}{2}\, s_c = \frac{1}{2}; J_T = 1\, m_{J_T} = -1\right\rangle = -\frac{\sqrt{3}}{2}\left|-1, -\frac{1}{2}, \frac{1}{2}\right\rangle + \frac{1}{\sqrt{12}}\left|-1, \frac{1}{2}, -\frac{1}{2}\right\rangle + \frac{1}{\sqrt{6}}\left|0, -\frac{1}{2}, -\frac{1}{2}\right\rangle \tag{E.8a}$$

$$\left|S_b = \frac{3}{2}\, s_c = \frac{1}{2}; J_T = 1\, m_{J_T} = 0\right\rangle = -\frac{1}{\sqrt{6}}\left|-1, \frac{1}{2}, \frac{1}{2}\right\rangle - \frac{1}{\sqrt{3}}\left|0, -\frac{1}{2}, \frac{1}{2}\right\rangle + \frac{1}{\sqrt{3}}\left|0, \frac{1}{2}, -\frac{1}{2}\right\rangle + \frac{1}{\sqrt{6}}\left|1, -\frac{1}{2}, -\frac{1}{2}\right\rangle \tag{E.8b}$$

$$\left|S_b = \frac{3}{2}\, s_c = \frac{1}{2}; J_T = 1\, m_{J_T} = 1\right\rangle = -\frac{1}{\sqrt{6}}\left|0, \frac{1}{2}, \frac{1}{2}\right\rangle - \frac{1}{\sqrt{12}}\left|1, -\frac{1}{2}, \frac{1}{2}\right\rangle + \frac{\sqrt{3}}{2}\left|1, \frac{1}{2}, -\frac{1}{2}\right\rangle \tag{E.8c}$$

- $S_b = 3/2$, $J_T = 2$:

$$\left|S_b = \frac{3}{2}\, s_c = \frac{1}{2}; J_T = 2\, m_{J_T} = -2\right\rangle = \left|-1, -\frac{1}{2}, -\frac{1}{2}\right\rangle \tag{E.9a}$$

$$\left|S_b = \frac{3}{2}\, s_c = \frac{1}{2}; J_T = 2\, m_{J_T} = -1\right\rangle = \frac{1}{2}\left|-1, -\frac{1}{2}, \frac{1}{2}\right\rangle + \frac{1}{2}\left|-1, \frac{1}{2}, -\frac{1}{2}\right\rangle + \frac{\sqrt{2}}{2}\left|0, -\frac{1}{2}, -\frac{1}{2}\right\rangle \tag{E.9b}$$

$$\left|S_b = \frac{3}{2}\, s_c = \frac{1}{2}; J_T = 2\, m_{J_T} = 0\right\rangle = \frac{1}{\sqrt{6}}\left|-1, \frac{1}{2}, \frac{1}{2}\right\rangle + \frac{1}{\sqrt{3}}\left|0, -\frac{1}{2}, \frac{1}{2}\right\rangle + \frac{1}{\sqrt{3}}\left|0, \frac{1}{2}, -\frac{1}{2}\right\rangle + \frac{1}{\sqrt{6}}\left|1, -\frac{1}{2}, -\frac{1}{2}\right\rangle \tag{E.9c}$$

$$\left|S_b = \frac{3}{2}\, s_c = \frac{1}{2}; J_T = 2\, m_{J_T} = 1\right\rangle = \frac{\sqrt{2}}{2}\left|0, \frac{1}{2}, \frac{1}{2}\right\rangle + \frac{1}{2}\left|1, -\frac{1}{2}, \frac{1}{2}\right\rangle + \frac{1}{2}\left|1, \frac{1}{2}, -\frac{1}{2}\right\rangle \tag{E.9d}$$

$$\left|S_b = \frac{3}{2}\, s_c = \frac{1}{2}; J_T = 2\, m_{J_T} = 2\right\rangle = \left|1, \frac{1}{2}, \frac{1}{2}\right\rangle \tag{E.9e}$$

Equations (E.6), (E.7), (E.8) and (E.9), summarize all the 12 possible states with which the collision can occur, given that both J_T and m_{J_T} must conserve, as well as S_b and m_{S_b}. These states contain the information of the probability of the μH being in each m_F (table E.1).

Considering for example a decay due to collisions from the $m_F = -1$ state to the $m_F = 0$ state. It is known that the initial state had $m_F = -1$, so the total system had to be in a state in which it must be possible to have $m_F = -1$. There are 8 states for which this is possible (the ones where the $m_F = -1$ column is not 0), which are considered equally likely due to the non polarization of the bc molecule. Then it is known that J_T, m_{J_T}, S_b and m_{S_b} must conserve, and the final state must have $m_F = 0$. If the system was in the state $\left|S_b = 1/2\, s_c = 1/2; J_T = 0\, m_{J_T} = 0\right\rangle$ then it will have to stay in the same state in order to

Table E.1: Probability of being in each m_F state depending on total angular momentum J_T during the collision of $\mu\mathrm{H} + bc$.

			Probability of being in m_F state in the decoupled basis		
S_b	J_T	m_{J_T}	$m_F = -1$	$m_F = 0$	$m_F = 1$
1/2	0	0	1/3	1/3	1/3
	1	-1	2/3	1/3	0
		0	1/3	1/3	1/3
		1	0	1/3	2/3
3/2	1	-1	5/6	1/6	0
		0	1/6	2/3	1/6
		1	0	1/6	5/6
	2	-2	1	0	0
		-1	1/2	1/2	0
		0	1/6	2/3	1/6
		1	0	1/2	1/2
		2	0	0	1

conserve both J_T and S_b, and thus it will have a probability of 1/3 of having $m_F = 0$ after collision. The probability of being in the $m_F = 0$ state knowing that the system must have came from a $m_F = -1$ state is then:

$$W_{-0} = \frac{1}{8}\left(\frac{1}{3} + \frac{1}{3} + \frac{1}{3} + \frac{1}{6} + \frac{2}{3} + \frac{1}{2} + \frac{2}{3}\right) = \frac{3}{8} \tag{E.10}$$

which is also the statistical weight associated with the decay of the $m_F = -1$ to the $m_F = 0$ state (decay with a rate of $W_{-0}\Gamma_{el}^{F=1}$, where $\Gamma_{el}^{F=1}$ is the total decay of one $F = 1$ sub-level to another $F = 1$ sub-level). The Statistical weights of one sub-level must sum to 1:

$$\sum_{m'} W_{mm'} = 1 \tag{E.11}$$

This calculation can be performed for all possible decays between $F = 1$ sub-states of μH. The statistical weights are summarized in table E.2.

Table E.2: Statistical weights of elastic decays between $F = 1$ sub-states of μH. The statistical weights are $W_{mm'}$, where m is the initial state and m' the final state.

		final m_F		
		-1	0	1
initial m_F	-1	1/2	3/8	1/8
	0	3/10	2/5	3/10
	1	1/8	3/8	1/2

E.2 Elastic Decays of $F = 1$ Sub-States of $\mu^3\mathrm{He}^+$

To calculate the statistical weights for $\mu^3\mathrm{He}^+$ the process is similar to the μH case, however it is simpler for $\mu^3\mathrm{He}^+$.

The elastic interaction of (3.49) is between the μ^3He^+ (with total angular momentum $F=1$) and an ^3He (with spin 1/2). The total angular momentum, $\vec{\mathbf{J}}_T$, of this system, as well as the projection m_{J_T} must conserve in the collision.

Considering coupling rules, the possible values for J_T are

$$\left|1-\frac{1}{2}\right| \leq J_T \leq 1+\frac{1}{2} \implies J_T = \frac{1}{2}, \frac{3}{2} \tag{E.12}$$

and for each, there are $2J_T+1$ possible states. Writing these states in a decoupled basis (where the decoupled basis $\left|F m_F, s_{\mathrm{He}} m_{s_{\mathrm{He}}}\right\rangle$ is written as $\left|m_F, m_{s_{\mathrm{He}}}\right\rangle$ for simplicity), according to (E.2), gives (E.13) and (E.14):

- $J_T = 1/2$:

$$\left|F=1\, s_{\mathrm{He}}=\frac{1}{2}; J_T=\frac{1}{2}\, m_{J_T}=-\frac{1}{2}\right\rangle = -\sqrt{\frac{2}{3}}\left|-1,\frac{1}{2}\right\rangle + \frac{1}{\sqrt{3}}\left|0,-\frac{1}{2}\right\rangle \tag{E.13a}$$

$$\left|F=1\, s_{\mathrm{He}}=\frac{1}{2}; J_T=\frac{1}{2}\, m_{J_T}=\frac{1}{2}\right\rangle = -\frac{1}{\sqrt{3}}\left|0,\frac{1}{2}\right\rangle + \sqrt{\frac{2}{3}}\left|1,-\frac{1}{2}\right\rangle \tag{E.13b}$$

- $J_T = 3/2$:

$$\left|F=1\, s_{\mathrm{He}}=\frac{1}{2}; J_T=\frac{3}{2}\, m_{J_T}=-\frac{3}{2}\right\rangle = \left|-1,-\frac{1}{2}\right\rangle \tag{E.14a}$$

$$\left|F=1\, s_{\mathrm{He}}=\frac{1}{2}; J_T=\frac{3}{2}\, m_{J_T}=-\frac{1}{2}\right\rangle = \frac{1}{\sqrt{3}}\left|-1,\frac{1}{2}\right\rangle + \sqrt{\frac{2}{3}}\left|0,-\frac{1}{2}\right\rangle \tag{E.14b}$$

$$\left|F=1\, s_{\mathrm{He}}=\frac{1}{2}; J_T=\frac{3}{2}\, m_{J_T}=\frac{1}{2}\right\rangle = \sqrt{\frac{2}{3}}\left|0,\frac{1}{2}\right\rangle + \frac{1}{\sqrt{3}}\left|1,-\frac{1}{2}\right\rangle \tag{E.14c}$$

$$\left|F=1\, s_{\mathrm{He}}=\frac{1}{2}; J_T=\frac{3}{2}\, m_{J_T}=\frac{3}{2}\right\rangle = \left|1,\frac{1}{2}\right\rangle \tag{E.14d}$$

These equations carry the information of the probability of the μ^3He^+ being in each m_F, which is summarized in table E.3.

Table E.3: Probability of being in each m_F sub-state depending on total angular momentum J_T during the collision of $\mu^3He^+ + {}^3He$.

		Probability of being in m_F state in the decoupled basis		
J_T	m_{J_T}	$m_F=-1$	$m_F=0$	$m_F=1$
1/2	−1/2	2/3	1/3	0
	1/2	0	1/3	2/3
3/2	−3/2	1	0	0
	−1/2	1/3	2/3	0
	1/2	0	2/3	1/3
	3/2	0	0	1

Now the statistical weights from a m_F state are calculated by assuming equal probability of being in any of the states in the coupled basis (but guarantying that is possible to have that certain m_F), and knowing that the final state in coupled basis must be the same. The probability of having a final m_F' state is presented in table E.4

Table E.4: Statistical weights of elastic decays between $F = 1$ sub-states of $\mu^3\mathrm{He}^+$. The statistical weights are $W_{mm'}$, where m is the initial state and m' the final state.

		final m_F		
		-1	0	1
initial m_F	-1	2/3	1/3	0
	0	1/4	1/2	1/4
	1	0	1/3	2/3

E.3 Inelastic Decays of $\mu^3\mathrm{He}^+$

In the spin-flip collisional decay of $\mu^3\mathrm{He}^+$ (3.47), the initial state has $F = 0$ and the final state has $F = 1$. The possibilities of the final state were already calculated in the previous section of this appendix (equations (E.13) and (E.14)). For the initial state there is only $J_T = 1/2$ (since $F = 0$) and as such, there are two possible states:

$$\left|F = 0\, s_{\mathrm{He}} = \frac{1}{2}; J_T = \frac{1}{2}\, m_{J_T} = -\frac{1}{2}\right\rangle = \left|F = 0\, m_F = 0,\, s_{\mathrm{He}} = \frac{1}{2}\, m_{s_{\mathrm{He}}} = -\frac{1}{2}\right\rangle \tag{E.15}$$

$$\left|F = 0\, s_{\mathrm{He}} = \frac{1}{2}; J_T = \frac{1}{2}\, m_{J_T} = \frac{1}{2}\right\rangle = \left|F = 0\, m_F = 0,\, s_{\mathrm{He}} = \frac{1}{2}\, m_{s_{\mathrm{He}}} = \frac{1}{2}\right\rangle \tag{E.16}$$

There is an equal probability of being in any of these two states at start. After collision, the state in the coupled basis must be conserved (same $J_T = 1/2$ and m_{J_T}), but the state must be composed of linear combinations of states with $F = 1$, i.e., the states of (E.13). The probability of the $F = 0$ state decaying into each of the $F = 1$ sub-states is equally likely:

$$F = 0 \to m_F = -1: \quad \frac{1}{2} \times \left(\frac{2}{3} + 0\right) = \frac{1}{3} \tag{E.17}$$

$$F = 0 \to m_F = 0: \quad \frac{1}{2} \times \left(\frac{1}{3} + \frac{1}{3}\right) = \frac{1}{3} \tag{E.18}$$

$$F = 0 \to m_F = 1: \quad \frac{1}{2} \times \left(0 + \frac{2}{3}\right) = \frac{1}{3}\,. \tag{E.19}$$

F

Tables of FWHM and Peak Values in μH Diffusion

The tables in this appendix were all obtained considering the laser on for τ= 100 ns. All of the tables include the FWHM and peak value (which always corresponds to the resonance Δ= 0 MHz) of the dark state, and the tables for 4-levels also include the LMS of the dark state profile relative to the 2-levels case. The tables were obtained for two pressures (1 bar and 0.5 bar), three temperatures (22 K, 30 K and 50 K), two laser bandwidths (10 MHz and 100 MHz) and three fluences (10 Jcm^{-2}, 20 Jcm^{-2} and 50 Jcm^{-2}). Each table correspond to a different polarization (η= 0, 0.25, 0.5, 0.75, 1, left polarizations produce the same result as the positive with the same absolute value), for the 4-levels case, and the first table (F.1) to the 2-levels case (which does not depend on the polarization).

Table F.1: FWHM and peak values of the dark state profile in the 2-levels case.

			$\mathcal{F}$ = 10 Jcm^{-2}		$\mathcal{F}$ = 20 Jcm^{-2}		$\mathcal{F}$ = 50 Jcm^{-2}	
P [bar]	T [K]	Γ_l [MHz]	FWHM [MHz]	ρ_{DS}^{peak}	FWHM [MHz]	ρ_{DS}^{peak}	FWHM [MHz]	ρ_{DS}^{peak}
0.5	22	100	331	0.13	340	0.24	370	0.50
1	22	100	467	0.09	477	0.17	507	0.38
0.5	22	10	258	0.17	266	0.31	294	0.59
1	22	10	386	0.11	395	0.21	425	0.44
0.5	30	100	318	0.14	327	0.26	354	0.51
1	30	100	414	0.10	423	0.20	452	0.42
0.5	30	10	250	0.18	258	0.32	283	0.60
1	30	10	338	0.13	347	0.24	375	0.49
0.5	50	100	327	0.14	335	0.26	361	0.50
1	50	100	380	0.12	388	0.22	415	0.46
0.5	50	10	267	0.18	274	0.31	295	0.54
1	50	10	314	0.15	321	0.27	346	0.52

Table F.2: FWHM and peak values of the dark state profile in the 4-levels case with linear polarization, $\eta = 0$. The LMS of the dark state profile relative to the 2-levels case is also presented.

			$\mathcal{F}$= 10 Jcm^{-2}			$\mathcal{F}$= 20 Jcm^{-2}			$\mathcal{F}$= 50 Jcm^{-2}		
P [bar]	T [K]	Γ_l [MHz]	FWHM [MHz]	$\rho_{DS}{}^{peak}$	LMS$_\Delta$ $\times 10^{-2}$	FWHM [MHz]	$\rho_{DS}{}^{peak}$	LMS$_\Delta$ $\times 10^{-2}$	FWHM [MHz]	$\rho_{DS}{}^{peak}$	LMS$_\Delta$ $\times 10^{-2}$
0.5	22	100	331	0.13	0.037	340	0.24	0.130	369	0.50	0.555
1	22	100	467	0.09	0.010	476	0.17	0.038	507	0.38	0.185
0.5	22	10	258	0.17	0.061	266	0.31	0.201	294	0.59	0.720
1	22	10	386	0.11	0.014	395	0.21	0.051	425	0.44	0.234
0.5	30	100	318	0.14	0.063	326	0.26	0.218	354	0.52	0.883
1	30	100	414	0.10	0.020	423	0.20	0.071	452	0.42	0.327
0.5	30	10	250	0.18	0.110	258	0.33	0.347	283	0.60	1.101
1	30	10	338	0.13	0.029	347	0.24	0.100	375	0.49	0.421
0.5	50	100	327	0.14	0.139	335	0.26	0.466	360	0.51	1.750
1	50	100	379	0.12	0.050	388	0.22	0.175	414	0.46	0.741
0.5	50	10	267	0.18	0.264	274	0.31	0.758	295	0.54	1.912
1	50	10	314	0.15	0.080	321	0.27	0.263	345	0.53	0.930

Table F.3: FWHM and peak values of the dark state profile in the 4-levels case with polarization η= 0.25. The LMS of the dark state profile relative to the 2-levels case is also presented.

			$\mathcal{F}$= 10 Jcm^{-2}			$\mathcal{F}$= 20 Jcm^{-2}			$\mathcal{F}$= 50 Jcm^{-2}		
P [bar]	T [K]	Γ_l [MHz]	FWHM [MHz]	${\rho_{DS}}^{peak}$	LMS_Δ $\times 10^{-2}$	FWHM [MHz]	${\rho_{DS}}^{peak}$	LMS_Δ $\times 10^{-2}$	FWHM [MHz]	${\rho_{DS}}^{peak}$	LMS_Δ $\times 10^{-2}$
0.5	22	100	331	0.13	0.035	340	0.24	0.125	369	0.50	0.531
1	22	100	467	0.09	0.010	476	0.17	0.036	507	0.38	0.177
0.5	22	10	258	0.17	0.058	266	0.31	0.192	294	0.59	0.689
1	22	10	386	0.11	0.014	395	0.21	0.049	425	0.44	0.224
0.5	30	100	318	0.14	0.061	326	0.26	0.209	354	0.52	0.846
1	30	100	414	0.10	0.019	423	0.20	0.068	452	0.42	0.313
0.5	30	10	250	0.18	0.105	258	0.33	0.333	283	0.60	1.054
1	30	10	338	0.13	0.027	347	0.24	0.096	375	0.49	0.403
0.5	50	100	327	0.14	0.134	335	0.26	0.447	360	0.51	1.680
1	50	100	379	0.12	0.048	388	0.22	0.168	414	0.46	0.711
0.5	50	10	267	0.18	0.254	274	0.31	0.727	295	0.54	1.836
1	50	10	314	0.15	0.077	321	0.27	0.253	345	0.53	0.892

Table F.4: FWHM and peak values of the dark state profile in the 4-levels case with polarization η= 0.5. The LMS of the dark state profile relative to the 2-levels case is also presented.

			$\mathcal{F}$= 10 Jcm^{-2}			$\mathcal{F}$= 20 Jcm^{-2}			$\mathcal{F}$= 50 Jcm^{-2}		
P [bar]	T [K]	Γ_l [MHz]	FWHM [MHz]	${\rho_{DS}}^{peak}$	LMS$_\Delta$ $\times 10^{-2}$	FWHM [MHz]	${\rho_{DS}}^{peak}$	LMS$_\Delta$ $\times 10^{-2}$	FWHM [MHz]	${\rho_{DS}}^{peak}$	LMS$_\Delta$ $\times 10^{-2}$
0.5	22	100	331	0.13	0.032	340	0.24	0.114	369	0.50	0.486
1	22	100	467	0.09	0.009	477	0.17	0.033	507	0.38	0.162
0.5	22	10	258	0.17	0.053	266	0.31	0.175	294	0.59	0.630
1	22	10	386	0.11	0.013	395	0.21	0.045	425	0.44	0.205
0.5	30	100	318	0.14	0.056	326	0.26	0.192	354	0.52	0.775
1	30	100	414	0.10	0.017	423	0.20	0.062	452	0.42	0.288
0.5	30	10	250	0.18	0.097	258	0.33	0.305	283	0.60	0.967
1	30	10	338	0.13	0.025	347	0.24	0.088	375	0.49	0.370
0.5	50	100	327	0.14	0.123	335	0.26	0.412	360	0.51	1.547
1	50	100	379	0.12	0.044	388	0.22	0.154	414	0.46	0.655
0.5	50	10	267	0.18	0.233	274	0.31	0.670	295	0.54	1.693
1	50	10	314	0.15	0.071	321	0.27	0.233	345	0.53	0.822

Table F.5: FWHM and peak values of the dark state profile in the 4-levels case with polarization η= 0.75. The LMS of the dark state profile relative to the 2-levels case is also presented.

			$\mathcal{F}$= 10 Jcm^{-2}			$\mathcal{F}$= 20 Jcm^{-2}			$\mathcal{F}$= 50 Jcm^{-2}		
P [bar]	T [K]	Γ_l [MHz]	FWHM [MHz]	${\rho_{DS}}^{peak}$	LMS_Δ $\times 10^{-2}$	FWHM [MHz]	${\rho_{DS}}^{peak}$	LMS_Δ $\times 10^{-2}$	FWHM [MHz]	${\rho_{DS}}^{peak}$	LMS_Δ $\times 10^{-2}$
0.5	22	100	331	0.13	0.030	340	0.24	0.107	369	0.50	0.455
1	22	100	467	0.09	0.008	477	0.17	0.031	507	0.38	0.152
0.5	22	10	258	0.17	0.050	266	0.31	0.164	294	0.59	0.590
1	22	10	386	0.11	0.012	395	0.21	0.042	425	0.44	0.192
0.5	30	100	318	0.14	0.052	326	0.26	0.180	354	0.52	0.728
1	30	100	414	0.10	0.016	423	0.20	0.058	452	0.42	0.270
0.5	30	10	250	0.18	0.091	258	0.33	0.286	283	0.60	0.908
1	30	10	338	0.13	0.024	347	0.24	0.083	375	0.49	0.347
0.5	50	100	327	0.14	0.116	335	0.26	0.388	360	0.51	1.458
1	50	100	379	0.12	0.041	388	0.22	0.145	414	0.46	0.617
0.5	50	10	267	0.18	0.220	274	0.31	0.631	295	0.54	1.596
1	50	10	314	0.15	0.067	321	0.27	0.219	345	0.53	0.774

Table F.6: FWHM and peak values of the dark state profile in the 4-levels case with right circular polarization, $\eta = 1$. The LMS of the dark state profile relative to the 2-levels case is also presented.

			$\mathcal{F}$= 10 Jcm^{-2}			$\mathcal{F}$= 20 Jcm^{-2}			$\mathcal{F}$= 50 Jcm^{-2}		
P [bar]	T [K]	Γ_l [MHz]	FWHM [MHz]	$\rho_{DS}{}^{peak}$	LMS$_\Delta$ $\times 10^{-2}$	FWHM [MHz]	$\rho_{DS}{}^{peak}$	LMS$_\Delta$ $\times 10^{-2}$	FWHM [MHz]	$\rho_{DS}{}^{peak}$	LMS$_\Delta$ $\times 10^{-2}$
0.5	22	100	331	0.13	0.030	340	0.24	0.105	369	0.50	0.447
1	22	100	467	0.09	0.008	477	0.17	0.031	507	0.38	0.149
0.5	22	10	258	0.17	0.049	266	0.31	0.161	294	0.59	0.579
1	22	10	386	0.11	0.012	395	0.21	0.041	425	0.44	0.189
0.5	30	100	318	0.14	0.051	326	0.26	0.177	354	0.52	0.715
1	30	100	414	0.10	0.016	423	0.20	0.057	452	0.42	0.265
0.5	30	10	250	0.18	0.089	258	0.33	0.281	283	0.60	0.892
1	30	10	338	0.13	0.023	347	0.24	0.081	375	0.49	0.341
0.5	50	100	327	0.14	0.114	335	0.26	0.381	360	0.51	1.433
1	50	100	379	0.12	0.041	388	0.22	0.143	414	0.46	0.606
0.5	50	10	267	0.18	0.216	274	0.31	0.620	295	0.54	1.569
1	50	10	314	0.15	0.066	321	0.27	0.215	345	0.53	0.761

G

Figures of Time Evolution of Asymmetry in μH

The time evolution of the $F=1$ states and electron populations without decays are shown in figures G.1, G.2, G.3 and G.4, for the polarizations $\eta=0$, 0.25, 0.75 and 1, respectively. For all figures, the total excited state $F=1$ population is represented with a black line. The $m_F=-1$ sub-level population and electron ρ_e^- population are represented with a red line and the $m_F=1$ sub-level and ρ_e^+ with a blue line. The excited $m_F=0$ population is represented with a magenta line while the ρ_e^0 electron population is represented with a purple line. The exponential decay of the muon total population and its complementary negative exponential decay of the electron populations is included with the black dashed lines. The solutions presented were all obtained for a fluence of $\mathcal{F}=10$ Jcm^{-2} during $\tau=1000$ ns.

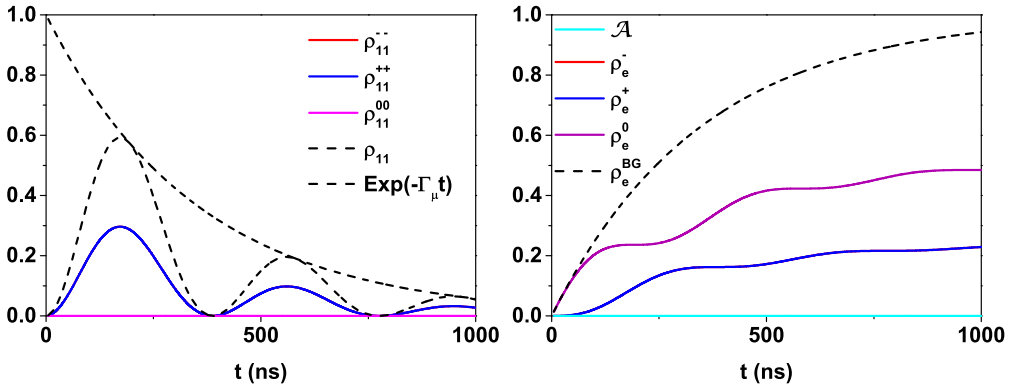

(a) Atomic populations.

(b) Electron populations.

Figure G.1: Time evolution of the $F=1$ atomic states (a) and electron populations (b) of μH for linear polarization, $\eta=0$.

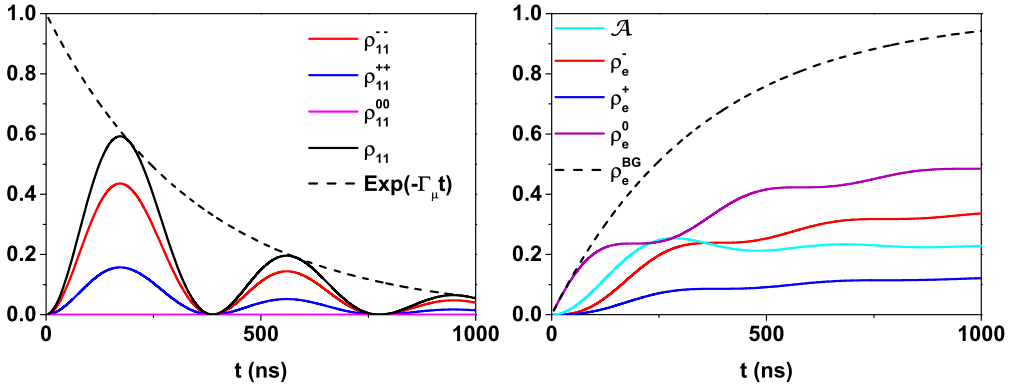

(a) Atomic populations. (b) Electron populations.

Figure G.2: Time evolution of the $F = 1$ atomic states (a) and electron populations (b) of μH for polarization $\eta = 0.25$.

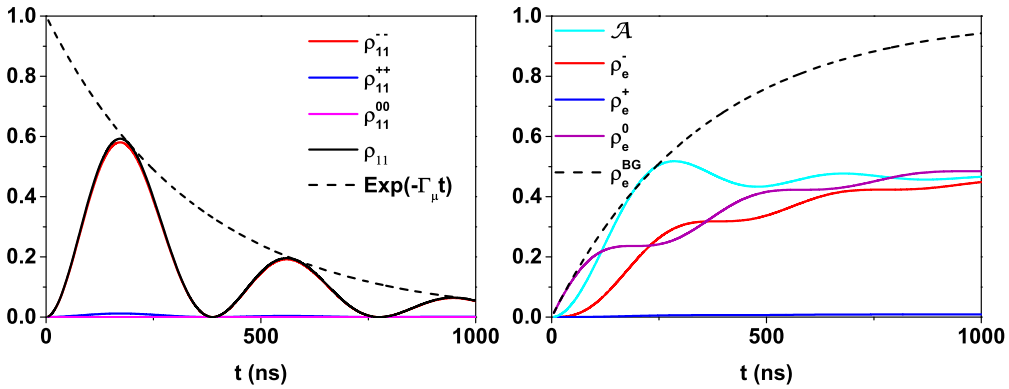

(a) Atomic populations. (b) Electron populations.

Figure G.3: Time evolution of the $F = 1$ atomic states (a) and electron populations (b) of μH for polarization $\eta = 0.75$.

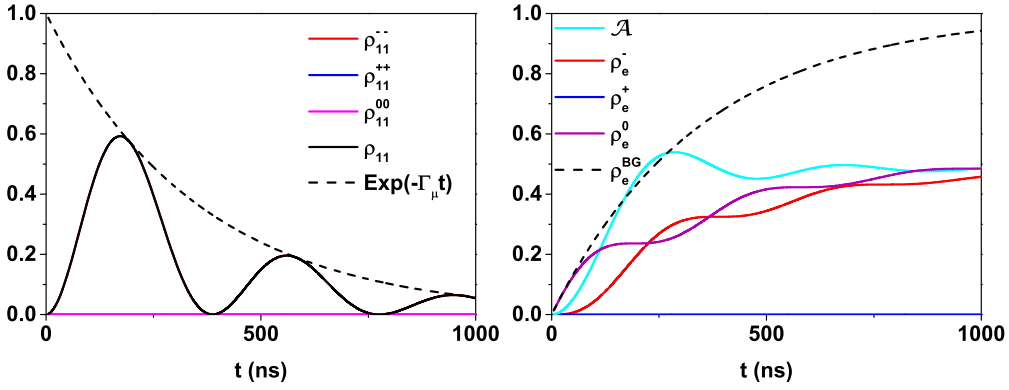

(a) Atomic populations. (b) Electron populations.

Figure G.4: Time evolution of the $F = 1$ atomic states (a) and electron populations (b) of μH for right circular polarization, $\eta = 1$.

The time evolution of the asymmetry $\mathcal{A}$, and of the ρ_e^- and ρ_e^+ electron populations is represented for different sets of temperature and pressure in figures G.5, G.6 and G.7. In these figures the asymmetry population is on the left and the electron populations on the right, with the colors representing the same polarization (η= 0, 0.25, 0.5, 0.75, and 1, have the colors black, red, blue, cyan and magenta respectively). In the electron populations plots, the solid line is for the ρ_e^- population and the dashed line for the ρ_e^+. The presented solutions were all obtained for a fluence of $\mathcal{F}$= 10 Jcm^{-2} during τ= 100 ns, and are scaled by a factor of 10^3.

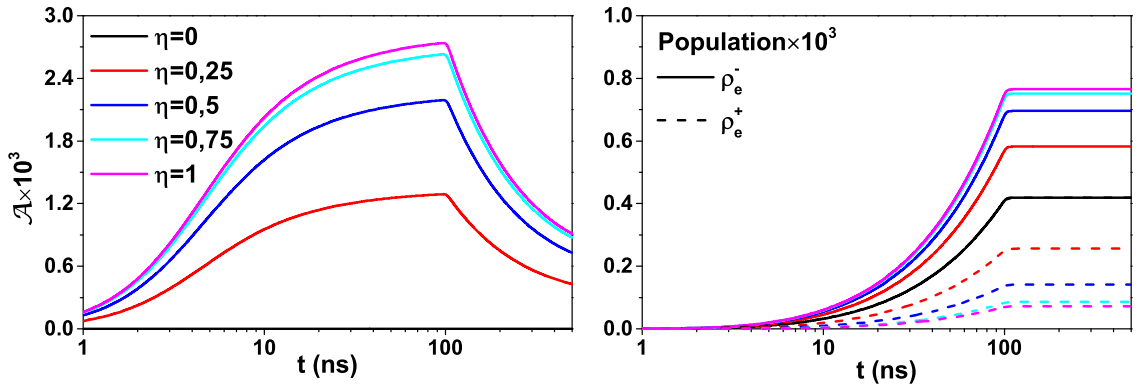

Figure G.5: Time evolution of the asymmetry and electron populations for T= 30 K and P= 0.5 bar.

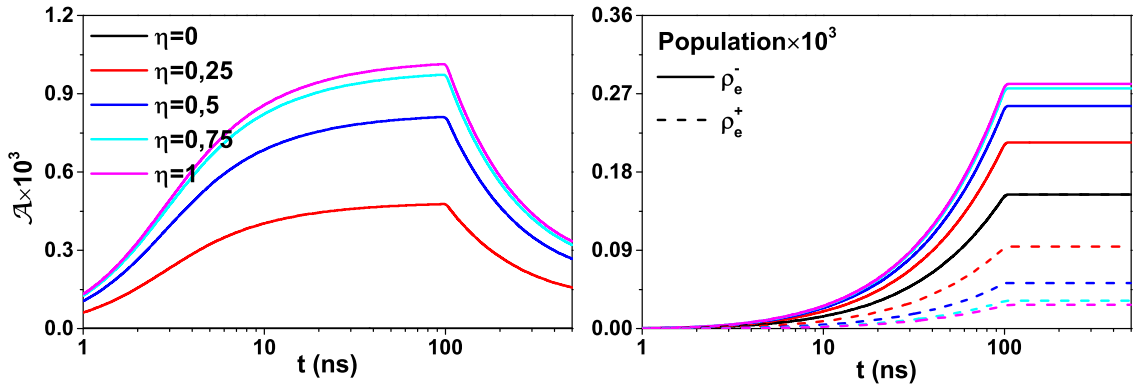

Figure G.6: Time evolution of the asymmetry and electron populations for T= 30 K and P= 1 bar.

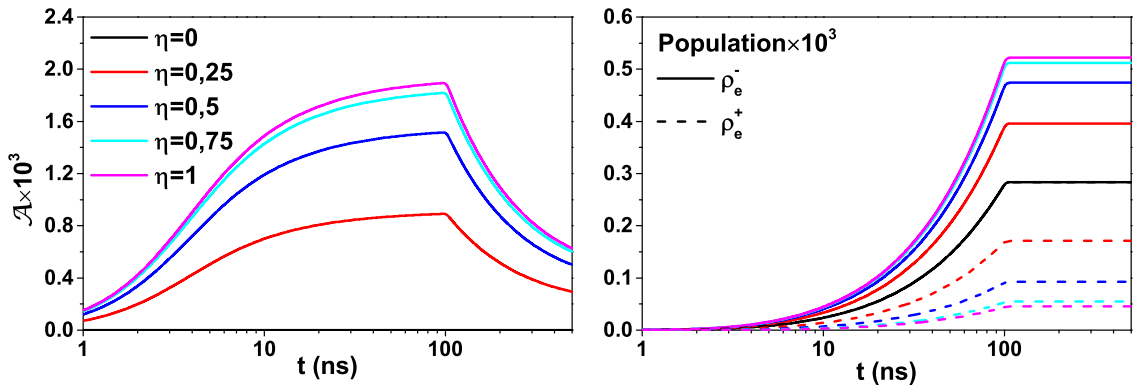

Figure G.7: Time evolution of the asymmetry and electron populations for $T = 22$ K and $P = 0.5$ bar.

H

Tables of FWHM and Peak Values of Asymmetry in μH

The tables in this appendix were all obtained considering the laser on for τ= 100 ns. All of the tables include the FWHM and peak value (which always corresponds to the resonance Δ= 0 MHz) of the dark state. The tables were obtained for two pressures (1 bar and 0.5 bar), three temperatures (22 K, 30 K and 50 K), two laser bandwidths (10 MHz and 100 MHz) and three fluences (10 Jcm^{-2}, 20 Jcm^{-2} and 50 Jcm^{-2}). Each table correspond to a different polarization (η= 0, 0.25, 0.5, 0.75, 1, left polarizations produce the same result as the positive with the same absolute value).

Table H.1: FWHM and peak values of the asymmetry profile with polarization η= 0.25.

			$\mathcal{F}$ = 10Jcm^{-2}		$\mathcal{F}$ = 20Jcm^{-2}		$\mathcal{F}$ = 50Jcm^{-2}	
P [bar]	T [K]	Γ_l [MHz]	FWHM [MHz]	$\mathcal{A}^{\text{peak}}$ $\times 10^{-2}$	FWHM [MHz]	$\mathcal{A}^{\text{peak}}$ $\times 10^{-2}$	FWHM [MHz]	$\mathcal{A}^{\text{peak}}$ $\times 10^{-2}$
0.5	22	100	323	0.089	324	0.178	326	0.437
1	22	100	458	0.031	458	0.061	459	0.152
0.5	22	10	251	0.120	251	0.239	253	0.586
1	22	10	378	0.038	378	0.075	379	0.187
0.5	30	100	311	0.129	312	0.256	314	0.627
1	30	100	406	0.048	406	0.095	407	0.236
0.5	30	10	244	0.176	245	0.347	247	0.840
1	30	10	331	0.060	331	0.120	332	0.298
0.5	50	100	321	0.214	322	0.422	326	1.014
1	50	100	373	0.091	373	0.181	375	0.445
0.5	50	10	257	0.289	259	0.568	262	1.321
1	50	10	307	0.117	308	0.232	310	0.567

Table H.2: FWHM and peak values of the asymmetry profile with polarization η= 0.5.

			$\mathcal{F}$ = 10Jcm^{-2}		$\mathcal{F}$ = 20Jcm^{-2}		$\mathcal{F}$ = 50Jcm^{-2}	
P [bar]	T [K]	Γ_l [MHz]	FWHM [MHz]	$\mathcal{A}^{\text{peak}}$ $\times 10^{-2}$	FWHM [MHz]	$\mathcal{A}^{\text{peak}}$ $\times 10^{-2}$	FWHM [MHz]	$\mathcal{A}^{\text{peak}}$ $\times 10^{-2}$
0.5	22	100	323	0.152	324	0.302	326	0.743
1	22	100	458	0.052	458	0.104	459	0.259
0.5	22	10	251	0.205	251	0.407	253	0.996
1	22	10	378	0.064	378	0.128	379	0.318
0.5	30	100	311	0.219	312	0.435	314	1.065
1	30	100	406	0.081	406	0.162	407	0.401
0.5	30	10	244	0.298	245	0.590	247	1.428
1	30	10	331	0.103	331	0.205	332	0.506
0.5	50	100	321	0.364	322	0.718	326	1.724
1	50	100	373	0.155	373	0.308	375	0.756
0.5	50	10	257	0.492	259	0.965	262	2.247
1	50	10	307	0.199	308	0.394	310	0.963

Table H.3: FWHM and peak values of the asymmetry profile with right circular polarization η= 0.75.

			$\mathcal{F}$ = 10Jcm^{-2}		$\mathcal{F}$ = 20Jcm^{-2}		$\mathcal{F}$ = 50Jcm^{-2}	
P [bar]	T [K]	Γ_l [MHz]	FWHM [MHz]	$\mathcal{A}^{\text{peak}}$ $\times 10^{-2}$	FWHM [MHz]	$\mathcal{A}^{\text{peak}}$ $\times 10^{-2}$	FWHM [MHz]	$\mathcal{A}^{\text{peak}}$ $\times 10^{-2}$
0.5	22	100	323	0.182	324	0.362	326	0.892
1	22	100	458	0.063	458	0.125	459	0.310
0.5	22	10	251	0.246	251	0.488	253	1.196
1	22	10	378	0.077	378	0.154	379	0.382
0.5	30	100	311	0.263	312	0.523	314	1.278
1	30	100	406	0.097	406	0.194	407	0.482
0.5	30	10	244	0.358	245	0.708	247	1.713
1	30	10	331	0.123	331	0.246	332	0.608
0.5	50	100	321	0.437	322	0.861	326	2.069
1	50	100	373	0.186	373	0.369	375	0.908
0.5	50	10	257	0.590	259	1.158	262	2.695
1	50	10	307	0.238	308	0.473	310	1.156

Table H.4: FWHM and peak values of the asymmetry profile with right circular polarization $\eta = 1$.

			$\mathcal{F} = 10\text{Jcm}^{-2}$		$\mathcal{F} = 20\text{Jcm}^{-2}$		$\mathcal{F} = 50\text{Jcm}^{-2}$	
P [bar]	T [K]	Γ_l [MHz]	FWHM [MHz]	$\mathcal{A}^{\text{peak}}$ $\times 10^{-2}$	FWHM [MHz]	$\mathcal{A}^{\text{peak}}$ $\times 10^{-2}$	FWHM [MHz]	$\mathcal{A}^{\text{peak}}$ $\times 10^{-2}$
0.5	22	100	323	0.190	324	0.377	326	0.929
1	22	100	458	0.065	458	0.130	459	0.323
0.5	22	10	251	0.256	251	0.508	253	1.246
1	22	10	378	0.080	378	0.160	379	0.398
0.5	30	100	311	0.274	312	0.544	314	1.331
1	30	100	406	0.101	406	0.202	407	0.502
0.5	30	10	244	0.373	245	0.738	247	1.785
1	30	10	331	0.128	331	0.258	332	0.633
0.5	50	100	321	0.455	322	0.897	326	2.155
1	50	100	373	0.193	373	0.384	375	0.946
0.5	50	10	257	0.615	259	1.206	262	2.808
1	50	10	307	0.248	308	0.493	310	1.204

I

Figures of Time Evolution of Asymmetry in μ^3He^+

The time evolution of the $F=1$ states and electron populations without decays are shown in figures I.1, I.2, I.3 and I.4, for the polarizations $\eta=0$, 0.25, 0.75 and 1, respectively. For all figures, the total excited state $F=1$ population is represented with a black line. The $m_F=-1$ sub-level population and electron ρ_e^- population are represented with a red line and the $m_F=1$ sub-level and ρ_e^+ with a blue line. The excited $m_F=0$ population is represented with a magenta line while the ρ_e^0 electron population is represented with a purple line. The exponential decay of the muon total population and its complementary negative exponential decay of the electron populations is included with the black dashed lines. The solutions presented were all obtained for a fluence of $\mathcal{F}=10$ Jcm^{-2} during $\tau=1000$ ns.

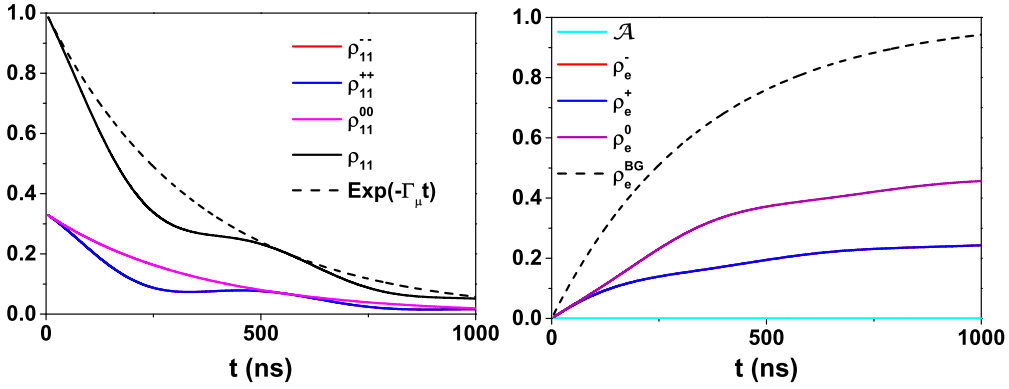

(a) Atomic populations.

(b) Electron populations.

Figure I.1: Time evolution of the $F=1$ atomic states (a) and electron populations (b) of μ^3He^+ for linear polarization, $\eta=0$. The ρ_{11}^{--} and ρ_{11}^{++} populations are equal, as well as the ρ_e^- and ρ_e^+

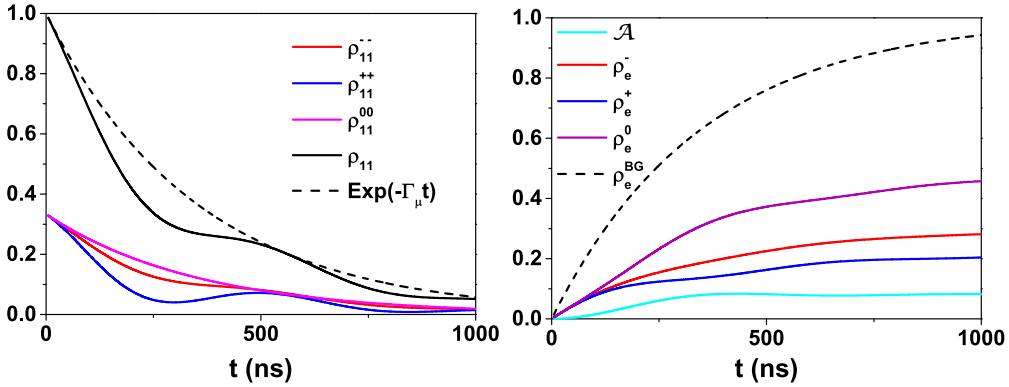

(a) Atomic populations. (b) Electron populations.

Figure I.2: Time evolution of the F= 1 atomic states (a) and electron populations (b) of μ^3He$^+$ for polarization η= 0.25.

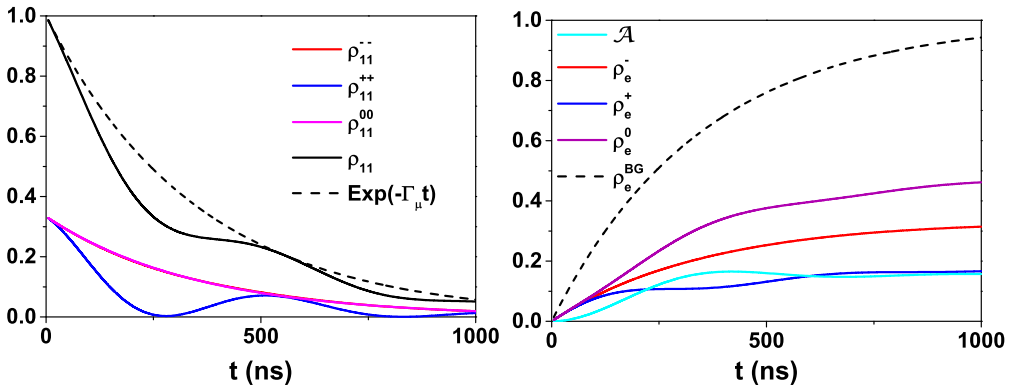

(a) Atomic populations. (b) Electron populations.

Figure I.3: Time evolution of the F= 1 atomic states (a) and electron populations (b) of μ^3He$^+$ for polarization η= 0.75.

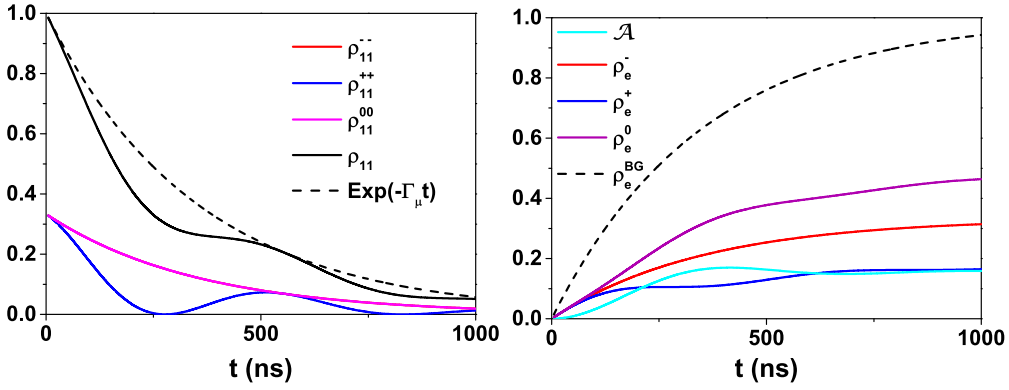

(a) Atomic populations. (b) Electron populations.

Figure I.4: Time evolution of the F= 1 atomic states (a) and electron populations (b) of μ^3He$^+$ for right circular polarization, η= 1.